UNIVERSITÀ DEGLI STUDI DI PADOVA

DIPARTIMENTO DI INGEGNERIA INDUSTRIALE

CORSO DI LAUREA MAGISTRALE IN INGEGNERIA CHIMICA
E DEI PROCESSI INDUSTRIALI

Tesi di Laurea Magistrale in

Ingegneria Chimica e dei Processi Industriali

Temperature programmed reductions and oxidations on cupric oxide: parametric sensitivity and investigations on thermal effects

Relatore: Prof. Paolo Canu

Correlatrice: Ing. Benedetta Oliani

Laureanda: SARA CAPITANIO

ANNO ACCADEMICO 2019 – 2020

Abstract

In this thesis work, Temperature-Programmed Reduction (TPR) and Temperature-Programmed Oxidation (TPO) techniques have been used to determine the cyclic redox reactivity of cupric oxide, based on the peak shape analysis and the total oxygen removed during reductions and regained during oxidations. In parallel, the impact of thermal effects, considered as potential inhibitors of the solid reactivity, has been evaluated.

The variation of experimental parameters allowed to determine the reactivity of cupric oxide under different experimental conditions and to gain additional information on its reaction mechanism, mass transfer limitations and thermal inertia of the solid.

The peak shape analysis, coupled with the quantification of oxygen removed from cupric oxide during the TPR, and regained by copper during TPO, proved to be effective in identifying a loss in catalytic activity during sequential reduction and oxidation cycles. A physical agglomeration of the bed has been observed and therefore further studied by increasing the solid mass analysed. The monitoring of pressure drops along the bed during the reactions and the images provided by the Scanning Electron Microscope confirmed the agglomeration phenomenon.

A bed dilution with silicon carbide has positively affected both reduction and oxidation process, as it reduced temperature gradients in the solid bed and delayed the agglomeration effect.

Contents

Introduction

Temperature-Programmed Reduction (TPR) is a characterization technique widely used in surface science to determine the reduction properties of bulk and/or supported metal oxides as temperature is linearly increased in a reducing flow. Similarly, Temperature-Programmed Oxidations (TPO) measure the reactivity of a reduced material towards oxidation by flowing an oxidant mixture. The metal oxide reactivity is then inferred with the peak shape analysis and the quantification of gaseous reagent consumed allows to indirectly evaluate the reduction or oxidation degree of the reacting solid phase. When coupled and performed cyclically, these two techniques can be used to evaluate the properties and the long-term reactivity of redox materials. These assessments are essential for the selection of a suitable metal oxide to carry out cyclic redox processes, such as chemical looping combustions. In these peculiar systems, the metal oxide acts as an oxygen carrier, thus limiting or avoiding the use of gaseous O_2. The advantages in terms of cost and safety are evident, but unaltered performances over time are indeed desired.

TPR and TPO analyses are usually carried out using a standardized experimental protocol and conditions (solid mass, flowrate, reducing/oxidizing concentration, heating rate) to guarantee a fair comparison between results. However, the major drawback is the lack of information regarding potential mass transfer limitations, surface and bulk species reactivity, thermal inertia, structural changes/aging that may mislead the analyses.

As first assessment of this thesis work, the behaviour of CuO/Cu system was studied by varying the experimental conditions and demonstrating that the aforementioned information can be retrieved.

The second objective was the assessment of the cyclic redox efficiency of cupric oxide (CuO) to be used as oxygen donor in chemical looping processes. In parallel, insights about the efficiency loss were carried out by studying the thermal effects of both reduction and oxidation. As literature reports, even placing in optimal conditions and using a model reactive specie as CuO, anomalous reactivity, resulting in multiple peaks in reduction profiles, has been detected. This behaviour has been attributed to three reasons: diffusional limitations induced by the reaction products covering the unreacted particles, the release of trapped gaseous reagent, the presence of a multiple-step mechanism.

The third objective was the correlation of these anomalies in CuO reactivity to an uneven temperature distribution in the sample. Following this hypothesis, the effect of bed dilution with

silicon carbide (SiC), known for its excellent thermal properties, on the reduction profiles and bed agglomeration was also studied.

This thesis is structured in four chapters. In Chapter 1, a bibliographic research is reported to provide a general view on TPR/TPO techniques, with particular attention to the optimal choice of experimental parameters, multiple-peaks and thermal phenomena. The experimental set-up, the experimental procedure to carry out TPR and TPO analyses and the method to quantify the oxygen consumed and regained by the oxide are presented in Chapter 2. The results of the parametric sensitivity on TPR/TPO techniques are then shown in Chapter 3. In Chapter 4, the outcome of CuO/Cu system cyclic redox reactivity and characterizations with SEM of spent CuO are shown.

This experimental work was carried out at the premises of K-INN Lab research group, based at the Department of Industrial Engineering (Via Marzolo, 9) at University of Padova.

SEM and EDS analyses were performed at Centro di Analisi e Servizi per la certificazione CEASC (Via Jappelli 1/A).

Chapter 1

State-of-the-art

The main objective of this thesis work is providing a more thorough insight into the temperature-programmed reaction analyses and their possible utilization for intuition on the reaction mechanism of a catalyst. The influence of experimental parameters variation on TPR/TPO test is then explored using Cu/CuO as a reference. Finally, the results obtained are interpreted taking into consideration the thermal effect that naturally develops as the reaction progresses.
In this chapter the literature concerning the interpretation and optimal conditions for temperature programmed reductions is reviewed.

1.1 Temperature programmed reductions

Temperature-Programmed reactions are simply chemical transformations carried out under a given temperature policy. Depending on the reagent, they can be either reduction or oxidations. Temperature-Programmed Reduction (TPR) is a characterization technique commonly used to assess the redox proprieties of metal oxides, mixed metal oxides and metal oxides dispersed on a support. Namely, it provides qualitative and quantitative information of the type and reducibility (i.e. oxidation state) of metals on the surface and in the bulk, as well as changes in reactivity resulting from promoters or metal/support interactions [1]. In a typical TPR experiment, the sample is placed in a fixed bed reactor through which a reducing mixture (usually H_2 in Ar) flows across and the temperature is linearly increased. A highly sensitive detector, such as a Thermal Conductivity Detector, continuously analyses the outlet stream and the reducing gas concentration can be plotted against temperature. The integration of the concentration curves yields the total amount of reducing gas consumed, directly correlated to the total reducible species in the sample, and the peak position (i.e. temperature) gives information on the sample reducibility (e.g. reaction rate and steps).
The basic rationale for Temperature-Programmed Oxidation (TPO) is the same as for TPR, but in the TPO the sample is in a reduced form and an oxidizing mixture (air or O_2) is flowed over the sample. This analysis is also performed to quantify the amount of carbonaceous deposits deriving from coking or any other reaction involving organic compounds [2], however the same results obtainable with TPR are achievable for oxidations. Additionally, coupled TPR/TPO

experiments provide useful information on the redox behaviour of a catalyst and its long-term reactivity when subject to cyclic reducing/oxidizing atmospheres.
For the sake of simplicity, only TPR will be analysed as it is a wider applied technique than TPO.

1.2 Reduction reactions

1.2.1 Thermodynamics

The complete reduction of a metal oxide can be written as in Equation (1.1)

$$M_xO_y + yH_2 \rightarrow xM + yH_2O \tag{1.1}$$

and pure metal M with an oxidation state of 0 is produced together with H_2O. The Gibbs free energy of reaction (ΔG_R) can be computed as a function of temperature (T) and activities of the gaseous species (a_i). Assuming ideal gas mixtures, the activities of the gas species are the partial pressure (P_i) divided by a reference pressure, while the activity of solids is unitary, so the resulting equation is Equation (1.2):

$$\Delta G_R = \Delta G_R^0 + RT\ log\frac{a_{H2O}}{a_{H2}} \approx \Delta G_R^0 + RT\ log\frac{P_{H2O}}{P_{H2}} \tag{1.2}$$

From a thermodynamic point of view, this reaction is spontaneous only when $\Delta G_R < 0$. This condition is satisfied when ΔG_R^0 is negative, as it happens for most of the metallic oxides, but also when ΔG_R^0 is positive (e.g. for vanadium or chromium oxides [3]) provided that the second term is sufficiently negative. Practically speaking, the reaction is favoured by decreasing H_2O partial pressure in the system, i.e. removing the product as soon as it is formed [3].

1.2.2 Kinetics and mechanism of bulk oxides

The kinetics for a reduction reaction is usually expressed as degree of reduction (α), which is a function of time (t) and is defined as in Equation (1.3)

$$\alpha = \frac{V_M(t)}{V_{M,fin}} \tag{1.3}$$

where $V_M(t)$ is the volume of the metal M formed at a certain time t and $V_{M,fin}$ is the volume of the metal M at the end of the process. Alternatively, if the metal percentage and the reaction stoichiometry are known, the degree of sample reduction is given by the ratio (Equation (1.4))

$$\alpha = \frac{n_{H2}}{n_M s_f} \tag{1.4}$$

where n_{H2} is the number of detected hydrogen atoms that are proportional to the peak area, n_M is the total number of metal atoms contained in the sample and s_f is the stoichiometric factor depending by the initial oxidation state and by the final product.
The reduction of a metal oxide is usually described with two models: the nucleation one and the contracting sphere one [3]. They are based on few assumptions:

1. the metal oxide is in its bulk form (thus no effect due to support, impurities or anisotropies are present);
2. the metal oxide is made of spherical particles;
3. the reaction rate depends on the surface area.

These two models are somewhat simplified since they do not consider thoroughly the oxide ion diffusion, or the production of water that modifies the composition of the fluid phase, or also the porosity of the bed. Those parameters may be introduced to properly fit experimental data.

1.2.2.1 Nucleation Model

According to this model, which considers a particle of a bulk oxide as represented in Figure 1.1.a, the reducing gas reacts with surface oxygen from the metal oxide creating an anion vacancy in the lattice. A structural rearrangement happens when the vacancy concentration exceeds its critical value and this yields to the formation of small grains of lower oxide or metal. The surface available for reaction begins then to increase, and so does the reaction rate, as shown in Figure 1.1.b and Figure 1.1.c by means of α and its derivative over time. These grains grow until their boundaries overlap, creating a core-shell structure in which the inner part is still oxidised and covered by a reduced oxide/metal layer. From this moment onwards the reaction rate decreases, and the reduction follows the contracting spheres model.
This model successfully describes the reduction of NiO [3].

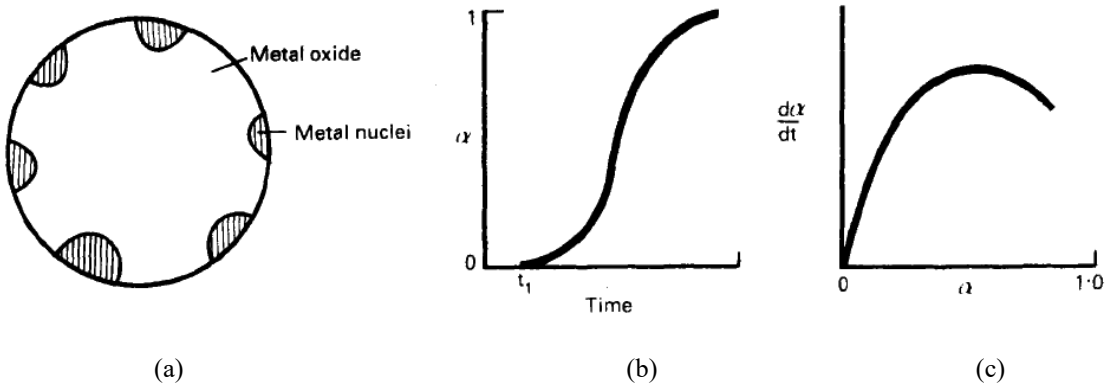

Figure 1.1: *Nucleation model:* (a) *particle representation,* (b) *degree of reduction over time and* (c) *reduction rate over time.*

1.2.2.2 Contracting sphere model

This model is an extreme case of the nucleation model and it can be used when the nucleation process is fast, such as in the reduction of MnO_2 to Mn metal [3]. In this case a large number of small reduced oxide grains are formed on the oxide surface, whose boundaries overlap creating a thin layer of metal over the oxide surface, as represented in Figure 1.2.a. Since the reaction surface decreases (i.e. the interface between metal and metal oxide) and the height of the reduced metal shell through which the reagents should diffuse increases, the rate of reduction ($d\alpha/dt$) slows down as the process evolves. This is shown in the plot of Figure 1.2.c. The profile of the degree of reduction α will consequently have the shape reported in Figure 1.2.b [3].

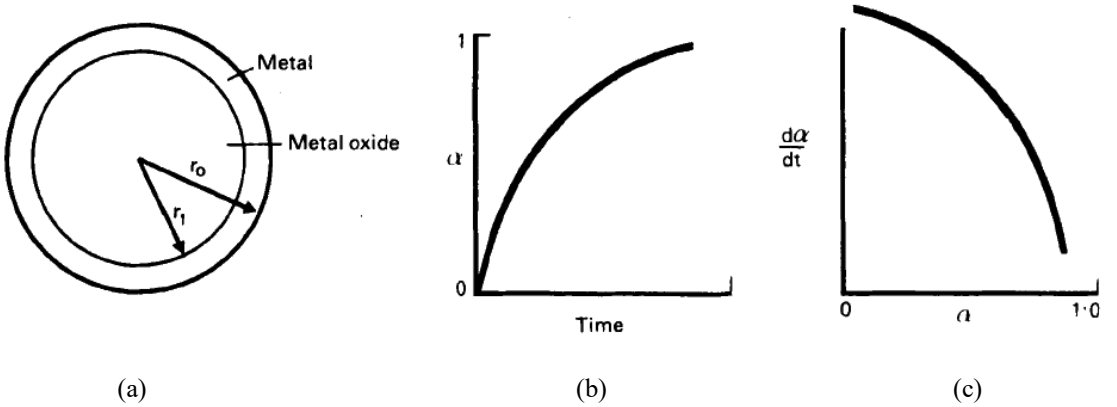

Figure 1.2: *Contracting sphere model:* (a) *particle representation,* (b) *degree of reduction over time and* (c) *reduction rate over time.*

1.2.2.3 Theory of non-isothermal reductions

When a generic gas-solid reaction

$$Gas + Solid \rightarrow Product$$

is considered, the reaction rate can be expressed as

$$R = -\frac{d[G]}{dt} = -\frac{d[S]}{dt} = K[G]^p[S]^q \tag{1.5}$$

where $[G]$ is the concentration of the gaseous reagent, $[S]$ is the concentration of the solid reagent, p and q are the partial orders of reactions for the gaseous and solid reagent respectively, and K is the kinetic constant of the process. K of Equation (1.5) can be expressed with the Arrhenius equation as in Equation (1.6):

$$K = Ae^{-\frac{E_a}{R_g T}} \tag{1.6}$$

where A is its pre-exponential factor, E_a is the activation energy, R_g is the gas constant and T is temperature.

Since temperature is raised in TPR experiments it is a function of time. For a constant heating, the heating rate β is defined as in Equation (1.6)

$$\beta = \frac{dT}{dt} \tag{1.7}$$

Through a change of variables, Equation (1.5) can be rewritten as

$$R = -\beta\frac{d[G]}{dT} = -\beta\frac{d[S]}{dT} = K[G]^p[S]^q \tag{1.8}$$

making explicit its dependence upon β and T.

Following a thermogravimetric approach, E_a can be retrieved analytically by rewriting Equation (1.7) in terms of reduced solid fraction γ:

$$\gamma = \frac{S}{S_0} \tag{1.9}$$

being S the amount of reducible solid at a certain time t and S_0 the initial amount of reducible solid, and the concentration of reducing gas is assumed constant (e.g. in excess reducing gas), the term $[G]^p$ can be embedded into the kinetic constant K, so that $K' = K[G]^p$, and Equation (1.8) takes the form

$$R = \frac{d\gamma}{dt} = K'(1-\gamma)^q \tag{1.10}$$

Combining Equations (1.6), (1.7) and (1.10), integrating and taking logarithms gives

$$\log\left[1 - \frac{(1-\gamma)^{1-q}}{1-q}\right] = log\frac{AR}{\beta E_a}\left[1 - \frac{2R_gT}{E_a}\right] - \frac{E_a}{2.3R_gT} \tag{1.11}$$

if $q \neq 1$ (i.e. when the reaction is not first order with respect to the solid) while it gives

$$\log\left[-log\frac{(1-\gamma)}{T^2}\right] = log\frac{AR}{\beta E_a}\left[1 - \frac{2R_gT}{E_a}\right] - \frac{E_a}{2.3R_gT} \tag{1.12}$$

if $q = 1$ (i.e. when the reaction is first order with respect to the solid).
For most values of E_a over temperature the value of $\log(AR_g/\beta E_a)[1 - 2R_gT/E_a]$ is essentially constant, so a straight line with slope equal to $-E_a/(2.3R_g)$ will be found by plotting the left-hand side of Equation (1.11) or (1.12) against $1/T$, provided that the parameter q is correct.
However the derivation of kinetic parameters with Equation (1.11) or (1.12) is not practical, since most of the experimental TPR systems monitor the difference in reducing gas concentration between the reactor inlet and the outlet. To overcome this issue, Gentry *et al.* [4] suggested to focus on the consumption rate of gas instead of using the fraction of reduced solid γ. By working with the rate of reaction expressed as in Equation (1.8) together with the simplifying assumptions of:

1. the reactor behaving like a plug-flow;
2. low conversions of reducing gas;
3. $p = q = 1$ (i.e. the reaction is elementary);

the authors derived an analytical equation through which a value of E_a is obtained by means of experimental data at peak conditions. The equation is derived by considering that at the maximum rate of reaction, the derivative of both the rate of reaction and the concentration of reacting gas are null, resulting in the equation

$$2\ln T_{max} - ln\beta + \ln[G]_{max} = \frac{E_a}{R_gT_{max}} + constant \tag{1.13}$$

where T_{max} indicates the temperature at peak conditions and $[G]_{max}$ the concentration of reducing gas at peak conditions. A straight line of slope E_a/R_g is then obtained by plotting the left side of Equation (1.13) against $1/T_{max}$.

Similarly, Monti and Baiker [5] found an analytical expression to correlate the H_2 consumption rate with temperature by modelling the reacting system as a perfectly mixed reactor. The Authors solved the mass balance for H_2 using the mean H_2 concentration $\bar{c}$ between the inlet and the outlet, combined it with Equation (1.8) to express the rate of reaction as function of temperature and assumed the reaction elementary with respect to both the gas and the solid (i.e. $m = q = 1$). The resulting relation between the experimental parameters and the kinetic parameters is

$$\frac{dS}{dT} = -\frac{2c_0V^*}{\beta}\left(\frac{1}{1+\frac{2V^*}{SAe^{\frac{-E_a}{RT}}}}\right) \tag{1.14}$$

where S is the current amount of reducible species, V^* is the total flowrate of the reducing gas, c_0 is the inlet concentration of hydrogen, and the other terms as described above. The equation used to estimate kinetic parameters A and E_a through linear regression is then found by considering that at the H_2 consumption peak there is a maximum in the rate of reduction and logarithms are applied to both sides, giving

$$ln\frac{T_{max}^2\bar{c}_{max}}{\beta} = \frac{E_a}{R_gT_{max}} + ln\frac{E_a}{R_gA} \tag{1.15}$$

where subscript max refers to the operating conditions at the peak.
While this method to estimate kinetic parameters is simple and it is well suited to be fitted by a computer program, it is valid under the assumptions of:

1. negligible interparticle mass transfer limitations;
2. diffusion coefficients calculated on the assumption of binary mixture composed of H_2 and N_2 only;
3. negligible intraparticle diffusion limitations.

Hypothesis 1) involves the calculation of a mass transfer coefficient based on Sherwood non-dimensional number of the particles in the bed. This number can be expressed by accounting directly for the porosity of the bed, as Gunn [6] derived in his work

$$Sh = \frac{2k_fR_P}{D} = (7-10\varepsilon+5\varepsilon^2)\left(1+0.7Re_p^{0.2}Sc^{1/3}\right)+\cdots \\ \ldots+(1.33-2.4\varepsilon+1.2\varepsilon^2)Re_p^{0.7}Sc^{1/3} \tag{1.16}$$

where Sh is the Sherwood number, k_f is the fluid-solid mass transfer coefficient, R_P is the particle radius, D is the diffusion coefficient, ε is the porosity of the bed, Re_p is the Reynolds number of the particle and Sc is the Schmidt group. If Equation (1.16) provides a value for Sh

so that the concentration gradient of the reducing gas between the particle surface and the bulk gas phase is negligible with respect to c_0, hypothesis 1) is correct. On the other hand, Equation (1.15) could not be appropriate if the bed agglomerates in the process, since its porosity would not be constant anymore, and so a more suitable correlation should be found. Moreover, in this case also the bed surface area could not be supposed constant, thus leading to a complication of the reagent rate of consumption.

Hypothesis 2), instead, can be too simple, since diffusion coefficients of a component in a mixture are strongly dependent upon the molar fraction of all the components present in the mixture. This is pointed out by the Maxwell-Stefan equation [7]

$$\nabla x_i = -\sum_{j=1}^{NC} \frac{1}{cD_{i,j}} \left(x_i N_j - x_j N_i\right) , \qquad i = 1 \dots NC \tag{1.17}$$

where x_i is the molar fraction of component i in the mixture, N_i the molar amount of component i in the mixture, c is the total mixture concentration and $D_{i,j}$ the binary diffusion coefficient of component i into component j. Considering that the reduction of an oxide produces water, a more precise calculation of the diffusion coefficient D would account for its molar fraction dynamically, changing its value as the reaction progresses. Moreover, the calculation of the single $D_{i,j}$'s should account also for temperature, as the binary diffusion coefficients for gases are dependent upon $T^{1.4}$. However, diluted H_2 mixture are usually adopted, so that the Stefan-Maxwell correction is expected to be small.

Hypothesis 3) is based, instead, on the correlation proposed by Ibok and Ollis [8], for which a dimensionless number Φ is calculated as

$$\Phi = \frac{R_p^2}{D_{eff}} \left(\frac{1}{V_c} \left(\frac{dn}{dt}\right)_{max}\right) \frac{1}{c_s} \tag{1.18}$$

with D_{eff} being the diffusion coefficient accounting for both particle surface porosity and tortuosity of its pores, V_c being the sample volume, $(dn/dt)_{max}$ the consumption rate of hydrogen at the peak, and c_s the sample volume. If Φ is smaller than 0.3, intraparticle diffusion can be neglected. Under the experimental conditions used by Monti and Baiker [5], the assumption was satisfied if using particles with radii < 0.04 cm and tortuosity factor < 3, but the validity of this assumption should be checked experimentally or using Equation (1.18).

Differently from Gentry *et al.* and Monti and Baiker, who focused on the gaseous reagent consumption, Malet and Caballero [9] developed a model that expresses the rate of reduction of a solid species with hydrogen using the degree of reduction γ as stated in Equation (1.9). Supposing a one-step reduction process which follows a first-order kinetic both with respect to hydrogen and solid concentration, the resulting relation is

$$\frac{d\gamma}{dT} = \frac{A\, e^{\frac{-E_a}{RT}}(1-\gamma)}{\frac{\beta}{c_0} + PA\, e^{\frac{-E_a}{RT}}(1-\gamma)} \tag{1.19}$$

where P is the Malet parameter and the other parameters remain as defined above. In this case the Malet parameter P $[K]$ is defined as

$$P = \frac{\beta S_0}{F c_0} \tag{1.20}$$

where F is the volumetric flowrate of carrier, c_0 the hydrogen concentration at the reactor inlet, S_0 the initial amount of reducible species and β is the heating rate. This model was used successfully by the authors to obtain theoretical TPR curves, and the definition of P as in Equation (1.20) allowed them to study separately the influence of its parameters on the peak shape and maxima.

1.3 Variation of experimental parameters and conditions

Since it was experimentally ascertained that TPR results are very sensitive to the experimental conditions used (e.g. mixture volumetric flowrate $V*$, initial oxide mass S_0, heating rate β, and inlet reductant concentration at standard conditions c_0), Gentry *et al.* [4], Monti and Baiker [5] and Malet and Caballero [9] investigated their influence on the temperature of maximum reduction rate (peak temperature, T_{max}) as it was demonstrated to be essential in Equation (1.13) and Equation (1.15). Additionally, Gentry *et al.* [4] and Malet and Caballero [9] analysed the peak shapes, relating their deformations to the change in the operating parameters. The sensitivity analysis that Monti and Baiker [5] carried out is shown in Figure 1.3, which provides a comparison between experimental results and values predicted by the numerical integration of the mass balances into the reactor model of Equation (1.14).

From the results obtained, T_{max} almost linearly increases with the heating rate, while by increasing c_0, T_{max} exponentially decreases. This trend is confirmed by Gentry *et al.* [4] in their copper zeolite (Cu, Na)-X-50: T_{max} decreases by approximately 10 K for each 1% increase in inlet hydrogen concentration. For these two parameters, the model fit experimental data in an acceptable way.

On the other hand, the model predictions deviate from experimental values of T_{max} for low values of $V*$ (between 0.7 and 1.7 cm^3(NTP)/s) which are instead in accordance with the ones of Gentry, who reported that an increase from 0.167 to 0.333 cm^3(NTP)/s with 4% H_2 lowered T_{max} by 15-30 K. The total mass of solid (i.e. the quantity of reducible species), has a weak but not negligible effect on T_{max}, as an S_0 increase from 199 to 500 μmol lead to an increase of the experimental T_{max} by 12 K.

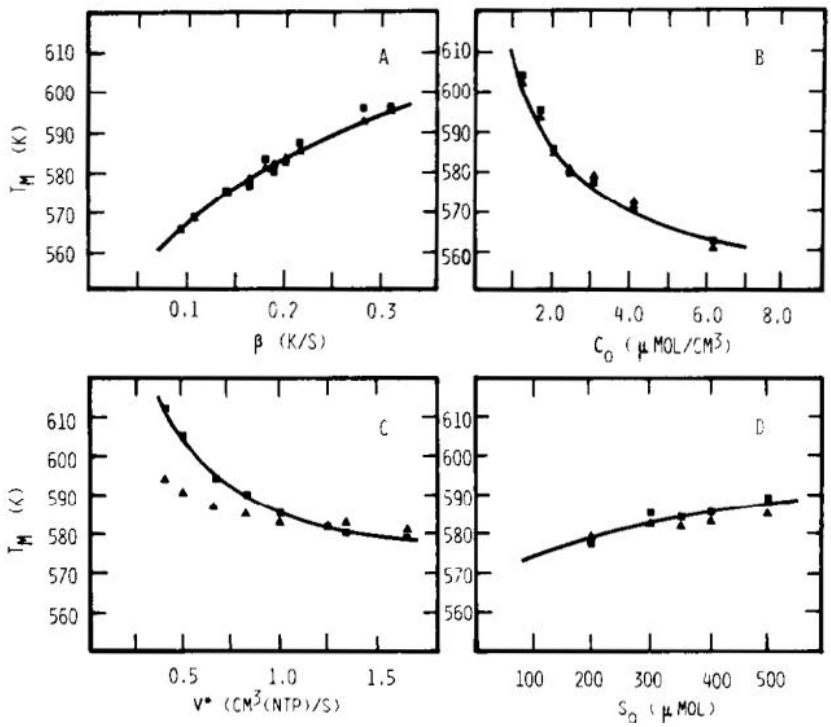

***Figure 1.3**: Parametric sensitivity of the temperature of the maximum reduction rate. Standard conditions: c_0=2.46μmol/cm^3, S_0=405 μmol NiO, V*=1.25 cm^3 (NTP)/s, β=0.2 K/s. (■) Experimental values, (▲) calculated values. [5]*

To facilitate the selection of appropriate operating variables, a number, called the Baiker parameter K [s] is defined as

$$K = \frac{S_0}{V^* c_0} \tag{1.21}$$

where S_0 is the initial quantity of reducible species, $V*$ is the mixture volumetric flowrate and c_0 is the inlet reductant concentration at standard conditions.

The Baiker parameter itself is developed to make reasonable the assumption of using the mean hydrogen concentration $\bar{c}$ into the reactor. Practically speaking, it requires to operate with low fractional conversions of hydrogen, but high enough to be measured by the detector. As a general rule, it is then prescribed to operate in such a way that the amount of hydrogen consumed at the peak never exceeds 2/3 of the hydrogen fed and that the minimum conversion at the peak should be 10%. Within these conditions, a value of K from 55 to 140 s is suggested when heating rates between 0.1 and 0.3 K/s are applied.

Regarding the peak shape, Gentry *et al.* [4] observed that the mass of solid and pre-treatments influence the H_2 consumption and the resolution and number of peaks. Decreasing the mass of solid (from 400 mg to 50 mg) the resolution of the peak increases and two separate reduction steps can be observed, i.e. the presence of two peaks. This fact was attributed by the authors to the temperature gradients that can originate into the sample, and to the hydrogen concentration

gradients. Additionally, they observed that the use of air or an inert gas to pre-treat the sample influences both T_{max} and the H_2 consumption: specifically, air increases the consumption of H_2 in (Cu, Na)-Y-68 zeolite with respect to N_2 without altering the temperature of the peaks. This could be connected to some morphological transformation of the solid.

The influence of the experimental parameters on the peak shape was computationally proven also by Malet and Caballero [9] who simulated TPR curves integrating the model of Equation (1.19) and studying the influence of both the ratio β/c_0 and P separately.

The model predicts that an increase in the ratio β/c_0 shifts the peaks towards higher temperatures, as Fig. Figure 1.4.a shows. Moreover, if the influence of the ratio $S_0/V*$ on the shape of the peaks is explored, it is seen that peaks flattens at their maxima as the number P increases, as shown in Figure 1.4.b. These two results are consistent with the experimental evidence of Monti and Baiker [5].

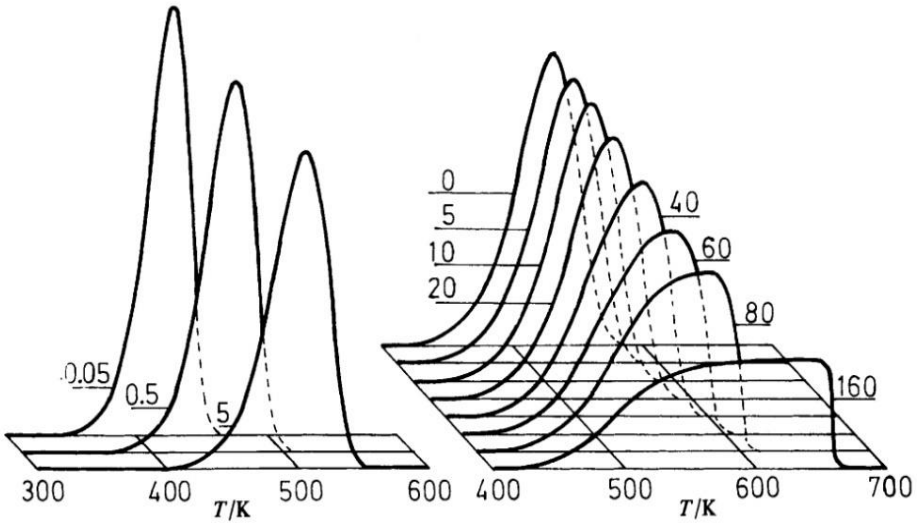

(a) (b)

Figure 1.4: *Simulated TPR curves for a single reduction process. E=24 kcal/mol, A=6·10⁹ min⁻¹;* (a) *P=5 K: effect of the ratio β/c₀;* (b) *β/c₀=20, effect of P. [9]*

The authors simulated TPR curves also for a two-step reduction process, and found that if P is kept constant and β/c_0 is increased, both a shift of the peaks and a loss of resolution occur, as Figure 1.5.a shows. If β/c_0 is instead kept constant and P is increased, a progressive loss in resolution accompanied by a flattening of the resulting peak is observed, as it can be seen in Figure 1.5.b.

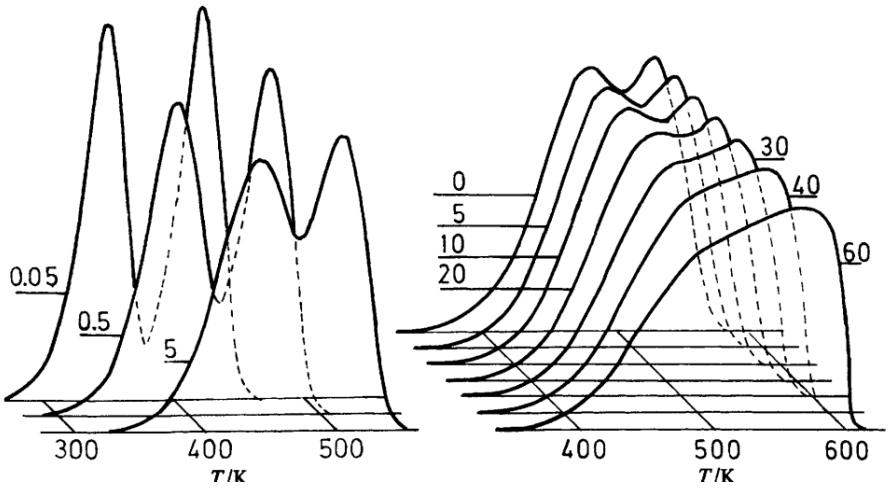

(a) (b)

Figure 1.5: *Simulated TPR curves for a two-step reduction process. E_1=15 kcal/mol, E_2=24 kcal/mol, $A_1=6\cdot10^6$ min^{-1}, $A_2=6\cdot10^9$ min^{-1}* (a) *P=5 K: effect of the ratio β/c_0;* (b) *β/c_0=20, effect of P. [9]*

These results are reproduced experimentally by the authors, who analysed different amounts of pure CuO while keeping constant the other parameters present in *P*. As shown in Figure 1.6, peaks merge together losing their resolution with greater amounts of sample analysed. These results explain also the ones obtained by Gentry *et al.* [4], who observed a similar loss in resolution with increasing amount of zeolite (Cu, Na)-X-50 analysed through their TPR studies.

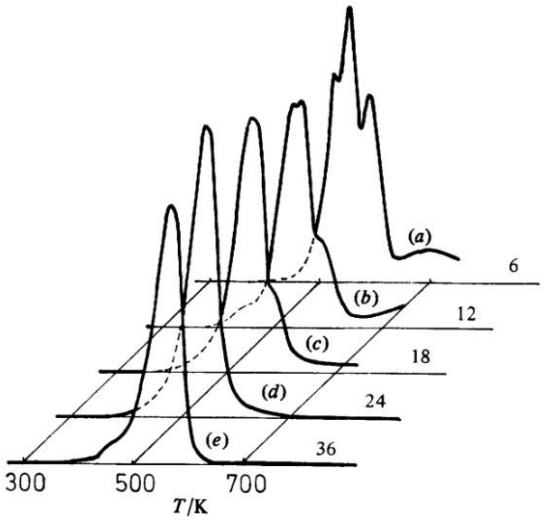

Figure 1.6: *TPR profiles for pure CuO (F=50 cm^3/min, β=0.167 K/s, C_0=2.232 μmol/cm^3). S_0/μmol= (a) 63, (b) 126, (c) 189, (d) 252 and (e) 378. Values of P/K are shown. [9]*

In order to clarify if those effects could be induced by heat-transfer phenomena, TPR profiles of 63 μmol of CuO sample were compared with the ones obtained by diluting the same amount of catalyst with 15 mg of Pyrex glass, sieved at d=100-200 μm. Since the two curves obtained

showed the same three peaks, it is concluded that no heat transfer effects is responsible of the merging of the peaks, but only the influence of incorrect ratio between the parameters used, whose effects are summarized in the parameter P. According to these authors, then, to avoid high distortions in the TPR profiles and maintain a good resolution, the parameter P should be kept as low as possible, and in any case lower than 20 K.

1.4 Anomalous peaks investigations

Considering Malet and Caballero results and applying Monti and Baiker approach, Fierro *et al.* [10] investigated TPR data of copper oxides (CuO and Cu_2O) catalysts under both adequate and inadequate conditions.

As Figure 1.7.a shows, a difference in the particle size of the CuO sample (D_p smaller than 100 μm and between 450 and 800 μm) at $K = 148\ s$ leads to a shift in the peaks towards higher values and to the appearance of a shoulder when the particle diameters are higher. Moreover, a drastic decrease in surface area of the samples leads to broader peaks and a slight shift of the maximum temperature towards higher values, as Figure 1.7.b reports. In both cases, no double peak appears, so none of these sample parameters could be the cause of multiple peaks observed in TPR's.

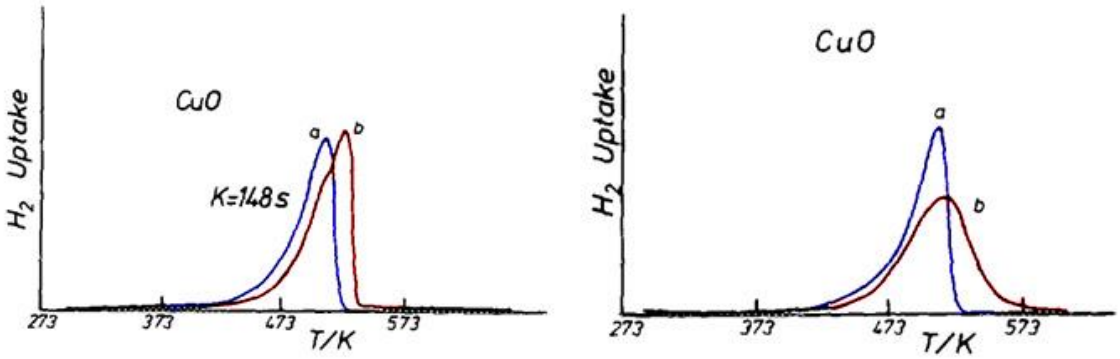

(a) (b)

Figure 1.7: *TPR profiles of two CuO batches having* (a) *different particle sizes: less than 100 μm (blue curve), and between 425 and 800 μm (red curve);* (b) *different surface area: 40 m2/g (blue curve), 2.4 m2/g (red curve). [10]*

As can be seen in Figure 1.8.A and Figure 1.8.B, instead, working intentionally with values of K greater than the ones proposed by Monti and Baiker gives rise to double peaks both in CuO and in Cu_2O samples. Differently, when experimental parameters are combined to have a value of K of 118 s for Cu_2O and of 148 s for CuO, one sharp peak is produced in both cases. Anomalous results are generated, instead, while testing CuO with $K = 65\ s$: even if K was within the suggested constraints, indeed, two broad peaks arises. The authors report that, in this case, a layer of copper deposited on the reactor wall. The test was then repeated using a different

reducing mixture and different sample amounts to have $K = 65\ s$ in one case, and $K = 38\ s$ in the other. What resulted is that a single and quite sharp peak was observed in both cases, as Figure 1.8.C shows.

Different profiles were also obtained by varying the heating rate parameter β while keeping high values of the parameter K, so studying the influence of the parameter P expressed in Equation (1.20). As Figure 1.8.D shows, for low enough values of P such as 7.3 K, a single peak is obtained.

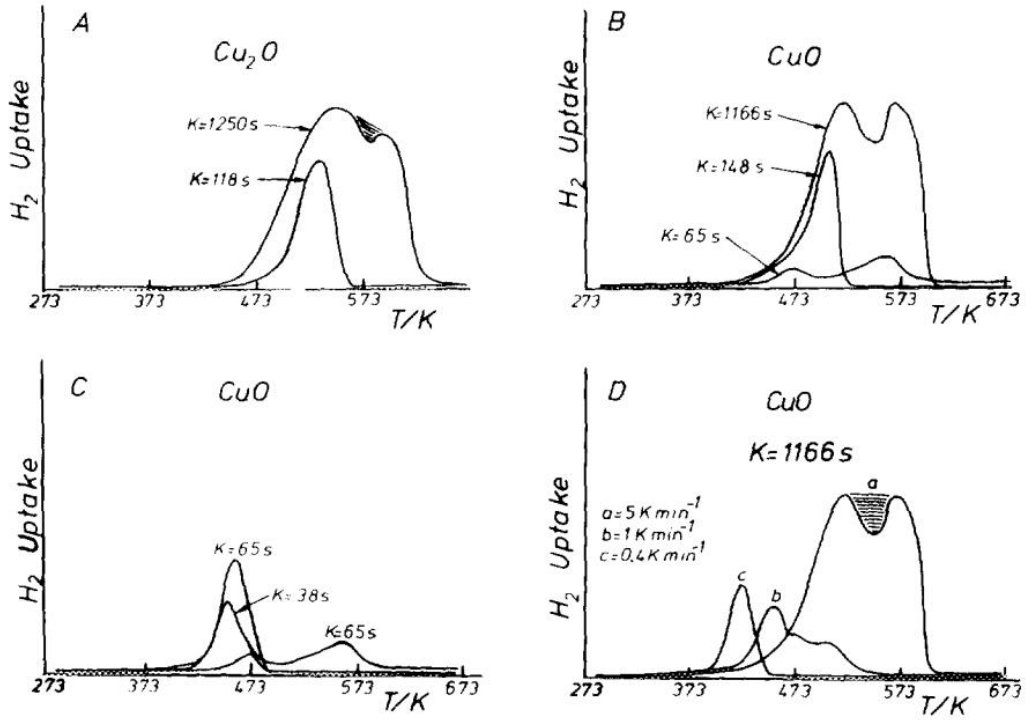

Figure 1.8: *TPR profiles of* (A) *Cu_2O under correct and wrong Baiker parameter;* (B) *CuO under correct and wrong Baiker parameter;* (C) *CuO under β=5 K/min, 10% H_2 in V*=90 ml (STP)/min of total flowrate; sample loadings: for K=65 s and P=5.4 K: 0.03490 g, for K=38 s and P=3.17 K: 0.02030 g; for the sake of comparison, also the reduction profile of CuO under K=65 s from frame (B) is reported;* (D) *CuO at fixed K value (ca. 1100 s) and different heating rates. Conditions for (b) and (c): 3% v/v H_2 in N_2, V*=40 ml (STP)/min, sample loadings: 0.07600 g, P(b)=18.3, P(c)=7.3. [10]*

These inconsistent results prove that the criterion of Monti and Baiker to choose the correct combination of experimental parameters through the K parameter is incomplete. The assumptions on which it is based must be revised and the dependence upon the heating rate β should be clarified.

1.5 Hypotheses on the double-peak origins

As seen in §1.4, a double-peak profile could arise when an incorrect combination of the experimental parameters is chosen. The reasons behind this behaviour are supposed to be both

the reactive environment at microscopic level and chemical nature of the sample. The following considerations are applied to the case of CuO since its reduction is easy to model and the experimental evidence regarding its behaviour in reduction is broader.

1.5.1 Sublimation of copper species

According to Fierro *et al.* [10], using low but adequate values of K on bulk CuO, double peaks could arise even when the particles are dispersed onto a membrane. This can happen when, upon temperature increase, the small particles of metallic copper can have enough energy to sublimate, thus covering the reactor walls and unreacted CuO particles. The reduction of the covered particles becomes more difficult since hydrogen needs to diffuse through it before reacting. Therefore, a second reduction peak appears at higher temperatures, producing a double-peak shape.

1.5.2 Hydrogen occlusion inside the copper lattice

It is known that metals with face-cubic crystal structures, such as Cu, may have structural defects like dislocations and micro-voids which can act as trap sites for hydrogen, as Lee and Lee [11] reports. It may happen that during a TPR test the small molecules of hydrogen are retained into the copper crystal lattice. If these phenomena happen while ramping up the temperature in a TPR run, the outlet hydrogen concentration will decrease because of a physical process, and not because of the reduction itself. At temperatures high enough to overcome the trap activation energy, on the other hand, hydrogen can desorb, giving rise to a double peak like the ones shown in Figure 1.8.

1.5.3 Presence of stable intermediates

Through time-resolved XRD studies of CuO powders, Rodriguez *et al.* [12] experimentally observed that the isothermal reduction of CuO at 240°C and at 200°C did not produce any stable intermediate, such as Cu_2O. The only difference was found in the induction times of the reactions, which were lower at higher temperatures. On the other hand, Cu_2O was found as a stable product when lower volumetric flowrates of reductant mixture together with low concentration of H_2 were fed to the reactive environment. A similar result can be obtained by mixing hydrogen with oxidants, as it was found by Günter *et al.* [13] using CuO/ZnO catalyst during methanol steam reforming.

To explain the phenomenon, Rodriguez *et al.* [12] suggest the presence of two parallel reduction processes:

$$2CuO + H_2 \rightarrow Cu_2O + H_2O$$
$$Cu_2O + H_2 \rightarrow 2Cu + H_2O$$

and

$$CuO + H_2 \rightarrow Cu + H_2O$$

with the first one being dominant at higher temperatures, since the diffraction lines for Cu_2O grew more intense as the reaction temperature increased in isothermal reductions, as compared in Figure 1.9.a-d.

Thus, high reaction temperatures and a limited supply of H_2 favour the appearance of Cu_2O as an intermediate of the reduction process.

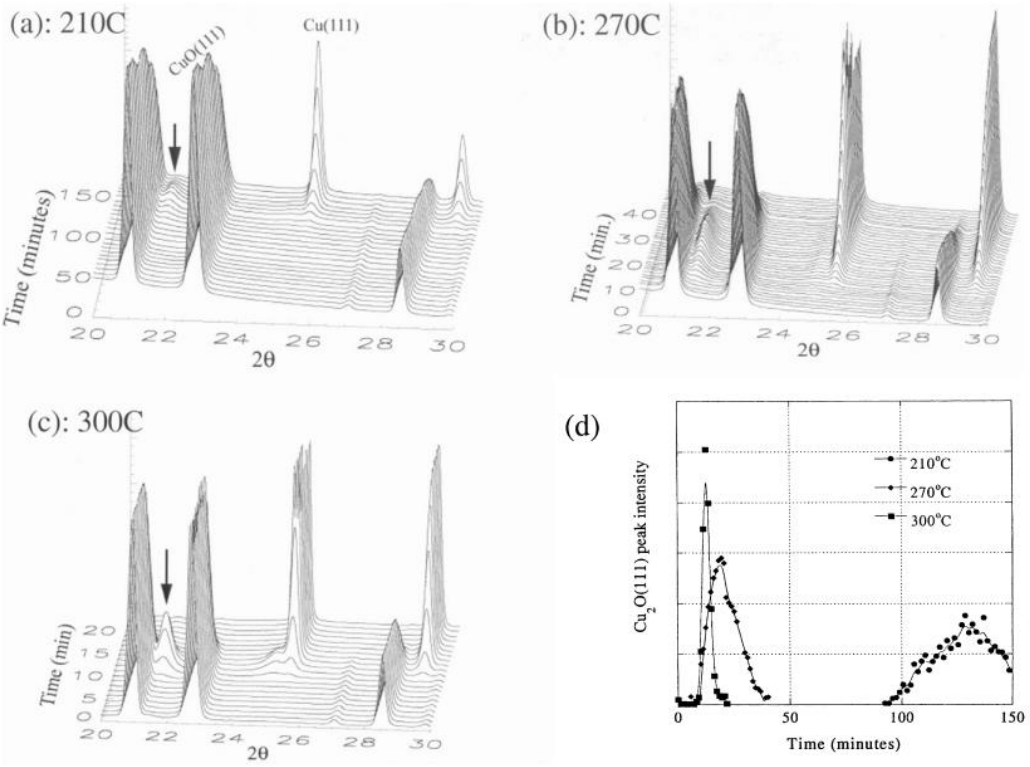

Figure 1.9: *Time-resolved XRD data for the isothermal reduction of CuO under a 5% H_2/95% He mixture (flowrate: ~1 cm^3/min) at three different temperatures:* (a) *210,* (b) *270 and* (c) *300 °C. The arrows indicate the main diffraction lines for Cu_2O.* (d) *intensity of the main diffraction lines for Cu_2O in each case. [12]*

Also Kim *et al.* [14] report that Cu_2O is an unstable copper oxide: indeed, through the combination of TPR and XRD analyses, they evidenced that Cu_2O is formed using high heating rates (e.g. at 20°C/min or 40°C/min), obtaining a greater amount of this oxide with higher heating rates. The formation of more complex oxides such as Cu_4O_3 is instead excluded since its formation would require a substantial distortion in the cell parameters.

Studying CuO slabs, moreover, the authors found that a high pressure of H_2 combined with high concentration of structural defects led to a significant decrease in the induction times. These sites are thought by the authors to be the most active ones for adsorption and dissociation

of H_2, with the latter process being the rate-determining step for the removal of atomic oxygen from the bulk and the formation of the new Cu phase.
It can be suspected that anomalies in the reaction conditions combined with the microscopic structure of the catalyst can lead to different mechanisms of reduction, which are then reflected on the results of the TPR analysis.

1.6 Temperature programmed oxidations (TPO)

As introduced in §1.1, the rationale behind TPO and TPR is equivalent except that the solid is in its reduced form and the reacting mixture is oxidant.
TPO curves describe the consumption of the oxidant component: they are retrieved from experimental tests and peaks are shown where the oxidation rate is higher. The temperature at which the peak is found is the one at which the process takes place.

1.6.1 Cu oxidation

If TPO analyses are made on pure Cu samples, a single peak or more peaks will result according to the mechanism of oxidation involved in the process. To understand if the process is carried out in a single step or through a multiple-step mechanism such as

$$\begin{matrix}(1)\quad 2Cu + 0.5\,O_2 \rightarrow Cu_2O \\ (2)\ Cu_2O + 0.5\,O_2 \rightarrow 2CuO\end{matrix} \qquad (1.22)$$

investigations should be made while analysing the outlet gas composition and the sample evolution over temperature. Rodriguez *et al.* [12] performed XRD studies while oxidizing Cu samples at 300°C for 140 minutes and found that at the end of the process more Cu_2O is produced than CuO, the first one being the dominant oxide. On the other hand, a different situation emerges when XRD analyses are carried out while varying the temperature from 30°C to 600°C: the results shown in Figure 1.10 highlight that Cu_2O is the main oxide and that only CuO is observed at the end.
It is concluded that Cu_2O is a stable species in the process of Cu oxidation, and the most favourable oxidation path is the one reported in Equation (1.22).

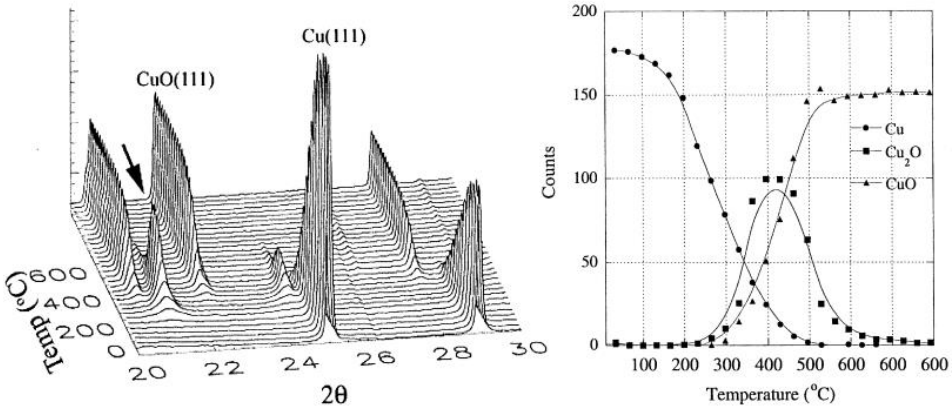

Figure 1.10: *Time-resolved XRD data for the oxidation of Cu under a 5% O_2/95% He mixture (flow rate: ~20 cm^3/min) at 25-600°C and constant 600°C (30 min). The arrow indicates the main diffraction line of Cu_2O. In the right-hand-side graph is shown the variation of the main diffraction lines for Cu, Cu_2O and CuO as function of temperature. [12]*

1.7 Thermal effects

Since both the reduction of CuO and the oxidation of Cu are exothermic reactions, the formulation of a heat balance that describes the thermal gradients over the reactive environment (e.g. the solid bed) is of primary importance in TPR/TPO systems, as unaccounted temperature inhomogeneities would eventually lead to a local increase in the reaction rates and a distorted reaction peak. Moreover, if the temperature at any point of the bed reaches values near the melting point of the reactive solid, the bed sinters and its reactivity is modified irreversibly.

A model that can be used to predict such effects in single particles is the Non-isothermal Changing Grain Size one, which is used by Garcia-Labiano *et al.* [15] to solve coupled mass and energy balances inside some oxygen carriers particles typically used in Chemical Looping Combustion processes. The parameters and conditions used in the simulation are reported in Table 1.1.

Table 1.1: *Parameters and conditions used in the simulation.*

Variable	Reference	Range
Temperature (K)	(Co, Fe, Mn and Ni) 1223	
	(Cu) 1073	
Gas concentration (vol %)		
Oxidation: O_2	21	
Reduction: fuel gas	70	
Particle size (mm)	0.7	0.1-1.0
Particle porosity	0.3	0.1-0.6
Grain size (μm)	0.5	0.1-0.6
Nusselt number	7	2-30

The results of the sensitivity analysis performed by the authors revealed that in every exothermic reactions the temperature of the particles increased quickly in the beginning of the reaction, reaching a maximum (ΔT_{max}) and then decreasing smoothly to the bulk temperature. The possibility of having sintering effects is also excluded, since the ΔT_{max} obtained in every compound studied never raised the particle temperature enough to reach its melting point.
Entering into detail, for the oxidation of Ni at the conditions expressed in Table 1.1 an increase in the particle porosity produced an important increase in the reaction rate, as shown in Figure 1.11.a. This behaviour was attributed to the lower resistance to the gas diffusion in the pore system. On the other hand, the maximum temperature increase is predicted for $\varepsilon = 0.4$, since for higher ε the heat power per unit volume of particle is lower. If the particle diameter is increased, instead, the maximum temperature increase is found for higher particle diameters (namely, for $D_p = 1\ mm$), as Figure 1.11.b shows: this is explained with the increase of the particle surface coupled with the external heat transfer regime, which was computationally proven to be the heat transfer main resistance in the system considered. These results also show that for $D_p < 0.2\ mm$ the reaction rates were almost independent of this variable, and that the thermal gradients within the particle can be neglected without significantly affecting the conversion.

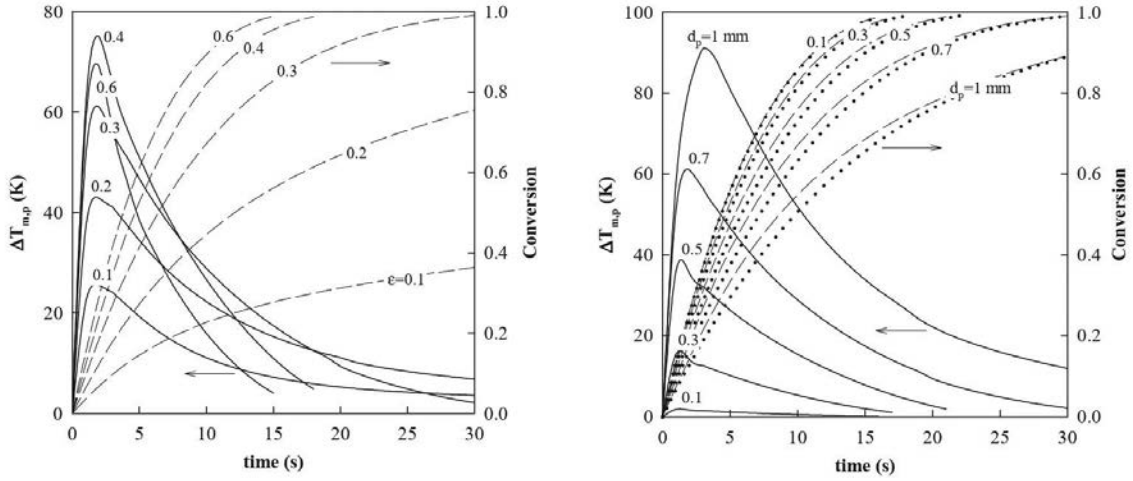

(a) (b)

Figure 1.11: (a) *Effect of the porosity on the maximum temperature increase inside of the particle during the Ni oxidation and* (b) *effect of the particle size on the solid conversion and the maximum temperature increase of the particle for the Ni oxidation reaction (dotted line: isothermal particles).[15]*

Other variables that could affect the heat balance are:

1. the thermal conductivity λ of the gaseous mixture, since high values of λ allows a better heat dissipation;

2. the physical properties of the inert material placed among the reacting solid particles, which should have a high thermal conductivity to allow a better dissipation of the heat generated on the surface of the particles;
3. the Nusselt group of the fluid phase, which determines the heat transfer coefficient and is influenced by the fluid dynamics of the system.

From what have been reported, the identification of thermal gradients in a reactive system is not straightforward and should be evaluated based on its specific physical and chemical characteristics. However, using both a mixture and a diluent having high thermal conductivity will surely help to distribute the reaction heat among the particles of the bed, favouring a more homogeneous reaction.

Chapter 2

Materials and methods

The aim of this chapter is to describe the general procedure, the setup and the instrumentation involved in the sequential TPR-TPO test which were used to determine the parametric sensitivity of the analytical technique. This test consisted of an inert pre-treatment of the cupric oxide sample, followed by an oxidizing pre-treatment and then sequential TPR and TPO analyses. The standard experimental setup and procedure is described in the following paragraphs, but some variations were also applied to study specific aspects of the system and they will be highlighted accordingly in §4.

The setup can be divided into three parts: feed, reaction and analysis section. The components of each part will be described. The complete configuration is shown in Figure 2.1, in which the analysis section depends on the type of experiments.

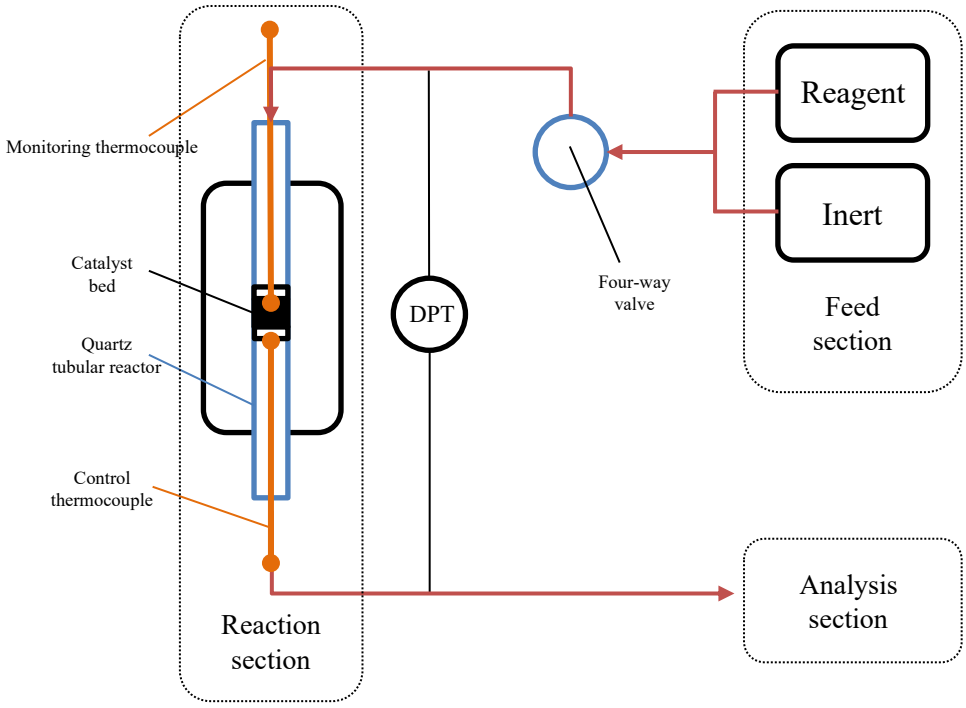

Figure 2.1: *Schematic representation of the setup used to study the parametric sensitivity.*

2.1 Feed section

High accuracy mass flowmeters are used to measure the gases flowrates and a four-way valve is installed to keep reducing and oxidizing gas mixture separated and, most importantly, to prevent the contact between the air and reduced bed when switching from TPR to TPO analysis.

2.1.1 Mass flowmeters

Pure gases from the cylinders are conveyed to manifolds that are connected with the mass flowmeters through polyamide tubes. All the flowmeters have a flow controller based on a calorimetric principle: the control action is performed by measuring the temperature before and after a capillary heated bypass with an electrical resistance. The wire heats up and the temperature difference gives an output signal linked to the gas flowrate by Equation (2.1):

$$V_{signal} = K c_p \rho \Phi_v \tag{2.1}$$

where V_{signal} is the output signal produced, K is a constant factor, c_p is the gas specific heat, ρ is the gas density and Φ_v is the gas volumetric flowrate [16].

These devices are usually calibrated by varying the operating setpoint (e.g. from 5% to 95%) and measuring the flowrate downstream (e.g. through a manual bubble flowmeter) of a single reference gas (N_2). The correct setpoint for different gases can be obtained by adjusting the reference calibration curve with a corrective factor (C) that depends on gas physical proprieties:

$$C = \frac{c_{p,1}\rho_1}{c_{p,2}\rho_2}$$

where subscript 1 refers to the reference gas while subscript 2 refers to the actual gas flowing.

Depending on the type of flowmeter, different Dynamic Data Exchange (DDE) software are used to allow bidirectional connection between flowmeters and Windows applications. In the case of Bronkhorst-type flowmeters, FlowDDE and FLOW-BUS interface are used (Figure 2.2) to directly control and monitor the setpoint and measured value.

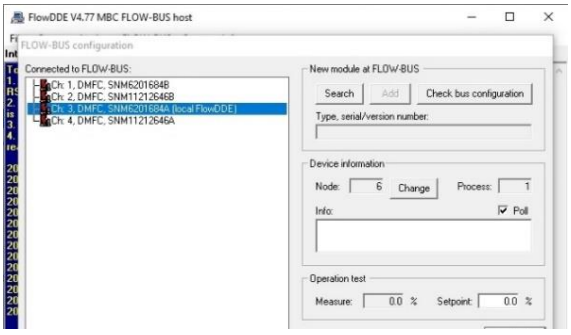

Figure 2.2: *Flow-DDE and its FLOW-BUS interface.*

2.1.2 Four-way valve

Gas sampling valves are normally mounted on gas-chromatographs to perform versatile analyses in which sample loops and column switches are required. In this thesis work, a four-way valve configuration is installed in the feed section to optimize the transition between TPR and TPO analyses. The rotary valve is made of a chamber that has four equally spaced ports paired to each other with micrometric internal lines and, depending on the ports coupling, two valve positions can be identified: ON and OFF. Internal connections can switch from one position to the other by using a two-position air actuator implemented with a solenoid valve assembly that pulses air (5 bar) to the actuator to switch the port connections and redirect the gas flow (Figure 2.3). The solenoid valve is remotely controlled with electrical impulses regulated by a MATLAB® executable program. When performing consecutive TPR-TPO analyses, two inlet ports are specific for reacting mixtures (reducing and oxidizing) while the outlets are connected to the rector and the chemical hood with 1/16" stainless-steel and polyamide lines. During TPR the Position OFF is chosen as the reducing mixture is fed to the reactor while the oxidizing one is discharged, while the Position ON is selected in TPO experiments. This automatized procedure prevents the mixing between gases and avoids the contact of the reduced sample with air (i.e. the spontaneous oxidation).

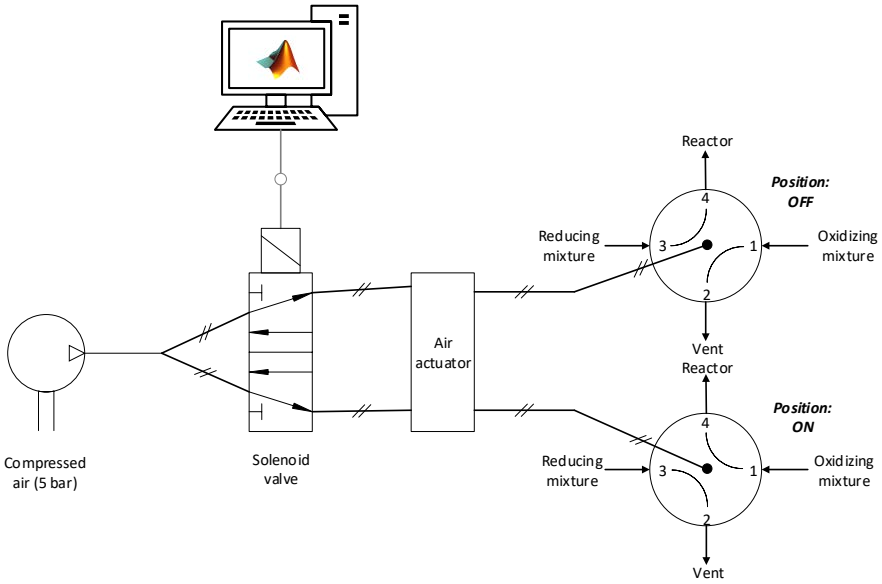

Figure 2.3: *Four-way valve scheme.*

2.2 Reaction section

The reactor setup for the experimental tests is a quartz glass tube with the geometrical parameters reported in Table 2.1. The choice of the internal diameter is crucial to minimize radial concentration and thermal gradients. Quartz glass is chosen for its high chemical inertia,

high melting temperature (about 1400°C) and low thermal expansion coefficient (i.e. for its remarkable ability to undergo rapid temperature changes without cracking).

Table 2.1: *Geometrical parameters of the quartz glass tube.*

Parameter	Symbol	Unit of measure	Value
Internal diameter	D_i	[mm]	6
External diameter	D_e	[mm]	10
Length	L	[cm]	60

A CuO sample of 50 mg, in powder form and with a particle size smaller than 45 μm, is placed in the tube central part to reduce thermal dispersions and it is kept in place with two quartz wool beds. Such quantity of catalyst is chosen so that the resulting bed approximates a monolayer and so to neglect axial diffusion. The tube is then sealed with two junctions that allow the gas flow and the thermocouples fastening. Two thermocouples are positioned inside the reacting system: a monitoring and a control one. The tip of the monitoring thermocouple, with a diameter of 1/16", pierces the upper quartz wool piece and registers the temperature close to the bed surface, which can be approximated to the sample one. The control one is placed under the lower quartz wool bed and registers the reactor internal temperature. With its higher diameter (i.e. 1/8") it also provides physical support to the bed.
An example of copper oxide bed is shown in Figure 2.4.

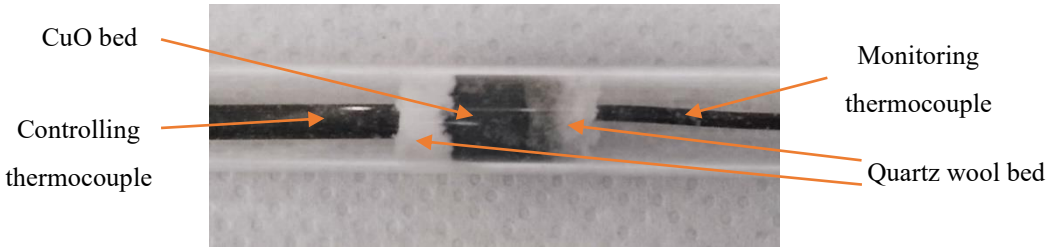

Figure 2.4: *Central part of the loaded reactor.*

Once assembled, the quartz glass tubular reactor is placed inside a cylindrical furnace (Watlow) that heats it through an electrical resistance. The final configuration of the reaction section is shown in Figure 2.5.a and the simulation of the temperature profile which is generated upon heating is shown in Figure 2.5.b. As it can be seen, only in the central part of the furnace the setpoint temperature (i.e. 1000°C) is achieved while thermal gradients arise along the axial direction and thus an isothermal behaviour is guaranteed only in a delimited area. Finally, since the furnace diameter is higher than the external diameter of the tubular reactor, the reactor is fastened with quartz wool pieces, preventing also heat losses due to air currents generated by natural convection.

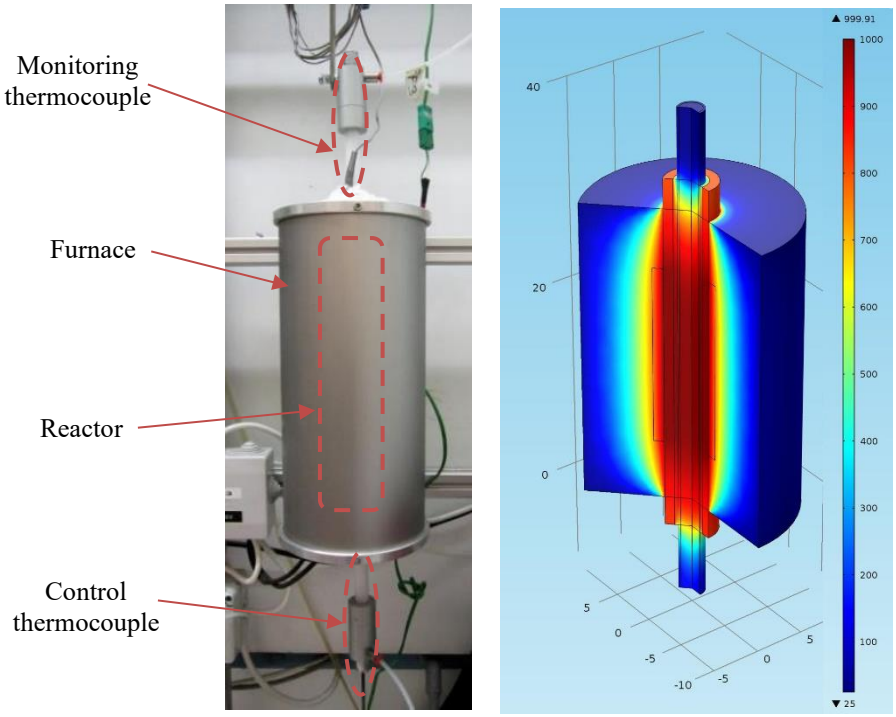

(a) (b)

Figure 2.5: (a) *Reaction section and* (b) *temperature profile simulation of the reactor.*

The power given to the reactor is controlled by a thermal regulator (Omron) with an integrated PID control logic (Figure 2.6.a). The thermal policies are implemented on CX-Thermo commercial software while few parameters (actual temperature, internal set-point, heating power, etc.) are monitored through the TrendViewer interface (Figure 2.6.b). Thermal data retrieved are finally stored in a text file. The monitoring thermocouple data are instead collected and viewed via a dedicated MATLAB® executable file, named Tin8, and stored in a text file. These text files can be read and edited afterwards by the MATLAB® script used for data processing and calculations.

As seen Figure 2.1, a differential pressure transmitter (MPX) is installed so that pressure drops along the reactor are continuously monitored during the cycles. The sensor has a chamber which is split in two by a membrane, each one having its own inlet. The membrane is connected to an electrical resistance and its bending produces a voltage signal (mV) converted into pressure difference (mbar) between the two chambers through a calibration curve. A 0-500 mbar pressure range transmitter model (MPX-5050) is chosen for the studied reactions.

The pressure measurements are then transferred and stored with a data logger device (PicoLog).

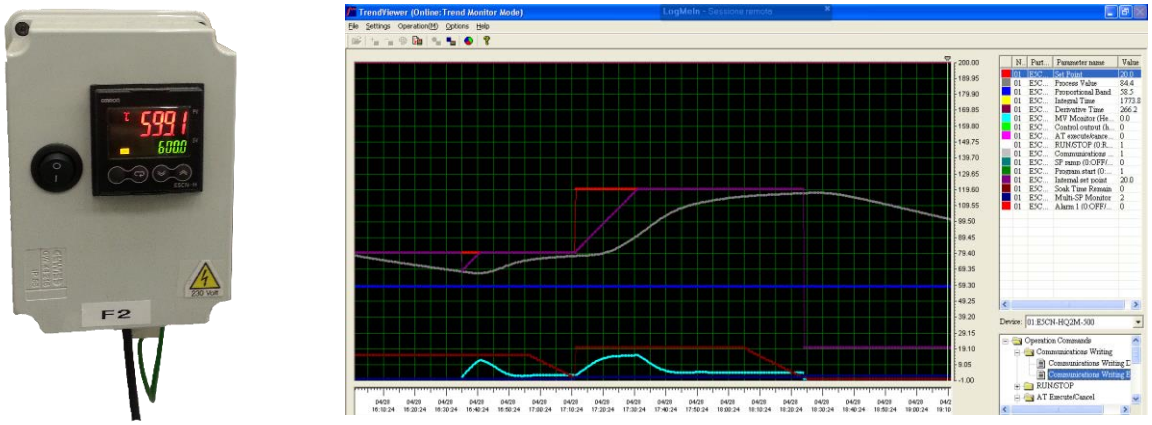

(a) (b)

Figure 2.6: (a) *Thermal regulator and* (b) *CX-Thermo trend viewer interface.*

2.3 Analysis section

The outlet composition is analysed by different instruments according to the reaction carried out, as explained in the introduction. The signals are then processed with MATLAB® to display concentration curves and to quantify the reagent consumed.

2.3.1 Thermal conductivity detector

The Thermal Conductivity Detector (TCD) is a detector installed in the gas-chromatograph Agilent HP-6890 (Figure 2.7.a) that compares the thermal conductivity λ [W/(m K)] of two gas flows (i.e. a pure reference gas and a mixture of the same reference gas and gas containing sample components) and produces an electrical signal (μV) proportional to the difference in λ. The detector cell is divided into two parts, as shown in Figure 2.7.b, one of them containing an electrically heated filament (W-Re) kept at constant temperature (>150°C) with a constant flow of the reference gas (such as Ar, He, N_2). As the analysis is carried out, the sample gas stream alternately flows across the filament (5 times per second) and changes the thermal conductivity by changing the temperature. Therefore, the filament increases its temperature and produces a measurable voltage change. In most chromatographic applications, the sample gas exits from a separation column and the TCD measures the difference in thermal conductivity, i.e. concentration after the calibration process for each component. In this work, H_2 is the only sample gas fed to the system thus no separation columns are required. The advantage of this configuration is the direct injection into the detector cell leading to a high analysis frequency (1 Hz up to 5 Hz) and the absence of temperature/pressure programs to favour single component separation.

Argon is selected as reference gas because its thermal conductivity is much smaller than the H_2 one ($\lambda_{Ar} = 0.016\ \mathrm{W/(m\ K)} < \lambda_{H2} = 0.168\ \mathrm{W/(m\ K)}$ at 25°C). Therefore, the sensibility is

increased even with small variations in H_2 concentration and the curves obtained with low H_2 concentration maintain a good resolution

H_2 calibration curves were performed before each analysis to obtain a linear correlation between the TCD signal and the H_2 fraction at constant volumetric flowrate. Since the signal intensity is dependent upon this last experimental parameter, calibration curves are built for a wide range of flowrates (from 25 to 250 Ncm^3/min) and the R^2 is always greater than 0.998. To confirm their validity, a comparison between reference values ($y_{H2} = 0$ and $y_{H2} =$ inlet concentration) is carried out before each experiment.

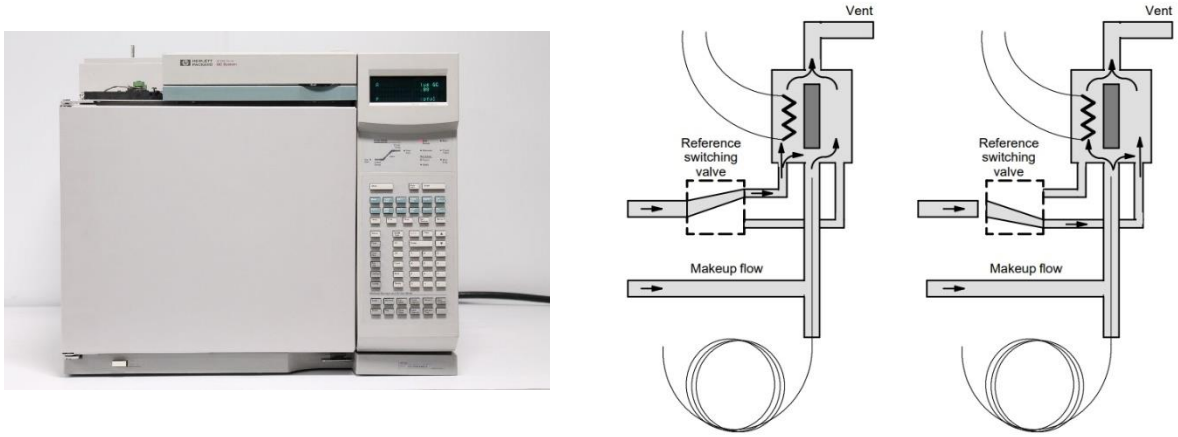

(a) (b)

Figure 2.7: (a) *Agilent HP 6890 and* (b) *TCD cell configurations in the measurement process.*

2.3.2 Mass spectrometer

The mass spectrometer (Hiden HPR 20, Figure 2.8.a) is an instrument that measures the mass-to-charge ratio of ions. Before reaching the detector, the mixture is ionised under high vacuum (~10^{-6} bar) by a stream of electrons that produces ions. These ions are then accelerated by an electric field and then deflected with a magnetic field according to their m/z (i.e. mass to charge) ratio. All the ions with a mass different than the ones to be analysed are diverted, while the ones of interest are focused on a transducer that generates an electrical signal acquired by the computer in terms of partial pressures.

In this experimental campaign the instrument is used in the oxidation analyses, and the masses of molecular oxygen (32 amu), argon (40 amu) and molecular nitrogen (28 amu) are monitored. This last one is considered to account for the oxygen contribution due to air infiltrations into the system.

The output value, provided by Hiden in real time by the software MasSoft (Figure 2.8.b), is the partial pressure of the monitored species: this value should not be considered as a real partial pressure, since even without feeding a component its output partial pressure is different from

zero. For this reason, the reference mass of argon is chosen, and all the partial pressures are scaled on its value during the data processing. The output expressed in terms of scaled partial pressures is then converted into volumetric fraction by a calibration curve with the same procedure used for the TCD, but in this case the dependence on the flowrate is negligible.

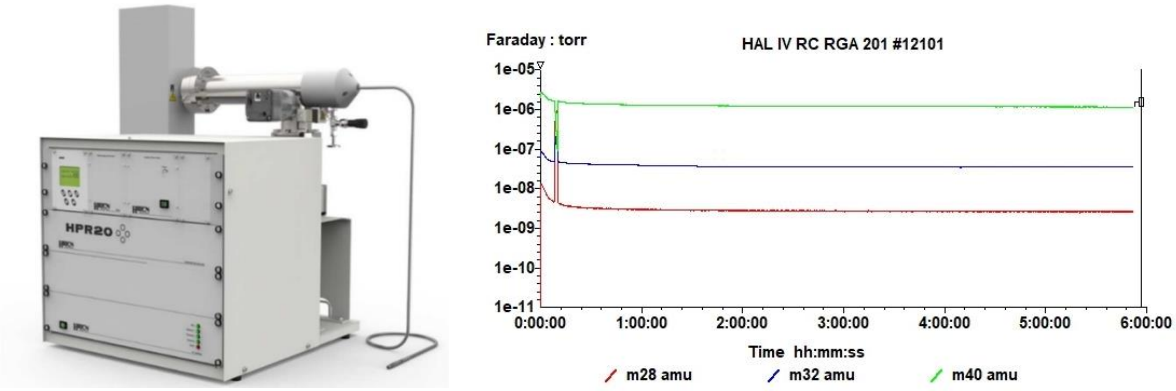

(a) (b)

Figure 2.8: *(a) Hiden HPR 20 mass spectrometer and (b) its scanning for a TPO analysis.*

2.3.3 Oxygen sensor

The oxygen sensor (Alphasense O2-C2, Figure 2.9.a) consists of a galvanic cell equipped with an inlet capillary tube through which the mixture flowrate gets to the cathode. This device operates like a metal/air battery (Figure 2.9.b): the gas mixture reaches the cathode in which the oxygen reduction to hydroxyl ions takes place, and the lead oxidize at the anode. The current generated in this process, which is proportional to the rate of oxygen consumption, is measured by a load resistor between the cathode and the anode and measuring the voltage drop (0-3 V, 0.1-20.9% O_2).

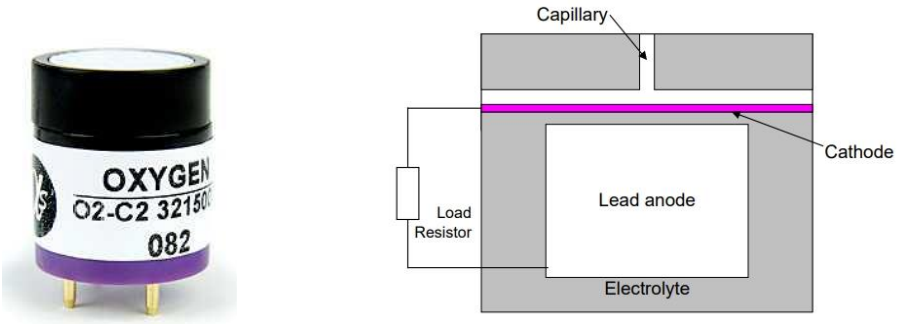

(a) (b)

Figure 2.9: (a) *Alphasense O2-C2 oxygen sensor and* (b) *representation of its components.*

Since the pressure at the cathode decreases as the oxygen is consumed, this pressure drop increases the rate of oxygen diffusion through the capillary. This arises a non-linearity between the output signal and the oxygen concentration, which, however, was insignificant in the narrow composition ranges studied during the experimental campaign.
As declared by the producer [17], the output signal varies also according to the carrier gas, as written in Equation (2.2)

$$V_2 = V_1 \sqrt{\frac{28}{MW}} \tag{2.2}$$

where V_1 is the output signal obtained using N_2 as a carrier and V_2 is the output signal obtained using a different carrier of molecular weight MW. To select the proper carrier gas, the sensor response is analysed by varying the carrier gas in step-input experiments. For each carrier tested, Table 2.2 reports the signal values (S_{O2}) and the time constants τ both for a positive step-input change (from 0% to 5% O_2) and a negative step-input change (from 5% to 2% O_2).

Table 2.2: *O_2 sensor signals and time constants for different carriers and step-input experiments.*

Carrier	S_{O2} (5%) [mV]	τ (0%-5%) [s]	S_{O2} (2%) [mV]	τ (5%-2%) [s]
Ar	850	26	633	17
N_2	870	30	643	17
He	1540	112	911	n. a.

Since the response obtained using helium tended towards high values stabilizing slowly, this carrier has been discarded. Argon and nitrogen, instead, gave similar signal values with the same mixture composition analysed, stabilizing in comparable times both with positive step input changes and negative step input changes. However, considering that the mass spectrometer quantifies the oxygen infiltrating into the system based on the nitrogen content measured, this carrier has been discarded. All things considered, argon has been chosen as the TPO gas carrier.
Calibration curves and their validity are retrieved with the same procedure carried out for H_2, but also in this case the dependence on the flowrate is negligible.

2.4 Second setup

To measure the temperature axial profile of the sample during the thermal cycles, a different setup from the one just described has been used, and is presented in the following section, keeping the same division between the feed one, the reactor one and the analysis one adopted above.

2.4.1 Feed section

The gas is fed to the reaction section thanks to the equipment already described in §2.1, with the only exception that the four-way valve is not used in this case. To prevent the oxidation of the reduced sample the reactor is kept sealed thanks to manual valves.

2.4.2 Reaction section

A picture focusing on its reaction section and its main components is reported in Figure 2.10. The gas path is evidenced in blue.

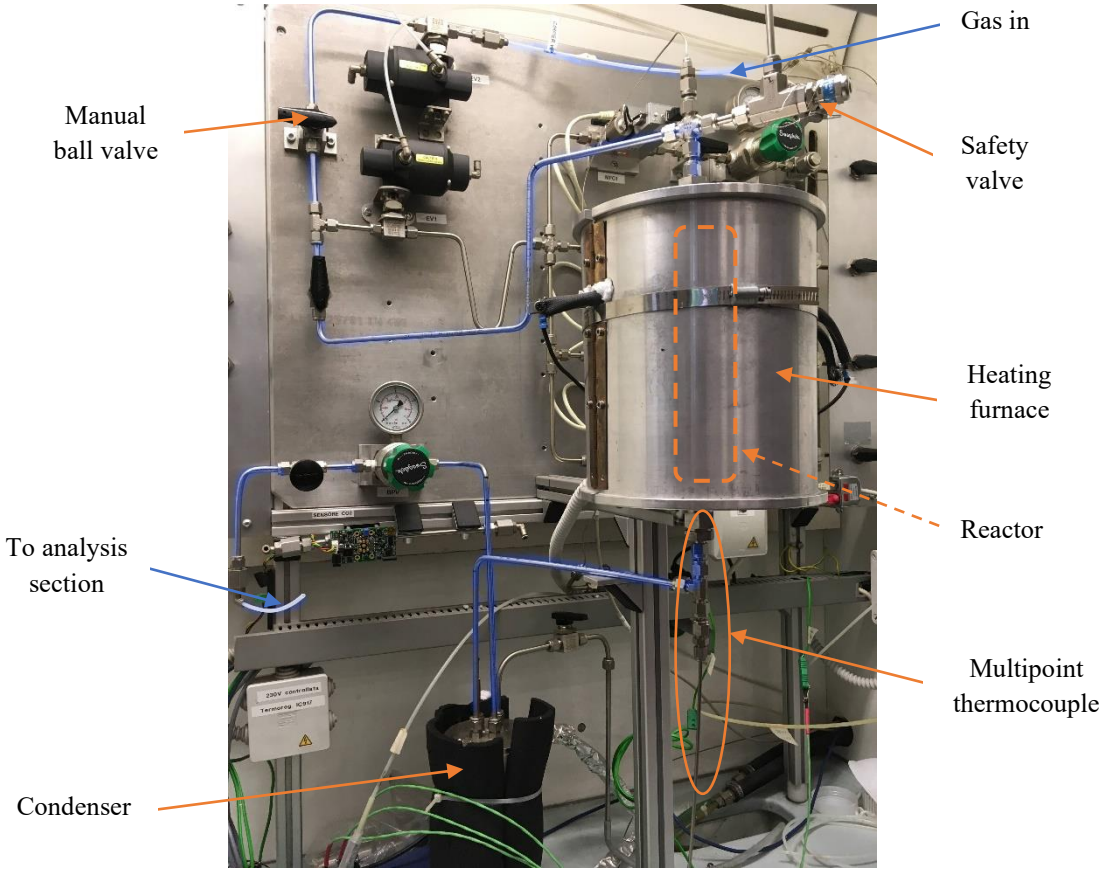

Figure 2.10: *Focus on the second setup reaction section.*

The tests are carried out in a tubular plug-flow reactor consisting of an Inconel (i.e. a steel alloy enriched with nickel) tube with an internal diameter of 12 mm. A multipoint thermocouple with outer diameter of 1/8” is placed inside the reactor, centred in axial position, and allows to gather 10 measurements, one each 5 mm starting from its tip. A bed of quartz wool supports the cupric oxide bed, and its height is chosen to have the thermocouple tip uncovered. This allows to monitor the gas temperature and the sample inner temperature at the same time. A scheme of

the reactor, normally being installed vertically, but here represented horizontally for convenience, is provided in Figure 2.11.

The reactor is then arranged into a tubular furnace consisting of two ceramic heating elements which can supply a maximum power of 550 W. The temperature ramp is controlled by an OMRON thermoregulator through the software CX-Thermo, which works in the same way as described in §2.2. The controlling temperature profile is collected by the software just mentioned, while six of the remaining ones by a MATLAB executable file named TAID and the other three by a Picolog data collector.

The reactor is combined with a pressure transducer that continuously monitors the pressure at its top, whose signal is acquired by the same TAID program. For safety reasons, the reactor is equipped with a vent valve which is calibrated to open when a pressure of 24 bar is reached.

Downstream the reactor, a condenser and a chiller are used during the reduction cycles to separate the water produced from the gases entering the TCD. The condenser consists of a chamber filled with alumina spheres, each one with the diameter of 5 mm, through which the gas passes. Its external jacket is cooled by the continuous flow of a refrigerating liquid (i.e. a mixture of water and glycol) whose temperature is kept at 5°C by the chiller.

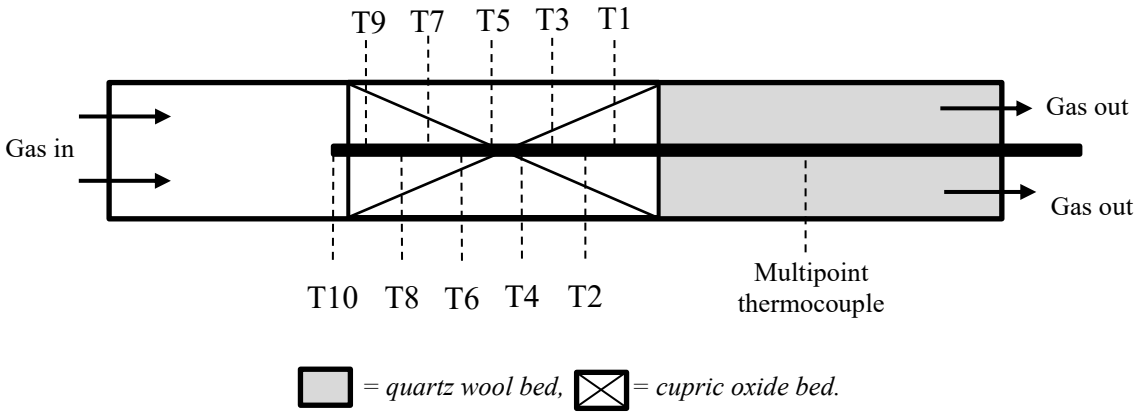

Figure 2.11: *Scheme of the second setup reactor.*

2.4.3 Analysis section

To analyse the outlet mixture composition, the thermal conductivity detector already described in §2.3.1 and the oxygen sensor already described in §2.3.3 are used.

2.5 Experimental procedure

After the reactor has been assembled and put into the furnace as shown in Figure 2.5.a, it is connected through polyamide pipes both to the feed section and the analysis section. The sample is then pre-treated and finally TPR and TPO analyses are performed in sequence. The parameters reported in the following sections are referred to the reference case of the parametric

sensitivity study. Since also specific aspects of the system have been studied in §4, the variation of the parameters of interest will be evidenced in detail in the following chapter.

2.5.1 Pre-treatments

Before running the analyses, the sample is pre-treated in an inert and in an oxidative flow with two separate thermal cycles. The former desorbs possible contaminants (e.g. water or carbonaceous substances) from its surface using a mild temperature ramp, while the latter brings all the particles of the bed in a reducible state. The parameters of each cycle are reported in Table 2.3.

Table 2.3: *Experimental parameters used in the pre-treatment cycles.*

	Inert [-]	**Reagent [-]**	$\dot{V}_{tot}$ **[Ncm³/min]**	y_R **[%]**	**β [°C/min]**	T_{fin} **[°C]**	t_s **[min]**
Inert thermal cycle	Ar	-	50	-	5	200	30
Oxidant thermal cycle	Ar	O_2	50	5	5	250	60

The inert pre-treatment is performed by flowing 50 Ncm³/min ($\dot{V}_{tot}$) of argon into the reactor while the temperature is linearly increased from ambient temperature to 200°C (T_{fin}) with a heating rate of 5°C/min (β). The reactor remains at the final temperature for 30 minutes (t_s), and then cools down naturally to ambient temperature.

After reaching ambient temperature, the oxidative pre-treatment begins: 50 Ncm³/min of oxidant mixture at 5% (y_R) O_2 are flowed in the reactor while the temperature is linearly increased to 250°C with a heating rate of 5°C/min. The reactor is kept at the final temperature for 60 minutes, and finally cools down again to ambient temperature.

During the process, the gas flowrates are controlled by the mass flowmeters and pass through the four-way valve positioned in ON, while the furnace keeps the temperature ramp and the differential pressure transmitter registers the pressure drop through the bed. The oxygen sensor is placed downstream the reactor to detect air infiltrations during the inert pre-treatment, and to detect the possible further oxidation of the bed during the oxidative pre-treatment.

2.5.2 Reductions

After the temperature has reached ambient temperature again, the TPR analysis is carried out with the parameters of Table 2.4.

Table 2.4: *Experimental parameters used in the TPR.*

	Inert [-]	**Reagent [-]**	$\dot{V}_{tot}$ **[Ncm³/min]**	y_R **[%]**	**β [°C/min]**	T_{fin} **[°C]**	t_s **[min]**
TPR	Ar	H_2	50	5	2.5	500	0

The four-way valve switches from ON to OFF position to allow the reducing mixture to enter the reactor. A diluted stream of H_2 in Ar is flowed as the temperature is increased linearly to 500°C with a heating rate of 2.5°C/min. When the final temperature is reached, the reactor is let cool down to ambient temperature naturally. The hydrogen flow is shut off, but a continuous flow of argon is added to prevent the spontaneous oxidation of the reduced sample with air.
The thermal conductivity detector (TCD) is placed after the reactor to monitor the outlet gas composition. Since H_2O is a reaction product and no component separation is made before entering the TCD cell, a silica-gel-trap is added at the reactor outlet to avoid that it negatively affects the analysis.
The signal processing couples the TCD and DPT signals to infer the CuO reduction rate and its effect on the arrangement of the bed.

2.5.3 Oxidations

TPO analysis is performed with the parameters of Table 2.5.

Table 2.5: *Experimental parameters used in the TPO.*

	Inert [-]	**Reagent [-]**	$\dot{V}_{tot}$ **[Ncm³/min]**	y_R **[%]**	**β [°C/min]**	T_{fin} **[°C]**	t_s **[min]**
TPO	Ar	O_2	50	5	2.5	500	0

The four-way valve switches from OFF to ON position to feed the oxidative mixture to the reactor while preventing air infiltration. The copper oxidation is then studied with the same experimental procedure described for reductions.
The analysis section is composed of the oxygen sensor and the mass spectrometer, and the signal produced by both instruments is related to the quantity of O_2 consumed in the oxidation process. Having two instruments linked in series that perform the same task allows to check if anomalies occur during the process. In every case, the oxygen concentration trend detected by the two instruments were consistent with each other, but the quantifications of the oxygen consumed has not always given the same results.

2.5.4 Parametric sensitivity study

To study the parametric sensitivity of the system with respect to the sample mass (m_s), the particle size (d_p), the mixture total volumetric flowrate ($\dot{V}_{tot}$), the reagent concentration (y_R) and the heating rate (β), one of these parameters at a time has been varied in reductions and oxidation cycles, keeping the others as reported in the previous sections. Moreover, also the effect of a bed dilution with silicon carbide of the same particle size range of the CuO sample has been studied combined with the variation of the heating rate β and the volumetric percentage of the reagent. The conditions studied are summarized in Table 2.6.

Table 2.6: *Experimental parameters variation in the parametric sensitivity study.*

	m_s [mg]	d_p [µm]	$\dot{V}_{tot}$ [Ncm^3/min]	y_r [%]	β [°C/min]	y_r [%]	β [°C/min]
Values	10, 50	<45, 100-150, 200-250	25, 50, 100	1, 5, 10	1, 2.5, 5, 10	1, 5, 10	2.5, 5, 10
SiC bed dilution	No	No	No	No	No	Yes	Yes

2.6 Signal analysis

As the analyses are performed (i.e. reductions and oxidations), one or more peaks are observed in the output signal of the analytical instruments, which are connected to the main reactions and processes occurring in the system at the explored temperatures.

All the signals produced by the laboratory instrumentation are coupled with the acquisition date and time: this allows their synchronization, which is made through an ad-hoc MATLAB® script. The synchronization process accounts also for the dead time (θ) between the reactor and the analytical instrument, and is calculated through (2.3)

$$\theta\ [min] = \frac{V_{pipe}}{\dot{V}_{tot}} \tag{2.3}$$

where V_{pipe} is the volume of the pipe that connects the reactor to the analytical instrument and $\dot{V}_{tot}$ is the gas volumetric flowrate, assumed constant throughout the process. The signals are then overlapped and plotted against time, allowing to retrieve the times that will be later used in the quantification process (i.e. the beginning and the end of the peak, t_{in} and t_{fin}).

The TCD signal, O_2 sensor signal and mass spectrometer output overlapped to the temperature profile are shown in Figure 2.12.a, Figure 2.12.b and Figure 2.12.c respectively. Through the calibration curve, the signals are then converted into the reagent gas concentration, and their profile over time is obtained.

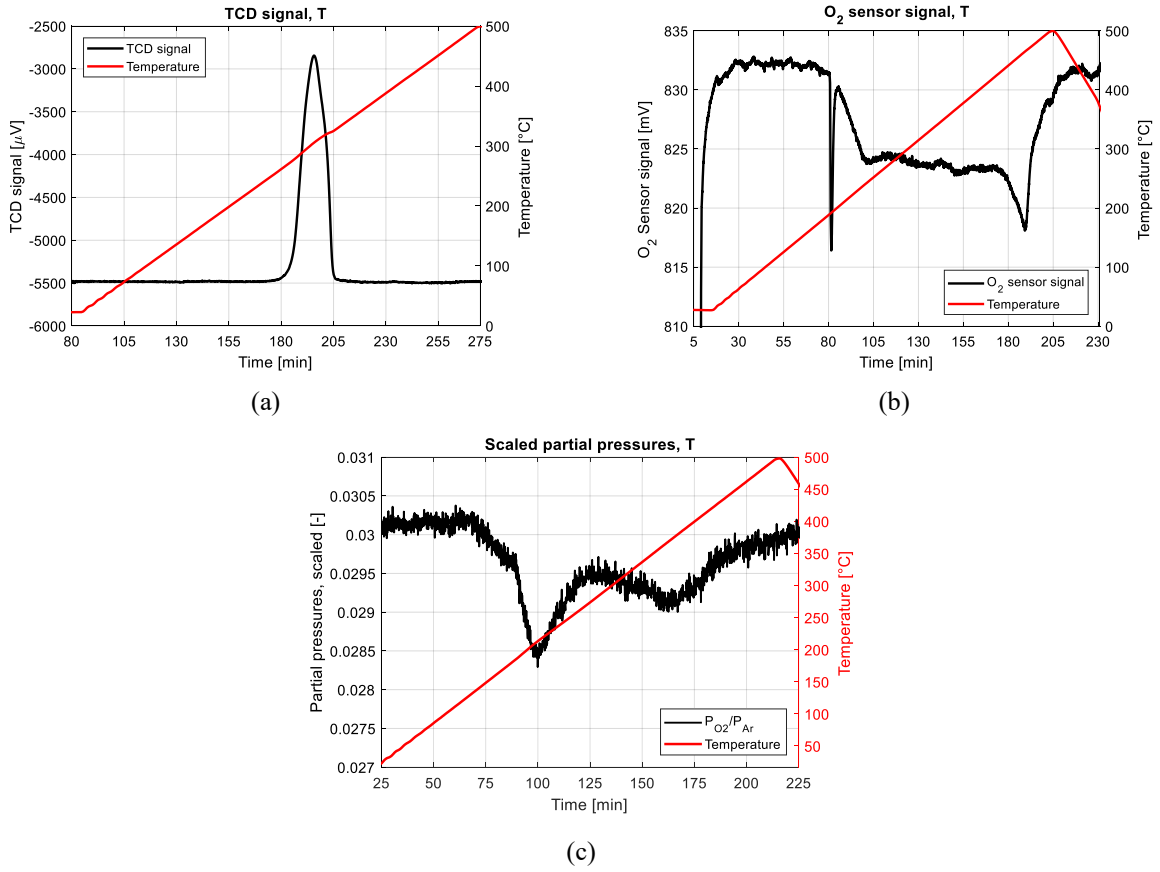

Figure 2.12: (a) *TCD signal,* (b) *oxygen sensor signal and* (c) *oxygen scaled partial pressure trends over time.*

2.7 Quantification of the reagent consumed

TPR analyses also provide information on the quantity of reducing gas consumed during the reduction (i.e. the amount of reducible species and metal oxidation state). The quantification procedure is described in the following equations (from (2.4) to (2.9)). Since the process is carried out at ambient pressure and high temperatures are explored, the ideal gas behaviour is supposed to hold.

The inlet molar fraction of H_2 (y_{H2}^{in}) is calculated as in Equation (2.4):

$$y_{H2}^{in}[-] = \frac{\dot{V}_{H2}^{in}}{\dot{V}_{tot}^{in}} \tag{2.4}$$

where $\dot{V}_{H2}^{in}$ is the inlet hydrogen volumetric flowrate and $\dot{V}_{tot}^{in}$ is the inlet total volumetric flowrate, both of them retrieved from experimental measurements (e.g. through a manual bubble flow meter). The inlet total molar flowrate ($\dot{n}_{tot}$), which is assumed constant during the whole process since diluted mixtures are used, is then calculated as in Equation (2.5):

$$\dot{n}_{tot}\left[\frac{mol}{min}\right] = \frac{P\dot{V}_{tot}^{in}}{R_g T} \tag{2.5}$$

where P is ambient pressure, R_g is the universal gas constant and T is ambient temperature. The inlet hydrogen molar flowrate ($\dot{n}_{H2}^{in}$) is calculated combining Equation (2.4) and Equation (2.5) through Equation (2.6):

$$\dot{n}_{H2}^{in}\left[\frac{mol}{min}\right] = y_{H2}^{in} \cdot \dot{n}_{tot} \tag{2.6}$$

The outlet hydrogen molar flowrate ($\dot{n}_{H2}^{out}$), variable in time, is defined as in Equation (2.7):

$$\dot{n}_{H2}^{out}(t)\left[\frac{mol}{min}\right] = y_{H2}^{out}(t) \cdot \dot{n}_{tot} \tag{2.7}$$

where $y_{H2}^{out}(t)$ is the molar fraction of hydrogen, whose values are retrieved from the transformation of the TCD electrical signal (mV) into molar fractions with the calibration curve. The consumed hydrogen molar flowrate ($\dot{n}_{H2}^{cons}$) is calculated by combining Equation (2.6) and Equation (2.7) through Equation (2.8):

$$\dot{n}_{H2}^{cons}(t)\left[\frac{mol}{min}\right] = \dot{n}_{H2}^{in} - \dot{n}_{H2}^{out}(t) \tag{2.8}$$

The $\dot{n}_{H2}^{cons}(t)$ integration over the time subtended by the peak (Equation (2.9)) gives the total hydrogen consumed in the reduction (n_{H2}^{cons})

$$n_{H2}^{cons}[mol] = \int_{t_{in}}^{t_{fin}} \dot{n}_{H2}^{cons}(t)dt \tag{2.9}$$

To correlate the consumption of H_2 to the consumption of the CuO atomic oxygen, the reaction stoichiometry should be considered:

$$CuO_{(s)} + H_{2\,(g)} \rightarrow Cu_{(s)} + H_2O_{(g)}$$

obtaining that for 1:1 ratio

$$n_{O,CuO}^{cons}[mol] = n_{H2}^{cons}$$

The degree of reduction is finally calculated as:

$$\%_{O,CuO}^{cons}[\%] = \frac{n_{O,CuO}^{cons}}{n_{O,CuO}^{0}} \cdot 100 \tag{2.10}$$

being $n_{O,CuO}^{0}$ the moles of atomic oxygen into the CuO sample before the first reduction.

The same procedure is applied for the TPO analysis, in which the gas of interest is O_2, and the equations to be used are the same of Equation (2.4)-(2.9). Since the Cu oxidation is expressed as

$$Cu_{(s)} + 0.5\ O_{2(g)} \rightarrow CuO_{(s)}$$

the atomic oxygen $n_{O,CuO}^{reg}$ regained by the sample through oxidation is calculated as in Equation (2.11)

$$n_{O,CuO}^{reg}[mol] = \frac{n_{O2}^{cons}}{0.5} \tag{2.11}$$

and the degree of oxidation is calculated through Equation (2.12)

$$\%_{O,CuO}^{reg}[\%] = \frac{n_{O,CuO}^{reg}}{n_{O,CuO}^{0}} \cdot 100 \tag{2.12}$$

When reduction and oxidation cycles are performed in series, the comparison between the values of $\%_{O,CuO}^{cons}$ and $\%_{O,CuO}^{reg}$ are used to assess if the reactions are complete.

Chapter 3

Parametric sensitivity

The effect of different experimental parameters and combinations on CuO reduction/oxidation profiles has been investigated as described in §2. The objective is to demonstrate that standardized protocols and parameters for TPR and TPO lead to a loss of information on the system reactivity and on potential mass transfer limitations, even in the case of a model reaction such as CuO reduction with H_2 (Equation (3.1)) and oxidation with O_2 (Equation (3.4)).
In this chapter, the influence of different experimental parameters and some major combinations (Table 3.1) will be presented by analysing the peak shapes, maximum temperature, reduction and oxidation degree (i.e. atomic oxygen from CuO consumed/regained) and the comparison between literature results in terms of Baiker parameter (K) will be discussed.

***Table 3.1**: Experimental parameter varied.*

Parameter	Symbol
Sample mass	m_s
Particle size width	d_p
Total mixture volumetric flowrate	$\dot{V}_{tot}$
Reducing/oxidizing agent volumetric percentage	y_r
Heating rate	β
SiC dilution	-

3.1 Temperature programmed reductions (TPR)

The global reaction considered is the reduction of CuO with H_2 [15]:

$$CuO_{(s)} + H_{2\,(g)} \rightarrow Cu_{(s)} + H_2O_{(g)}\,,\ \Delta H_R^0 = -85.763\ \frac{KJ}{mol\ CuO} \qquad (3.1)$$

The experimental parameters varied are shown in Table 3.2. The results will be presented evidencing:

1. the hydrogen flowrate fed ($\dot{n}_{H2}^{in}$), as it defines the maximum hydrogen consumption achievable in the test;
2. the calculated K parameter (refer to Equation (1.19));
3. the activation temperature (T_{act}), defined as the temperature at which the hydrogen consumption becomes positive;
4. the temperature at which the maximum hydrogen consumption is observed (T_{peak});
5. the temperature at which shoulders are detected (T_s);
6. the temperature range in which the peak develops (Peak width);
7. the sample total oxygen consumed ($n_{O,CuO}^{cons}$);
8. the degree of reduction ($\%_{O,CuO}^{cons}$).

The reference case, obtained by analysing a 50-mg sample under 50 Ncm^3/min of mixture at 5% hydrogen concentration, using a particle size <45 μm and a heating rate of 2.5°C/min, will be always shown with an orange curve in the plot.

***Table 3.2**: TPR experimental parameters variation.*

Parameter	Symbol	Unit of measure	Values	SiC dilution
Sample mass	m_s	[mg]	10, **50**	No
Particle size width	d_p	[μm]	**<45**, 100-150, 200-250	No
Total mixture volumetric flowrate	$\dot{V}_{tot}$	[Ncm^3/min]	25, **50**, 100	No
Hydrogen volumetric percentage	y_{H2}	[%]	1, **5**, 10	No
Heating rate	β	[°C/min]	1, **2.5**, 5, 10	No
Hydrogen volumetric percentage	y_{H2}	[%]	1, 5, 10	Yes
Heating rate	β	[°C/min]	2.5, 5, 10	Yes

As Table 3.2 shows, the effect of the hydrogen concentration and the heating rate have been studied also diluting the bed with silicon carbide. This choice has been done because its addition increases the heat distribution among the bed thanks to its excellent thermal properties, evidenced in Table 4.19. In parallel, it also delays the agglomeration of the bed, which could cause barriers of diffusional type. The dilution has been done keeping a ratio of 1:1 on mass basis, using the same particle size of the CuO analysed not to affect the bed fluid-dynamics. Its effect on the sample reactivity is then explored under the experimental conditions reported in Table 3.2.

3.1.1 Sample mass effect (m_s)

The effect of the sample mass on the TPR profile is shown in Figure 3.1 and Table 3.3. The TPR profile of the reference case is also reported to underline the similarities between the activation temperatures identified in the two 50-mg samples.

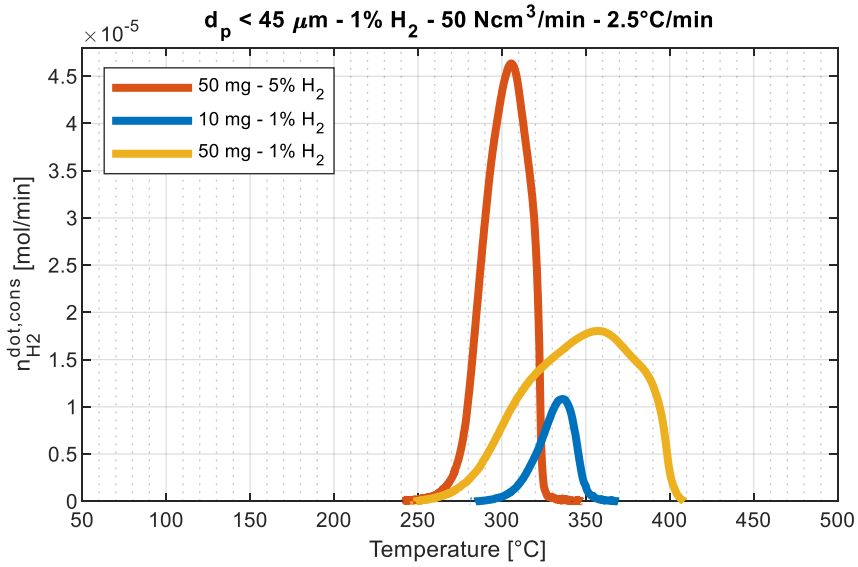

***Figure 3.1**: Sample mass influence on TPR profiles.*

***Table 3.3**: Relevant data concerning the sample mass variation.*

m_s [mg]	y_{H2} [%]	$\dot{n}_{H2}^{in}$ [mol/min]	K [s]	T_{act} [°C]	T_{peak} [°C]	T_s [°C]	Peak width [°C]	$n_{O,CuO}^{cons}$ [mol]	$\%_{O,CuO}^{cons}$ [%]
10	1	$2.08 \cdot 10^{-5}$	359	291	337	-	52	$1.15 \cdot 10^{-4}$	90.6
50	1	$2.08 \cdot 10^{-5}$	1832	251	358	315, 385	163	$6.14 \cdot 10^{-4}$	96.7
50	5	$1.04 \cdot 10^{-4}$	366	248	305	320	79	$5.89 \cdot 10^{-4}$	92.8

As the gathered data evidences, a greater mass of sample under the same experimental conditions produces a broader peak and shifts the reaction activation and the maximum hydrogen consumption at higher temperatures.

The enlargement of the peak could be explained with the creation of the copper layer on the unreacted particle, which are predicted by the models presented in §1.2.2.1 and §1.2.2.2 and observed experimentally by Kim *et al.* [14], and, in parallel, to the bed agglomeration which has been observed in all the tests (see §3.3). This layer covers the surface of the CuO particles as soon as they start reducing, adding a diffusional resistance to the reactive process. Since the main driving force for diffusion is the concentration gradient of gaseous reagent (in this case, between the outer and the inner copper interface), a lower hydrogen concentration will slow

down the entire process, resulting in larger peaks. This is observed in the two 50-mg samples (orange curve and blue curve in Figure 3.1), which activate at almost the same temperatures and react with similar rates in the first 10°C, but then reduce at considerably different rates. The 10-mg sample, on the other hand, could have reduced faster because of the lower bed height (the same reactor diameter has been used for all the tests) and lower bed packing, both leading to a lower diffusional resistance.

The shoulders observed at T_s in the 50-mg profiles could be connected to the release of trapped hydrogen (see §1.5.2), or by a change in the reaction mechanism, involving lower copper oxides or other compounds, such as copper hydride or hydroxide (see §1.5.3). As observed by Rodriguez *et al.* [12], the establishment of severe conditions (i.e. 5% H_2 in 1 Ncm^3/min of mixture) favours the Cu_2O formation, and so a two-step reduction mechanism, which will result in additional peaks. It could be possible that these conditions establish also in the 50-mg sample reduced at 1% H_2, probably when the hydrogen fed is mostly consumed (from T=315°C to T=385°C approximately), so favouring its formation and a two-step reduction process.

It is interesting to observe that using higher masses the activation temperature is lower (i.e. 40-43°C less when using a sample of 50 mg instead of 10 mg). In this case it can be guessed that the reaction occurs even at lower temperatures, but the heat of reaction is not retained in the subtle layer of the 10-mg cupric oxide, being flowed away by the feed mixture. This fact could prevent the required activation energy to be reached by most of the particles which, as they do not react, does not even provide energy to the system, shifting the reaction towards higher temperatures.

The quantifications suggest that a higher reduction degree is achieved by using higher masses, which is counterintuitive. Probably the cause lies in experimental errors.

3.1.2 Particle size effect (d_p)

The particle size effect on the TPR profile is shown in Figure 3.2 and Table 3.4. The mass of sample used has been kept equal in all the three cases reported.

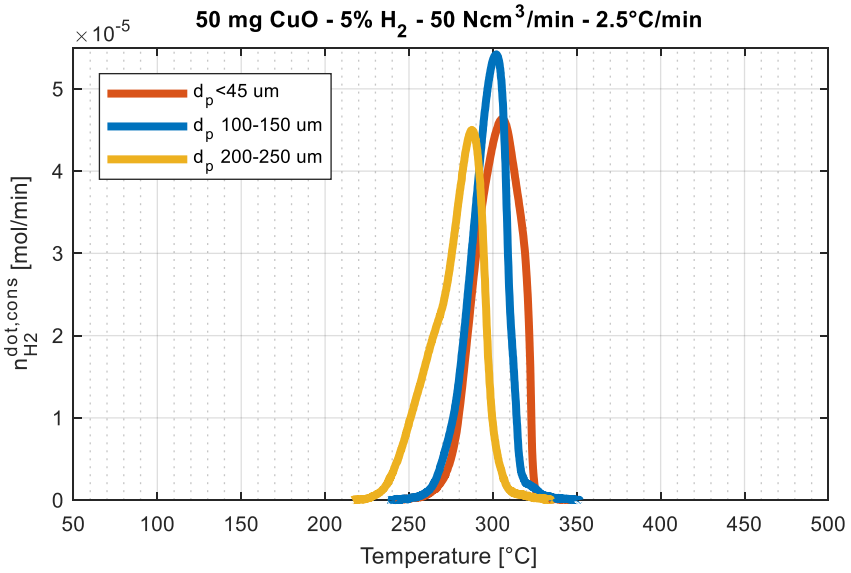

***Figure 3.2**: Sample particle size influence on TPR profiles.*

***Table 3.4**: Relevant data concerning the sample particle size variation.*

d_p [µm]	$\dot{n}_{H2}^{in}$ [mol/min]	K [s]	T_{act} [°C]	T_s [°C]	T_{peak} [°C]	Peak width [°C]	$n_{O,CuO}^{cons}$ [mol]	$\%_{O,CuO}^{cons}$ [%]
<45	$1.04 \cdot 10^{-4}$	366	241	318	305	79	$5.89 \cdot 10^{-4}$	92.8
100-150	$1.04 \cdot 10^{-4}$	371	240	274	302	85	$5.46 \cdot 10^{-4}$	86.1
200-250	$1.04 \cdot 10^{-4}$	375	229	270	288	96	$5.61 \cdot 10^{-4}$	88.4

As the data show, an increase in the peak width and a decrease in the peak temperature is observed when larger particle are used. As reported by Fierro *et al.* [10] a broader peak is associated with a lower surface area of the sample, which is in accordance with the results obtained. On the other hand, the shift of the whole peak towards slightly higher temperatures when decreasing the particle size suggests that the reagent diffusion through the bed is hindering. This could be an effect of the higher bed packing of the first and the second cases, the first being evidenced by the high polydispersity of the bed particles (see Figure 4.10.b). The higher bed packing, resulting in a smaller ε_{bed}, will indeed lower the effective hydrogen diffusion coefficient $D_{eff,H2}$ as in Equation (3.2)

$$D_{eff,H2} = D_{g,H2} \cdot \frac{\varepsilon_{bed}}{\tau} = D_{g,H2} \cdot \varepsilon_{bed}^{\frac{1}{3}} \tag{3.2}$$

where $D_{g,H2}$ is the diffusion coefficient of hydrogen, accounting for the reagent diffusion into the inert and for the Knudsen diffusion, and τ the tortuosity of the bed passages. As higher temperatures are reached, the effective diffusion coefficient will rise, promoting the reduction of the bed.

The shoulder which is evident using higher particle sizes could be connected to a different reaction mechanism than the one proposed in §3.1, or to the beginning of the agglomeration.

The quantifications results do not suggest any trend, but the observations made above underlines the importance of preventing intraparticle mass transfer limitations by having a particle size distribution as narrow as possible.

3.1.3 Mixture volumetric flowrate effect ($\dot{V}_{tot}$)

The particle size effect on the TPR profile is shown in Figure 3.3 and Table 3.5.

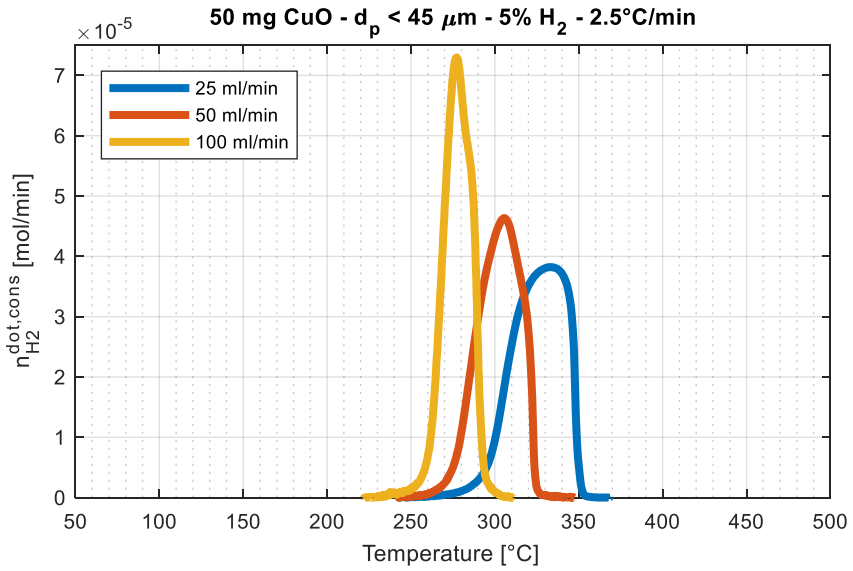

***Figure 3.3**: Mixture volumetric flowrate influence on TPR profiles.*

***Table 3.5**: Relevant data concerning the mixture volumetric flowrate variation.*

$\dot{V}_{tot}$ [Ncm^3/min]	$\dot{n}^{in}_{H2}$ [mol/min]	K [s]	T_{act} [°C]	T_s [°C]	T_{peak} [°C]	Peak width [°C]	$n^{cons}_{O,CuO}$ [mol]	$\%^{cons}_{O,CuO}$ [%]
25	$5.20\cdot10^{-5}$	714	247	-	334	93	$6.29\cdot10^{-4}$	99.1
50	$1.04\cdot10^{-4}$	366	248	318	305	79	$5.89\cdot10^{-4}$	92.8
100	$2.08\cdot10^{-4}$	180	230	290	277	63	$6.04\cdot10^{-4}$	95.2

As shown above, when increasing the total mixture volumetric flowrate, the peak width decreases together with the peak temperature. The profile shapes obtained in this case could be caused by the variation of the reagent molar amount fed ($\dot{n}_{H2}^{in}$) in parallel with a change in the fluid-dynamic of the system and in the external mass transfer coefficient.
As the reaction progresses, the hydrogen concentration in the mixture drops quicker in the case of a lower volumetric flowrate with the same inlet hydrogen concentration, because the quantity of hydrogen fed is lower. This will lower the reaction rates, as observed in the three profiles, and slow down the reaction. Moreover, since the reagent diffusion through the layer of copper is hindered by the lower driving force (i.e. the decrease in concentration gradient), the reduction of the whole sample is further slowed, and the peak temperature is shifted towards higher values.
In addition, using lower volumetric flowrates will favour the hydrogen dispersion in the mixture exiting the reactor, as the time required for the mixture to travel to the analyser increases. This will result in an increase of the hydrogen concentration distribution variance, and so in a broader peak.
Moreover, the development of a slower reaction in the case of using low fluid velocities (i.e. lower volumetric flowrates) suggests that also external mass transfer limitations are present. Since the external mass transfer coefficient $h_{m,H2}$ dependence upon the system and the fluid properties could be expressed as in Equation (3.3)

$$h_{m,H2} \propto \left(\frac{v_{rel}}{d_p}\right)^{1/2} D_{H2,mix}^{2/3} \nu_{mix}^{-1/6} \tag{3.3}$$

where v_{rel} is the relative velocity of the fluid with respect to the particles, d_p is the particle diameter, $D_{H2,mix}$ is the effective H_2 diffusion coefficient in the binary mixture fed, and ν_{mix} its kinematic viscosity, a higher mixture velocity will result in a higher $h_{m,H2}$. The mass transfer coefficient increase will then promote the reaction, which will occur at lower temperatures, as shown in Figure 3.3.
Like observed in 3.1.1, a shoulder is detected also in the profile obtained when flowing 100 Ncm^3/min of mixture: as explained in §1.5.2 and in §1.5.3, this could derive from the development of a different reaction mechanism than the one proposed.
The quantifications do not suggest any trend, but taking into account the considerations made up to now, using a higher volumetric flowrate is generally recommended, since the peak shape is less influenced by the fluid-dynamics.

3.1.4 Inlet hydrogen concentration effect (y_{H2})

The inlet hydrogen concentration effect on the TPR profile, obtained with and without the bed dilution as explained in §3.1, is shown in Figure 3.4 and Table 3.6.

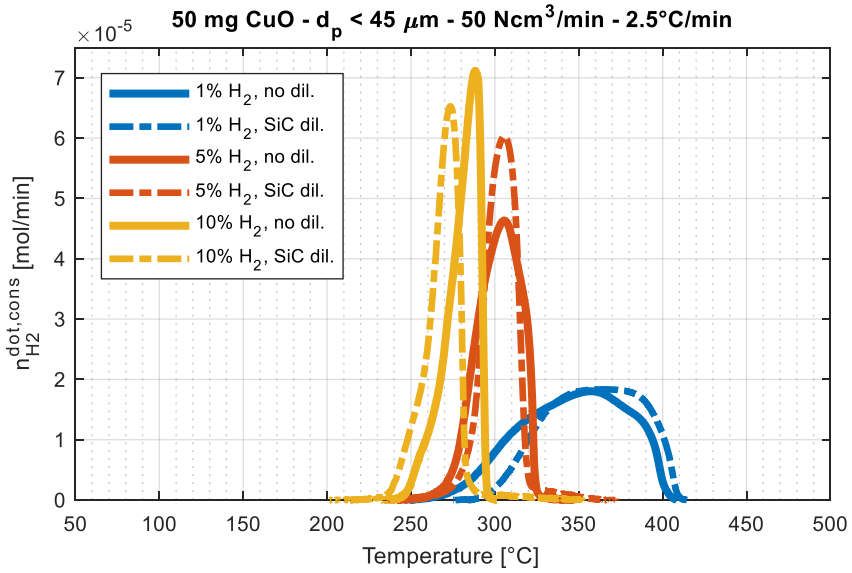

***Figure 3.4**: Inlet hydrogen concentration influence on TPR profiles.*

***Table 3.6**: Relevant data concerning the inlet hydrogen concentration variation.*

y_{H2}^{in} [%]	$\dot{n}_{H2}^{in}$ [mol/min]	K [s]	T_{act} [°C]	T_s [°C]	T_{peak} [°C]	Peak width [°C]	SiC dilution	$n_{O,CuO}^{cons}$ [mol]	$\%_{O,CuO}^{cons}$ [%]
1	$2.08 \cdot 10^{-5}$	1831	251	315, 385	358	163	-	$6.14 \cdot 10^{-4}$	96.7
5	$1.04 \cdot 10^{-4}$	366	248	318	305	79	-	$5.89 \cdot 10^{-4}$	92.8
10	$2.08 \cdot 10^{-4}$	184	240	270	288	67	-	$5.41 \cdot 10^{-4}$	85.3
1	$2.08 \cdot 10^{-5}$	1908	270	-	369	131	Yes	$5.67 \cdot 10^{-4}$	89.3
5	$1.04 \cdot 10^{-4}$	368	245	320	306	76	Yes	$5.78 \cdot 10^{-4}$	91.1
10	$2.08 \cdot 10^{-4}$	184	230	260	273	63	Yes	$6.00 \cdot 10^{-4}$	94.5

As the data above show, using a higher hydrogen concentration without a silicon-carbide bed dilution markedly decreases the peak temperature T_{peak} and the peak width, underlining a higher activity. The significantly faster hydrogen consumption at lower temperatures obtained with a 10% hydrogen mixture, moreover, proves that diffusion through the copper shell is limiting from the beginning of the reaction, as already explained in §3.1.1. The higher concentration gradients that establishes in this case, indeed, favours the hydrogen inward diffusion, resulting in a faster reduction and in a narrower peak. On the other hand, when this contribution is not enough large (i.e. when feeding a 5% H_2 mixture), the peak rises at higher temperatures because diffusion is improved by temperature. This favours the inward hydrogen diffusion and so the reduction of the core. In the case of feeding a 1% hydrogen mixture, the diffusion is furtherly hindered, and a broader peak is produced.

Using a silicon carbide bed dilution as explained in §3.1 improves the solid reactivity when using higher hydrogen concentrations. In the case of feeding a 10%-H_2 mixture the peak is shifted towards lower temperatures and is narrower with respect to the non-diluted case, while feeding a 5%-H_2 mixture makes it just narrower. In both cases, the SiC high thermal conductivity helped to spread the reaction heat in the sample, promoting a more uniform reduction. Moreover, its capability of delaying the agglomeration process (see §4.4) could have mitigated the surface area decrease of the sample, resulting in a faster kinetic. At contrary, the combination of low hydrogen concentrations and a bed dilution seems to be detrimental, as the peak is shifted towards higher temperatures. On the other hand, a peak free of shoulders is obtained, meaning that the reaction is carried out with the mechanism of Equation (3.1).
Recalling the observations made in §3.1.1 about the high $\%_{O,CuO}^{cons}$ obtained with a low hydrogen concentration, the quantifications confirms that combining a high hydrogen concentration in the feed coupled with a silicon carbide bed dilution provides better results, as the degree of reduction of the bed is higher.

3.1.5 Heating rate effect (β)

The inlet hydrogen concentration effect on the TPR profile, obtained with and without the bed dilution as explained in §3.1, is shown in Figure 3.5 and Table 3.7.

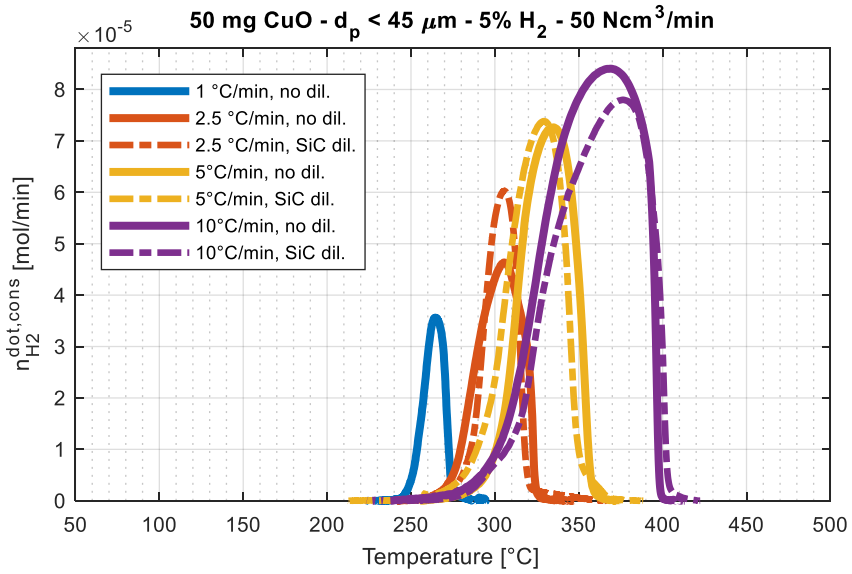

***Figure 3.5**: Heating rate influence on TPR profiles, with and without SiC dilution.*

***Table 3.7**: Relevant data concerning the heating rate variation.*

β [°C/min]	$\dot{n}_{H2}^{in}$ [mol/min]	K [s]	T_{act} [°C]	T_{peak} [°C]	Peak width [°C]	SiC dilution	$n_{O,CuO}^{cons}$ [mol]	$\%_{O,CuO}^{cons}$ [%]
1	$1.04 \cdot 10^{-4}$	367	230	264	58	-	$5.53 \cdot 10^{-4}$	87.1
2.5	$1.04 \cdot 10^{-4}$	366	241	305	79	-	$5.89 \cdot 10^{-4}$	92.8
5	$1.04 \cdot 10^{-4}$	367	240	334	126	-	$5.63 \cdot 10^{-4}$	88.8
10	$1.04 \cdot 10^{-4}$	363	256	368	144	-	$5.79 \cdot 10^{-4}$	91.2
2.5	$1.04 \cdot 10^{-4}$	368	240	306	76	Yes	$5.78 \cdot 10^{-4}$	91.1
5	$1.04 \cdot 10^{-4}$	367	239	330	122	Yes	$6.03 \cdot 10^{-4}$	95.0
10	$1.04 \cdot 10^{-4}$	358	244	377	165	Yes	$5.44 \cdot 10^{-4}$	85.8

As shown above, an increase in the heating rate without a silicon carbide bed dilution increases both the activation temperature and the peak width. The curves obtained suggests that for lower heating rates, such as 1°C/min, the sample is given more time both to reach thermal equilibrium and to react. These two facts shift the peak towards lower temperatures and produce narrower peaks. On the other hand, higher heating rates prevent the reach of a thermal equilibrium in the sample, which cause the reaction to be carried out in a broader temperature range. The shift of the reaction towards higher temperatures, and the fast consumption of the reagent fed, moreover, lower the hydrogen concentration in the reactor, hindering the hydrogen diffusion and further slowing down the process.

The reduction will benefit more from the use of silicon carbide as diluting agent when combined with intermediate heating rate (i.e. $\beta \leq 5$°C/min), as the peak will be narrower and shifted towards lower temperatures. As stated in §3.1.4, these effects could be attributed to its high thermal conductivity and the capability of preventing the bed agglomeration. Differently, at higher heating rates its presence seems irrelevant, if not even detrimental: probably the mass used was not enough to grant a visible effect.

The quantifications suggest that a higher degree of reduction is achieved with 2.5°C/min without bed dilution, and with 5°C if coupled with a silicon carbide bed dilution: intermediate heating rates should then be preferred if a more complete reduction of the bed is desired.

3.1.6 Overall conclusions

Given the results obtained, it can be asserted that the parameters which most affect the shape of the TPR profile are the hydrogen inlet concentration and the heating rate.

Generally speaking, in the first part of the process the reduction is carried out on the surface of the particles and, since it happens at relatively low temperatures, it is under kinetic control: an

increase in the inlet hydrogen concentration both accelerates it and activates it at lower temperatures. As the process develops the bed shrinks and agglomerates, as proved by the fall of the pressure drop through the bed (see §3.3). A shell of copper is then produced, through which the gas must diffuse to react with the cupric oxide present in the core. This resistance is overcome by feeding a more concentrated mixture, as the main driving force for diffusion is the concentration gradient, and in this case the peak is shifted towards lower temperatures. On the other hand, when a less concentrated mixture is fed or when the heating rate is too high, the reagent diffusion through the sample is so slow that the peak appears at higher temperatures. The external mass transfer resistance is overcome by raising the fluid velocity.

A bed dilution with silicon carbide is proven to influence the TPR profile obtained, as visible changes are produced in the profile varying both the inlet concentration of hydrogen and the heating rate. This suggests that the action of silicon carbide could be dual, as it could help both to decrease the agglomeration, making thus the diffusion of the reducing mixture easier, and to level out temperature gradients along the bed.

The parameters choice of the reference case provided the achievement of a good degree of reduction in the system studied, and slightly higher results are provided when using a higher volumetric flowrate (+2.4% with 100 Ncm^3/min), a higher hydrogen concentration coupled with a bed dilution (+1.7% with a 10% H_2 mixture) or a higher heating rate coupled with a bed dilution (+2.2% with 5°C/min).

Taking into account the K parameter, defined as in Equation 1.19 and calculated for every test, the results obtained show that whenever K is lower, narrower peaks are produced. Broader peaks are instead produced whenever K is quite higher than the upper limit suggested by the authors [5] (i.e. 140 s for $6<\beta<18$°C/min), or also with quite low K values coupled with high heating rates. These observations suggest that a parameter choice that makes K lie in proximity of the ranges suggested favours the obtainment of narrow peaks, and so in a faster reduction, at least in the system just studied.

From the results obtained, high heating rates are not recommended, since they favour an inhomogeneous temperature distribution in the sample that will lead to an inaccurate analysis. Moreover low volumetric flowrates should be avoided a priori, as the peak shape would be affected more by dispersion effects linked to the slower gas velocity.

3.2 Temperature programmed oxidations (TPO)

After each sample reduction whose results have been reported in §3.1, an oxidation is subsequently carried out without extracting the sample from the reactor.

The global reaction considered is the oxidation of Cu to CuO [15]:

$$Cu_{(s)} + \frac{1}{2} O_{2\,(g)} \rightarrow CuO_{(s)}\,,\ \Delta H_R^0 = -156.06\ \frac{KJ}{mol\ Cu} \tag{3.4}$$

The experimental parameters varied are shown in Table 3.2. The results will be presented evidencing:

1. the oxygen flowrate fed ($\dot{n}_{O2}^{in}$), as it defines the maximum oxygen consumption achievable in the test;
2. the activation temperature (T_{act}), defined as the temperature at which the oxygen consumption becomes positive;
3. the temperatures of the maximum oxygen consumption ($T_{peak,1}$ and $T_{peak,2}$);
4. the temperature at which the oxidation ends (T_{fin});
5. the total oxygen regained by the sample ($n_{O,CuO}^{reg}$)
6. the degree of oxidation ($\%_{O,CuO}^{reg}$).

The reference case, obtained by analysing a 50-mg sample under 50 Ncm^3/min of mixture at 5% oxygen concentration, using a particle size <45 μm and a heating rate of 2.5°C/min, will be always shown with an orange curve in the plots.

***Table 3.8**: TPO experimental parameters variation.*

Parameter	Symbol	Unit of measure	Values	SiC dilution
Sample mass	m_s	[mg]	10, **50**	No
Particle size width	d_p	[μm]	**<45**, 100-150, 200-250	No
Total mixture volumetric flowrate	$\dot{V}_{tot}$	[Ncm^3/min]	25, **50**, 100	No
Oxygen volumetric percentage	y_O	[%]	1, **5**, 10	No
Heating rate	β	[°C/min]	1, **2.5**, 5, 10	No
Oxygen volumetric percentage	y_O	[%]	1, 5, 10	Yes
Heating rate	β	[°C/min]	2.5, 5, 10	Yes

As for the TPR, the effect of the oxygen concentration and the heating rate have been studied also diluting the bed with silicon carbide. The motivations are the ones already discussed in §3.1.

3.2.1 Sample mass effect (m_s)

The effect of the sample mass on the TPO profile is shown in Figure 3.6 and Table 3.9. The TPO profile of the reference case is also reported to compare the results in terms of oxidation degree when using the same sample mass.

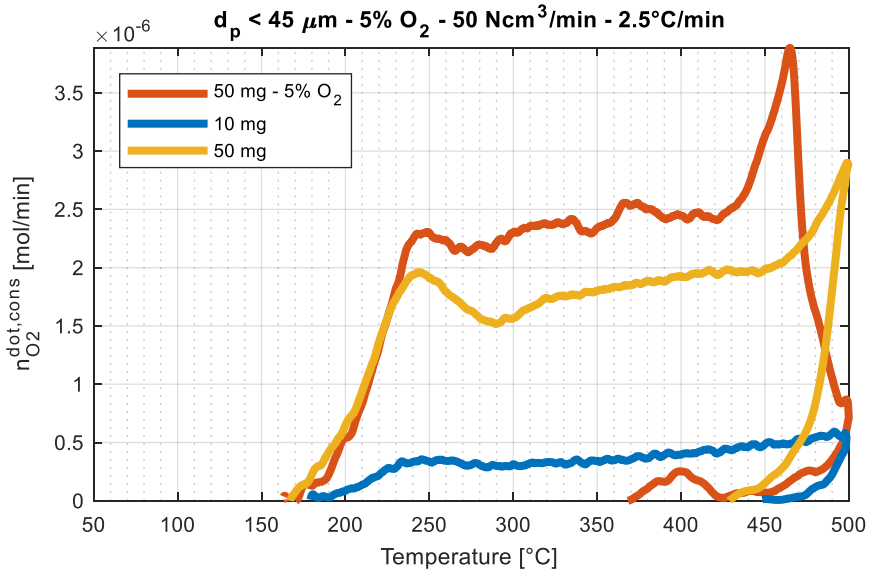

***Figure 3.6**: Sample mass influence on TPO profiles*

***Table 3.9:** Relevant data concerning the sample mass variation.*

m_s [mg]	y_{O2} [%]	$\dot{n}_{O2}^{in}$ [mol/min]	T_{act} [°C]	$T_{peak,1}$ [°C]	$T_{peak,2}$ [°C]	T_{fin} [°C]	$n_{O,CuO}^{reg}$ [mol]	$\%_{O,CuO}^{reg}$ [%]
10	1	$2.08 \cdot 10^{-5}$	178	244	500	452	$1.07 \cdot 10^{-4}$	84.4
50	1	$2.08 \cdot 10^{-5}$	167	244	500	430	$4.80 \cdot 10^{-4}$	75.6
50	5	$1.04 \cdot 10^{-4}$	163	244	465	371	$5.46 \cdot 10^{-4}$	86.1

Looking at the data above, two peaks are produced in all cases, but when using a greater sample mass an inflection at T=454°C (i.e. an abrupt change of the oxygen rate of consumption) is more evident, meaning that the process has accelerated. As explained in §1.6, the appearance of two distinct peaks could be associated with the copper oxidation being carried out in two steps, which are (Equation (3.5))

$$\begin{aligned} &(1)\quad 2Cu + 0.5\,O_2 \rightarrow Cu_2O \\ &(2)\quad Cu_2O + 0.5\,O_2 \rightarrow 2CuO \end{aligned} \tag{3.5}$$

Since the second peak is observed at the maximum temperature explored, and the oxidation continues also in the cooling process, it is clear that the second peak has not fully developed at

500°C. To fully develop the oxidation profile, the process should be carried out exploring a wider temperature range (e.g. from 50°C to 600°C) as Rodriguez *et al.* [12] did.
As the quantifications points out for the two cases oxidised with a 1% O_2 mixture, an increase in the sample mass decreases (-8.8%) the degree of oxidation of the sample. This result suggests that the complete oxidation is hindered if high sample masses are used, probably because a higher diffusional resistance develops in the process. The establishment of this resistance could be proved by the higher oxidation degree (+10.5%) obtained when feeding a more concentrated mixture (i.e. 5% O_2, see the orange curve of Figure 3.6) and using the same mass (i.e. 50 mg).

3.2.2 Particle size effect (d_p)

The effect of the fresh powder particle size on the TPO profile is shown in Figure 3.7 and Table 3.10.

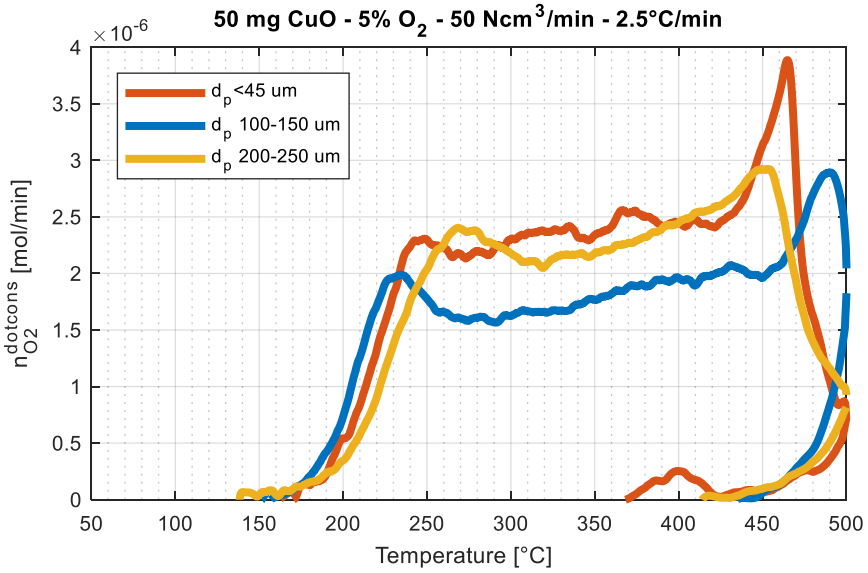

***Figure 3.7**: Particle size influence on TPO profiles.*

***Table 3.10**: Relevant data concerning the particle size variation.*

d_p [µm]	$\dot{n}_{O2}^{in}$ [mol/min]	T_{act} [°C]	$T_{peak,1}$ [°C]	$T_{peak,2}$ [°C]	T_{fin} [°C]	$n_{O,CuO}^{reg}$ [mol]	$\%_{O,CuO}^{reg}$ [%]
<45	$1.04 \cdot 10^{-4}$	163	244	465	371	$5.46 \cdot 10^{-4}$	86.1
100-150	$1.04 \cdot 10^{-4}$	153	231	490	433	$4.84 \cdot 10^{-4}$	76.3
200-250	$1.04 \cdot 10^{-4}$	139	270	452	420	$4.99 \cdot 10^{-4}$	78.6

As can be seen by the data above, two peaks in the oxidation process are obtained. Differently from the results in §3.2.1 the second peak is fully developed before the beginning of the cooling

ramp. Based on the results shown in §3.3 and §4.2, temperatures cannot be directly connected to the particle size because the bed has agglomerated during the previous TPR run.
The use of CuO powders of intermediate particle diameter range (i.e. 100-150 µm) decreaes the oxygen consumed between the two peaks (from T=250°C to T=450°C) compared to the other classes. In this particular case the oxygen consumption between the two peaks is lower than in the others. If the reaction exothermicity is advocated, it could be inferred that the smaller heat release due to the lower oxygen consumption makes the reaction slower, and so the second peak appears at a later time (i.e. at higher temperatures).
The quantifications show that a greater efficiency in oxidation is achieved when working with smaller particle sizes from the beginning of the previous TPR (+7.5~9.8%). Moreover, since the trend of the $\%_{O,CuO}^{cons}$ follows the one obtained in reductions (see Table 3.4), this suggests that the incomplete reduction of the bed could be caused by the effectiveness of the previous reductions.

3.2.3 Mixture volumetric flowrate effect ($\dot{V}_{tot}$)

The effect of the mixture volumetric flowrate on the TPO profile is shown in Figure 3.8 and Table 3.10Table 3.11.

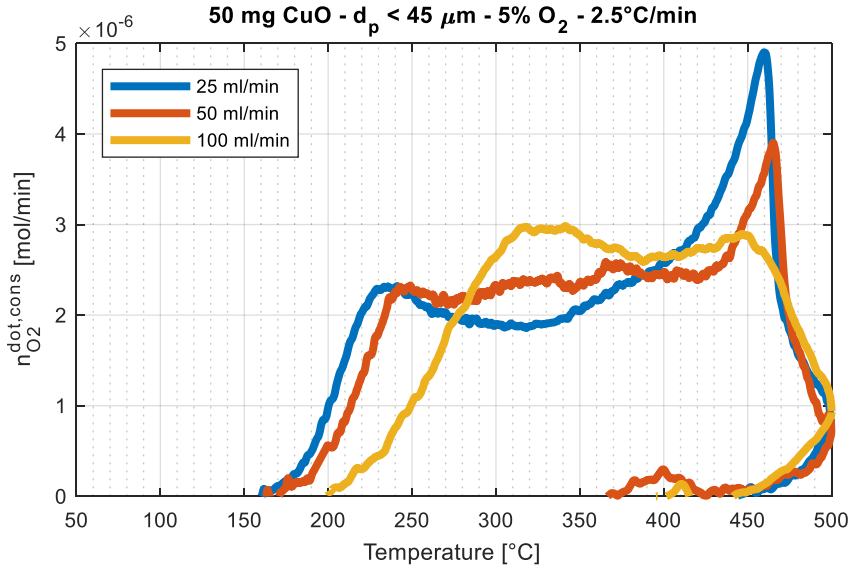

***Figure 3.8**: Mixture volumetric flowrate influence on TPO profiles.*

***Table 3.11**: Relevant data concerning the mixture volumetric flowrate variation.*

$\dot{V}_{tot}$ [Ncm^3/min]	$\dot{n}_{O2}^{in}$ [mol/min]	T_{act} [°C]	$T_{peak,1}$ [°C]	$T_{peak,2}$ [°C]	T_{fin} [°C]	$n_{O,CuO}^{reg}$ [mol]	$\%_{O,CuO}^{reg}$ [%]
25	$5.20 \cdot 10^{-5}$	161	235	461	404	$5.87 \cdot 10^{-4}$	92.5
50	$1.04 \cdot 10^{-4}$	163	244	465	371	$5.47 \cdot 10^{-4}$	86.1
100	$2.08 \cdot 10^{-4}$	201	327	448	448	$5.19 \cdot 10^{-4}$	81.8

As data above show, using lower volumetric flowrates (i.e. 25 Ncm^3/min or 50 Ncm^3/min) leads to the appearance of two peaks approximately at the same temperatures, even if the first one slightly reduces its height in the case of feeding 50 Ncm^3/min of mixture. Differently, a higher mixture volumetric flowrate (i.e. 100 Ncm^3/min) makes the oxidation process start at higher temperatures, (+83~92°C) and the resolution of the peaks is not pronounced. This leads to a higher oxygen consumption in between the two peaks.

Given these results, it can be said that an increase in the fluid velocity negatively affects the phenomena related to the first peak. Possibly a higher mixture velocity could have removed the reaction heat from the reactive bed, preventing the oxidation to develop in the first part (i.e. from T_{act} to $T_{peak,1}$).

The quantifications show a greater efficiency in oxidation when using smaller volumetric flowrates, while no correlation is found with the values obtained in the relative reduction process.

3.2.4 Inlet oxygen concentration effect (y_{O2})

The inlet oxygen concentration effect on the TPO profile, obtained with and without the bed dilution as explained in §3.1, is shown in Figure 3.9 and Table 3.12. The data for the oxidation with a 1% O_2 mixture coupled with the bed dilution are not available.

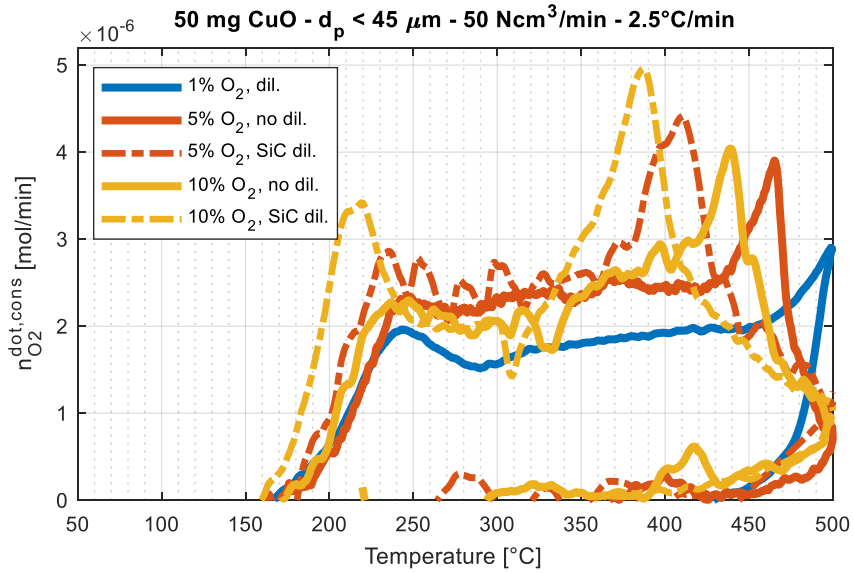

***Figure 3.9**: Inlet oxygen concentration influence on TPO profiles, with and without SiC dilution.*

***Table 3.12**: Relevant data concerning the inlet oxygen concentration variation.*

y_{O2}^{in} [%]	$\dot{n}_{O2}^{in}$ [mol/min]	T_{act} [°C]	$T_{peak,1}$ [°C]	$T_{peak,2}$ [°C]	T_{fin} [°C]	SiC dilution	$n_{O,CuO}^{reg}$ [mol]	$\%_{O,CuO}^{reg}$ [%]
1	$2.08 \cdot 10^{-5}$	167	235	500	431	-	$4.80 \cdot 10^{-4}$	75.6
5	$1.04 \cdot 10^{-4}$	168	244	465	371	-	$5.47 \cdot 10^{-4}$	86.1
10	$2.08 \cdot 10^{-4}$	175	245	439	303	-	$5.51 \cdot 10^{-4}$	86.9
5	$1.04 \cdot 10^{-4}$	180	236	411	264	Yes	$6.22 \cdot 10^{-4}$	98.1
10	$2.08 \cdot 10^{-4}$	110	215	388	369	Yes	$6.31 \cdot 10^{-4}$	99.5

As the data show, when a bed dilution is not used and the mixture concentration is varied, the activation temperatures are quite similar (171±4°C) and two peaks are always obtained. Likewise, the temperatures at which the first peak appears are similar (240±5°C), so a kinetic control is expected at lower temperatures, being the reaction not influenced by the feed concentration. On the other hand, when the oxygen concentration is increased, the second peak occurs at lower temperature. This could be caused by the establishment of diffusional limitation, which are overcome at higher temperatures and with a higher concentration gradient between the bulk and the outer surface of the sample. In the case of 1% O_2, the low oxygen concentration seems to be not sufficient to overcome the diffusional limitation, and the second peak (i.e. the second reduction step) is not fully developed.

Quantifications provide quite good results, suggesting that a greater efficiency is obtained when feeding a more concentrated mixture. The low oxidation degree with the less concentrated mixture could be related to the uncompleted development of the second peak, which leads to an incomplete oxidation of the sample.

A bed dilution with silicon carbide improves the results obtained: as Table 3.12 shows, indeed, it lowers the significantly $T_{peak,1}$ (-30°C) when feeding a more concentrated mixture (10% O_2). $T_{peak,2}$ is lowered as well in both cases (-54°C with 5% O_2, and -51°C with 10% O_2), and an almost-complete oxidation of the sample is reached. As will be shown in §4.4, the SiC bed dilution could have favoured the oxygen diffusion by delaying the agglomeration of the bed, and could also have levelled out temperature gradients, promoting a more uniform oxidation.

3.2.5 Heating rate effect (β)

The heating rate effect on the TPO profile, obtained with and without the bed dilution as explained in §3.1, is shown in Figure 3.10 and Table 3.13.

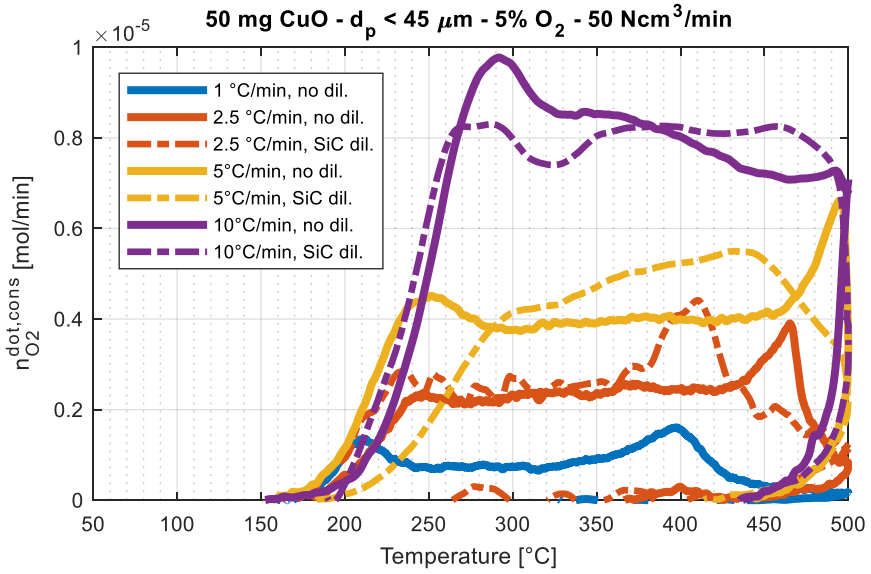

***Figure 3.10**:Heating rate influence on TPO profiles, with and without SiC dilution.*

***Table 3.13**: Relevant data concerning the heating rate variation.*

β [°C/min]	$\dot{n}_{O2}^{in}$ [mol/min]	T_{act} [°C]	$T_{peak,1}$ [°C]	$T_{peak,2}$ [°C]	T_{fin} [°C]	$n_{O,CuO}^{reg}$ [mol]	$\%_{O,CuO}^{reg}$ [%]
1	$1.04 \cdot 10^{-4}$	161	211	399	443	$4.94 \cdot 10^{-4}$	77.9
2.5	$1.04 \cdot 10^{-4}$	168	244	465	371	$5.46 \cdot 10^{-4}$	86.1
5	$1.04 \cdot 10^{-4}$	152	251	496	449	$5.30 \cdot 10^{-4}$	83.6
10	$1.04 \cdot 10^{-4}$	156	292	494	439	$5.32 \cdot 10^{-4}$	83.8
2.5	$1.04 \cdot 10^{-4}$	180	236	411	264	$6.23 \cdot 10^{-4}$	98.1
5	$1.04 \cdot 10^{-4}$	187	300	435	415	$4.85 \cdot 10^{-4}$	76.4
10	$1.04 \cdot 10^{-4}$	196	276	458	437	$4.99 \cdot 10^{-4}$	78.6

Looking at the data above regarding the non-diluted bed, two visible peaks are produced with low heating rates (β≤5°C/min). The shift of the first peak towards higher temperatures as the parameter β is increased suggests that the diffusion of the oxygen through the copper oxide formed becomes soon the dominant resistance.
When a greater heating rate (10°C/min) is used, the second peak is not obtained in the temperature range analysed: in this case the mixture could not have time to diffuse inwards due to the high heating rate used, while in parallel this fast temperature rise caused a decrease in the gas concentration, further hindering the process. The fact of not reaching the second peak seem also to suggest that an uneven temperature distribution is present in all the samples to be oxidised, being greater as β increases.
Quantifications values are average and seem to follow the trend given in Table 3.7 for the relative reduction, suggesting that an intermediate heating rate (2.5°C/min) provides better results both in reduction and in oxidation.
A bed dilution with silicon carbide shifts the activation temperatures towards higher values and strongly deforms the peaks shape, almost merging the two peaks in the case of using high heating rates (β≥5°C/min). This seems to suggest that the oxidation of Cu_2O to CuO (see Equation (3.5)) is promoted by the SiC bed dilution, probably due to its capability of levelling out temperature gradients in the bed generated by the reaction exothermicity and the high heating rates. Moreover, as pointed out in §3.2.4, it could have also favoured the oxygen diffusion in the inner part of the bed, as it delayed the agglomeration of the sample.
As well as in the case without bed dilution, using higher heating rates (β≥5°C/min) seems to hinder the complete oxidation of the bed. On the other hand, the highest degree of oxidation is reached using a bed dilution and intermediate heating rates (β=2.5°C/min), which suggest that this particular combination of parameters favours a complete oxidation of the bed.

3.2.6 Overall conclusions

Given the results obtained, the parameters which have a greater influence on the TPO profile are the inlet concentration of oxygen and the heating rate. Double peaks are obtained in most of the cases studied, while in some conditions (e.g. with 100 Ncm^3/min total volumetric flowrate and with 10°C/min and 5°C/min combined with a bed dilution) they are almost indistinguishable.
Referring to the results of Rodriguez *et al.* [12] and their analyses reported in Figure 1.10, the two peaks could be related to the two reaction steps that occur in the oxidation of copper, being the first one related to the Cu_2O production and the second to the CuO production.
Based on the results of Figure 1.10, it could be argued that when two peaks are formed both reactions starts at lower temperatures (around 200°C), but the first one finishes (at ca. 400°C) while the second one is carried out until all the Cu_2O is converted. The second reaction is slow

at the beginning because low quantities of cuprous oxide are present, while it reaches a maximum at around 450°C because a greater quantity of that oxide is present at that temperature. The peak merging suggests that a shift of the second reaction towards lower temperatures occurs, making the Cu_2O react faster to form CuO.
Since it was proven that the activation temperature and the temperature of the first peak are not influenced by a change in composition of the mixture fed, it can be guessed that the reaction is under kinetic control at lower temperatures. On the other hand, the shift of the first peak at higher heating rates suggests that in the first part of the oxidation process also diffusional limitations influence the outcome.
Since feeding a more concentrated mixture shifts the second peak towards lower values, it could be guessed that the main resistance in the later part of the oxidation process is diffusional. This is reasonable, since the reaction is first carried out on the surface of the solid and low diffusional limitations are present. As the reaction advances, however, the oxygen must diffuse inwards before reacting, making the diffusion the main limitation. This resistance becomes greater as the reaction progresses due to a simultaneous agglomeration and gradual increase of the oxide layer, making the oxidation of inner layers more difficult. This unfavourable condition is overcome by raising the oxygen concentration gradient between the solid bulk and the reaction interface, thus using a more concentrated feed.
The bed dilution with silicon carbide improves the results at different inlet oxygen concentrations, while promotes the Cu_2O oxidation to CuO when higher heating rates are used. Since in both cases the second peak temperatures are decreased with respect to those without dilution, it can be guessed that its action is dual also in TPO: SiC dilution decreases the contact between reacting particles, making the diffusion process easier by decreasing agglomeration effects, and levels out temperature gradients in the sample.

3.3 Pressure drop and thermal effects

Both in TPR and TPO analyses, pressure drop data have been registered for each run. The results were then plotted against temperature and overlapped to the hydrogen consumption rate for every test carried out. As Figure 3.11.a shows, during a TPR run the pressure drop fall just before the peak, meaning that from that moment onwards the bed agglomerates. In every test performed and presented in this chapter, pressure drop showed the same behaviour.
Moreover, a slight but appreciable decrease in pressure drop has been registered during the following TPO in the presence of the peaks (Figure 3.11.b), probably meaning that a further agglomeration of the bed occurred also during the oxidation process.

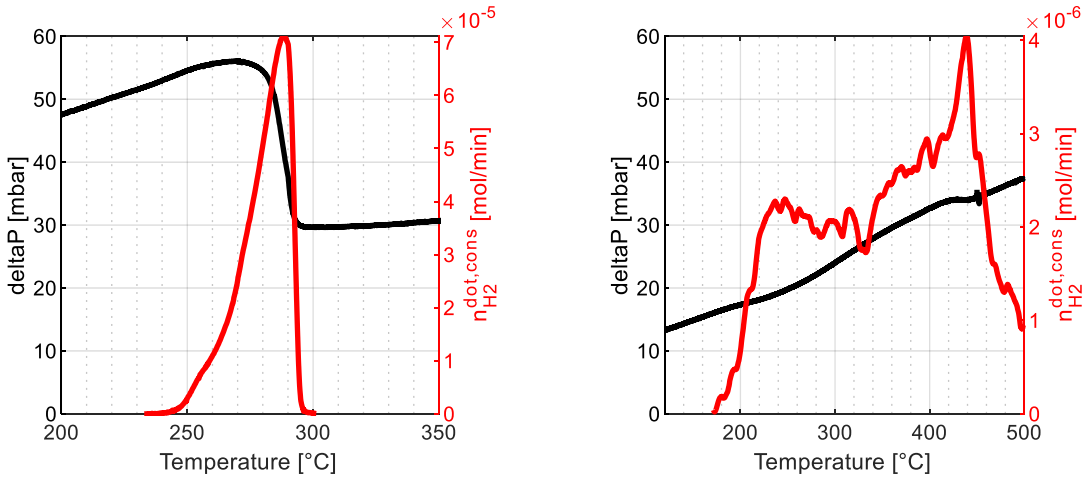

***Figure 3.11**: Measured pressure drop through the bed during* (a) *TPR with 10% H_2 and* (b) *TPO with 10% O_2, both without SiC dilution.*

Axial temperature gradients are detected in all the reactions carried out. This result is obtained by subtracting the temperature of the monitoring thermocouple with the controlling one (see Figure 2.1 for their arrangement in the reactor), and the resulting profile, overlapped to the reagent consumption curve, is shown in Figure 3.12. Since the profiles show the same behaviour, both during reduction (Figure 3.12.a) and oxidation (Figure 3.12.b), it is likely that a thermal effect deriving precisely from the reactions exothermicity could play a significant role in the progress of the reactions analysed, accelerating them and influencing the reaction peak shape.

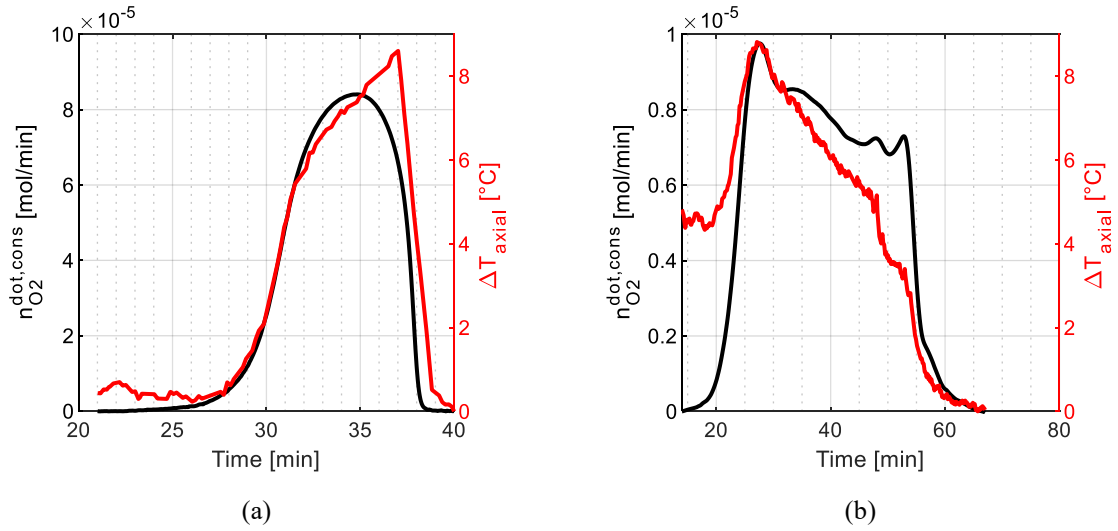

***Figure 3.12**: Axial difference in temperature for* (a) *TPR and* (b) *TPO, both carried out with β=10°C/min and without bed dilution.*

Furthermore, the silicon carbide capability of levelling out temperature gradients, more likely to happen when reactions are carried out at high heating rates, can be demonstrated by comparing the axial temperature gradient with (Figure 3.12) and without (Figure 3.13) the bed dilution using β=10°C/min. The comparison is immediate for the TPR case, since the baseline is straight for both the thermal profiles of Figure 3.12.a and Figure 3.13.a: using a SiC bed dilution, in this case, reduces the thermal axial gradient by 50%. In the case of the TPO run the effect is milder, as the maximum thermal gradients that develops with the SiC dilution is only 25% lower than the one without dilution. Thus, the addition of a highly conductive and inert material such as silicon carbide to dilute the bed is proven to positively affect the temperature distribution along the bed by reducing its axial and radial component.

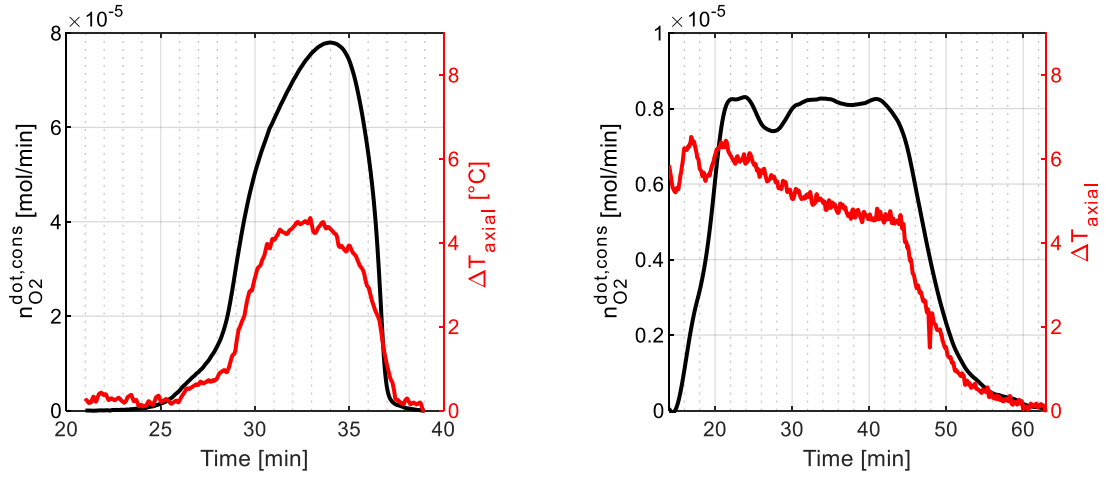

***Figure 3.13**: Axial difference in temperature for* (a) *TPR and* (b) *TPO, both carried out with β=10°C/min and a SiC bed dilution.*

3.4 Oxidised sample appearance

Interestingly, the agglomeration effects described in the aforementioned paragraphs and shown in multiple plots (Figure 3.11) are clearly visible on the bed conformation. Fresh and used (exposed to inert and oxidative pre-treatment, TPR and TPO) samples are shown in Figure 3.14.a and Figure 3.14.b, accordingly. As expected, different processes transformed a non-diluted bed in powder form into a compact lump with an axial shrinkage of 1 mm together with a lateral one (Figure 3.14.c).

(a) (b) (c)

***Figure 3.14**: (a) A 50 mg-sample before pretreatment; (b) the same sample after the TPO analysis and (c) highlight of the lateral shrinkage.*

In the case of bed dilution with silicon carbide, a powder bed of 3 mm was produced (Figure 3.15.a). These samples showed agglomeration but negligible axial shrinkage. On the other hand, some lateral wrinkles appeared (Figure 3.15.b).

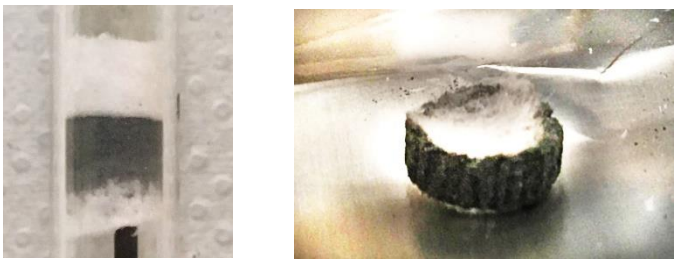

(a) (b)

***Figure 3.15**: (a) A 50 mg-sample diluted with silicon carbide before pretreatment; (b) the same sample after the TPO analysis.*

These wrinkles show that preferential passages between the bed and the reactor walls have established, which suggests that the gas preferentially took those paths during the test, partially by-passing the innermost part of the bed. As result, these parts could have been reached by the reactive mixture mainly through diffusion, which explains the importance of diffusive processes both reduction and oxidations.

Chapter 4

Cyclic redox reactivity

This chapter contains the results of further tests made to assess the cyclic redox reactivity of the cupric oxide under different experimental conditions. In detail, these studies involved:

1) The cupric oxide reactivity under eleven redox cycles;
2) The effect of additional thermal cycles under a flow of inert;
3) The influence of a different pre-treatment on the TPR and TPO profiles;
4) The effect of a bed height minimization;
5) The effect of a bed dilution with silicon carbide;
6) The axial temperature profile of a larger cupric oxide bed, both diluted and pure.

Apart from the tests 1) and 4), all the other investigations were performed using a larger quantity of sample, since a significant amount of it was required to be analysed after the test, both chemically and visually. The images produced are here presented to complete the analysis.

4.1 Sequential reductions and oxidation cycles

The activity of a copper oxide sample under sequential reduction and oxidation cycles has been analysed by performing 11 cycles of TPR-TPO in series. The setup used for the thermal treatments is the one reported in §2, with the only exception that the differential pressure transmitter was not used in this test. The sample features are reported in Table 4.1, while the parameters of the thermal cycles are reported in Table 4.2. The experimental procedure outlined in section §2.5 has been followed. The combination of mixture volumetric flowrate, reagent concentration and sample mass were chosen so to have a parameter K equal to 367.5 s (see Equation (1.21)), which proved to be effective in obtaining a single peak, as shown by the results of §3.1.

Table 4.1: *Cupric oxide bed features.*

Parameter	Symbol	Unit of measure	Values
Main reagent species	-	-	CuO
Sample purity	-	[%]	98
Sample mass	m_s	[mg]	51
Sample molecular weight	MW_s	[g/mol]	79.54
Sample molar amount	n_s	[mol]	$6.35 \cdot 10^{-4}$
Sample particle size range	d_p	[μm]	250-300
Particle bed height	H_{bed}	[mm]	2
Particle bed volume	V_{bed}	[cm^3]	0.071

Table 4.2: *Cycles parameters.*

	Inert [-]	Reagent [-]	$\dot{V}_{tot}$ [Ncm^3/min]	y_R [%]	$\dot{n}_R^{in}$ [mol/min]	β [°C/min]	T_{fin} [°C]	t_s [min]
Inert thermal cycle	Ar	-	50	-	-	5	200	30
Oxidant thermal cycle	Ar	O_2	50	5	$1.04 \cdot 10^{-4}$	5	250	60
TPR	Ar	H_2	50	5	$1.04 \cdot 10^{-4}$	2.5	500	0
TPO	Ar	O_2	50	5	$1.04 \cdot 10^{-4}$	2.5	500	0

4.1.1 TPR profiles

The results of the eleven reduction cycles are shown in Figure 4.1 and Table 4.3.

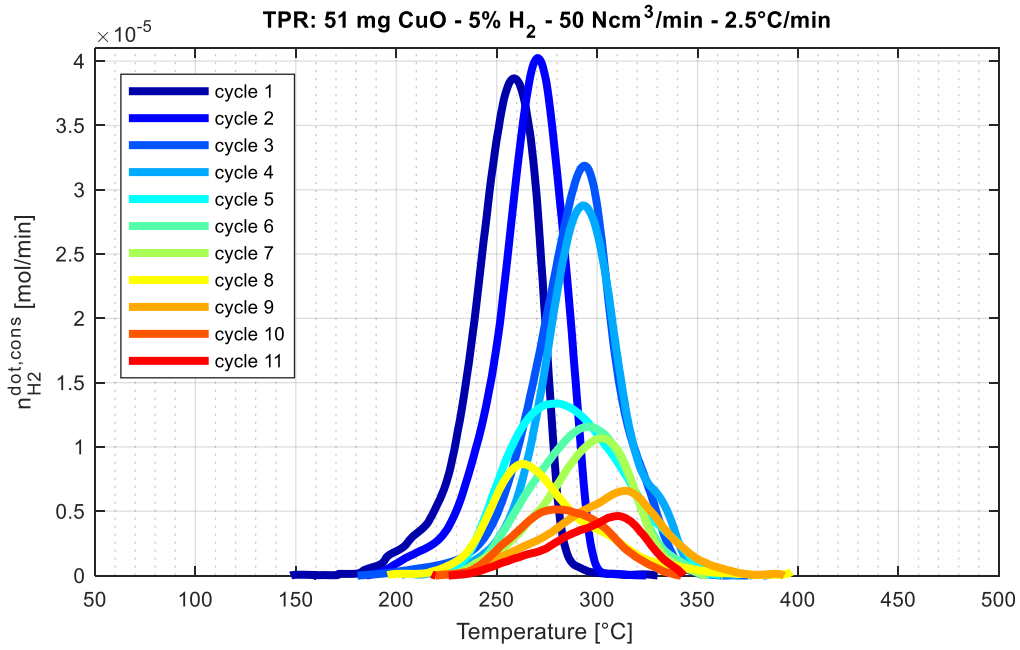

Figure 4.1: *TPR profiles obtained by the 11 sequential reduction and oxidation cycles.*

***Table 4.3**: Relevant data concerning the TPR profiles of sequential reduction and oxidation cycles.*

Cycle number	T_{act} [°C]	T_{peak} [°C]	T_{shift} [°C]	Peak width [°C]	Shoulder [-]	T_s [°C]	$n_{O,CuO}^{cons}$ [mol]	$\%_{O,CuO}^{cons}$ [%]
1	181	260	-	111	-	-	$6.10 \cdot 10^{-4}$	96.0
2	186	271	+11	106	-	-	$6.19 \cdot 10^{-4}$	97.5
3	190	295	+24	149	-	-	$6.06 \cdot 10^{-4}$	95.4
4	210	295	0	153	✔	330	$5.43 \cdot 10^{-4}$	85.6
5	200	280	-15	130	-	-	$3.74 \cdot 10^{-4}$	58.9
6	222	299	+19	119	-	-	$2.73 \cdot 10^{-4}$	43.0
7	226	305	+6	119	-	-	$2.29 \cdot 10^{-4}$	36.1
8	211	263	-42	161	✔	300	$1.98 \cdot 10^{-4}$	31.2
9	223	315	+52	154	-	-	$1.72 \cdot 10^{-4}$	27.0
10	217	282	-33	112	-	-	$1.21 \cdot 10^{-4}$	19.1
11	225	312	+30	112	-	-	$1.01 \cdot 10^{-4}$	16.0

As the data collected show, the activity of the cupric oxide sample decreases with the number of cycles, as the degree of reduction (i.e. $\%_{O,CuO}^{cons}$) gradually lowers. The only exception to the trend is the second cycle, for which the calculated hydrogen consumption increases with respect to the preceding TPR. This slight deviation from the trend could be caused by experimental errors, or by some phenomena happening in the preceding cycles that could change the catalyst structure, allowing a better reduction of the bed.

In the first two cycles the catalyst performances are good, since the reaction activates at low temperatures and almost all the bed is reduced (i.e. the reduction degree is close to 100%) fast (i.e. the peak width is narrower). As the cycles are performed, instead, the reactivity gradually worsens, since higher activation temperatures and a higher peak width are observed, coupled with a progressively decreasing bed reduction.

A drastic decrease in reactivity is observed from cycle 5 onwards: this reflects on the calculated reduction efficiency (-26.7% with respect to cycle 4) and in the peak shape, whose maximum hydrogen consumption visibly lowers. The profiles of the following cycles show an evident asymmetry, with progressively longer tails at low temperature, which suggests a resistance in the first part of the reaction, probably of diffusional type. This trend is inverted in cycle 8, while cycle 10 retains a symmetrical profile. Moreover, from cycle 9 onwards, double peaks seem to develop. All these observations suggest that a different reaction mechanism should be investigated in these cycles, involving not only the direct cupric oxide reduction, but also its partial reduction to cuprous oxide and diffusional limitations.

A shoulder is detected both in cycle 4 and 8, which from the studies of Lee *et al*. [11], as already mentioned in §3.1.3, could be considered a clue for the trapped hydrogen release.

Since every TPR has been followed by a TPO, the correct explanation for these behaviours could be deduced by looking at the oxygen consumption profiles during the oxidation cycles.

4.1.2 TPO profiles obtained with the oxygen sensor

The results of the eleven oxidation cycles are shown in Figure 4.2 and Table 4.4.

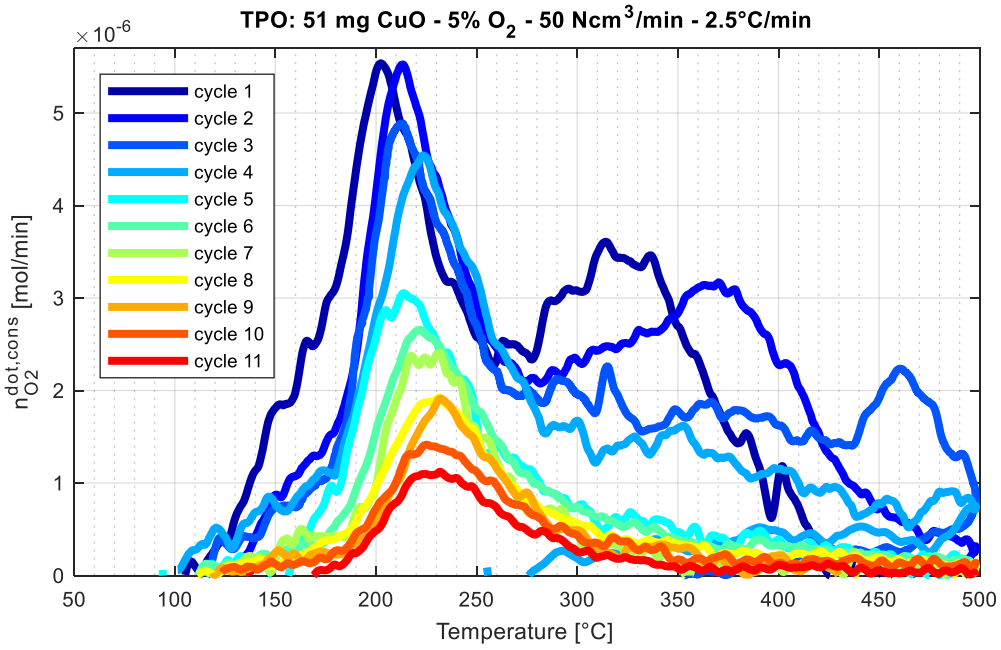

***Figure 4.2**: TPO profiles of the 11 sequential reduction and oxidation cycles obtained with the oxygen sensor.*

***Table 4.4**: Relevant data concerning the TPO profiles of sequential reduction and oxidation cycles.*

Cycle number	T_{act} [°C]	$T_{peak,1}$ [°C]	T_{shift} [°C]	2nd peak	$T_{peak,2}$ [°C]	$n_{O,CuO}^{reg}$ [mol]	$\%_{O,CuO}^{reg}$ [%]
1	105	201	-	✔	318	$6.24 \cdot 10^{-4}$	98.2
2	131	215	+14	✔	366	$6.37 \cdot 10^{-4}$	100.4
3	116	211	-4	✔	457	$5.96 \cdot 10^{-4}$	93.8
4	102	223	+12	-	-	$5.08 \cdot 10^{-4}$	80.0
5	115	217	+6	-	-	$3.14 \cdot 10^{-4}$	49.5
6	123	221	+4	-	-	$2.25 \cdot 10^{-4}$	35.4
7	126	224	+3	-	-	$1.69 \cdot 10^{-4}$	26.7
8	120	226	+2	-	-	$1.59 \cdot 10^{-4}$	25.1
9	130	233	+7	-	-	$1.25 \cdot 10^{-4}$	19.7
10	124	227	-6	-	-	$1.19 \cdot 10^{-4}$	18.7
11	137	229	+2	-	-	$0.92 \cdot 10^{-4}$	14.5

The data presented above evidence the presence of the first peak in all the cycles performed, which always lies between a temperature ($T_{peak,1}$) of 200°C and 230°C. On the other hand, the second peak shows only in the first three cycles, and its temperature ($T_{peak,2}$) shifts towards higher values as the cycle number increases. As the cycles are performed, moreover, the degree of oxidation (i.e. the integral of the peak) decreases: this lowers the value of $\%_{O,CuO}^{cons}$ calculated evidencing the decrease of the sample reactivity.

To explain the phenomena happening as the peaks form, the oxidation mechanism of cupric oxide should be advocated: based on the studies of Zheng *et al.* [18], the first step involves the creation of a cupric oxide shell on the surface of the reacting solid. This explanation is confirmed by the results of Rodriguez *et al.* [12] who evidenced the presence of small amounts of cupric oxide since the beginning of the reaction. Subsequently, the contemporary migration of copper ions to the inner shell interface and the diffusion of oxygen ions towards the interface allows the partial oxidation of the core to cuprous oxide. Finally, the complete oxidation to cupric oxide follows. As two peaks appear in the first three oxidation cycles, it can be concluded that they are related to the two reactive steps of the mechanism (i.e. the $2Cu + 0.5\ O_2 \rightarrow Cu_2O$ reaction and the $Cu_2O + 0.5\ O_2 \rightarrow 2CuO$ reaction respectively).

The explanation of the whole process consisting of the eleven TPR-TPO cycles could be formulated by looking at the efficiency of the redox cycles, which is represented graphically in Figure 4.3. During the first reduction, not all the cupric oxide initially present in the sample is reduced to copper, since its reduction degree is lower than 100%: in this case some copper or a small quantity of its oxides are expected to be still present in the sample. During the following TPO, all the sample is expected to be re-oxidised to its original state, since its degree of oxidation surpasses even the preceding TPR degree of reduction. This behaviour is repeated in the second cycle. The slightly higher degree of oxidation obtained in these cases could be associated to experimental errors, or to the production of small quantities of copper peroxide (CuO_2), whose presence, however, could not be verified.

In the third cycle the trend reverts: during the TPR the sample is not reduced completely, as the cycle degree of reduction is still lower than 100% (i.e. 95.4%), and in the following TPO the sample is not oxidised completely either, because the cycle degree of oxidation (i.e. 93.8%) is lower than the reduction degree just mentioned. As in the preceding cycles, some Cu_2O is expected to form instead of CuO during the TPR, and some additional Cu_2O is expected to form in the following TPO. This trend composed of the incomplete bed reduction followed by an incomplete bed oxidation seems to repeat over the cycles, except for the TPR of cycle 7, 8 and 9, for which the degree of reduction is higher than the preceding TPO degree of oxidation. Also in this case some errors in the quantification may have occurred, or simply some of the cuprous oxide present in the bed could have reduced again to copper, thus consuming more hydrogen than what could be predicted by the preceding TPO degree of oxidation.

Since a substantial decrease in the TPR performances is observed in cycle 5 (-21.6% with respect to the preceding TPO) while the TPO degree of oxidation in cycle 4, 5 and 6 does not decrease significantly with respect to the preceding degree of reduction, it is suggested that the drastic decrease in the efficiencies from cycle 5 onwards lies in some phenomena happened during the fifth TPR. Therefore, if this test involving cyclical TPR and TPO will be repeated in future, a sample characterization before and after the decrease in efficiency are suggested.

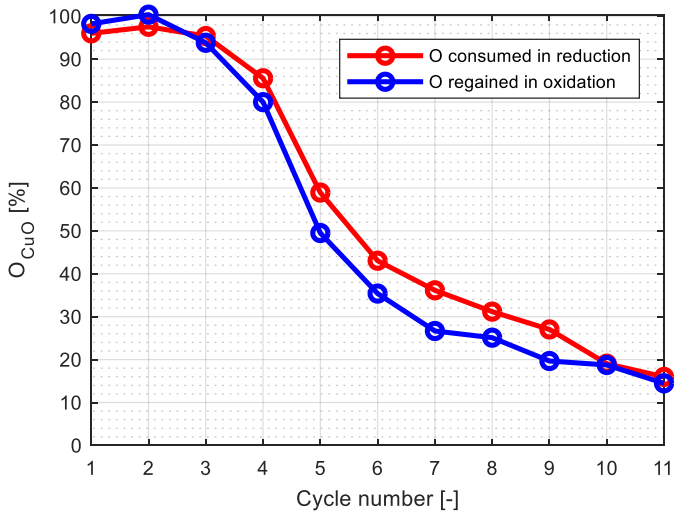

***Figure 4.3**: Graphical representation of the cycles efficiencies.*

4.1.3 TPO profiles obtained with the mass spectrometer

Following the procedure outlined in §2.5, the composition of the outlet mixture during oxidations has been analysed also using the mass spectrometer to cross-check the final results with the quantifications values and the oxidation profiles obtained through the oxygen sensor. The profiles obtained by the signal processing are shown in Figure 4.4 and Table 4.5. The first TPO data are not available.

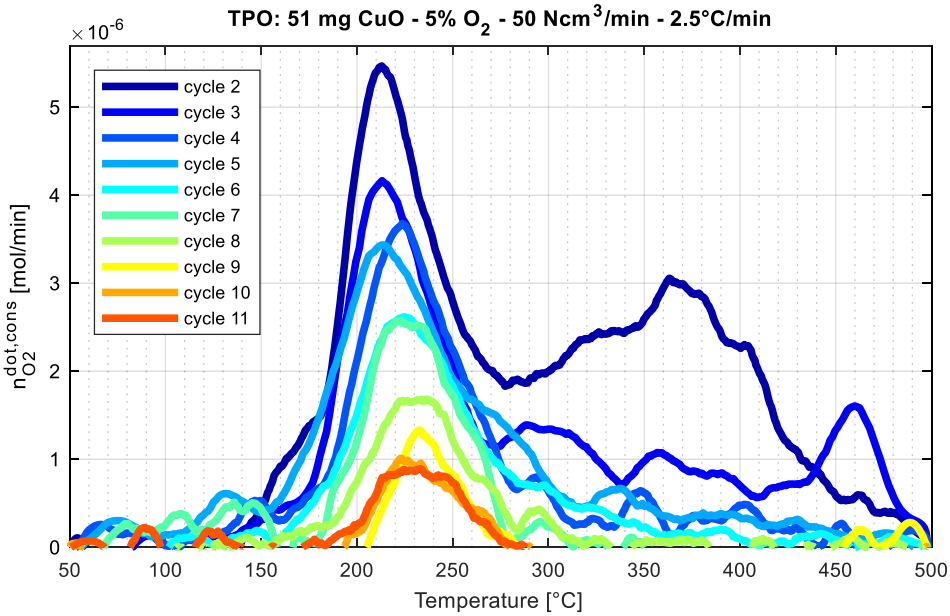

***Figure 4.4**: TPO profiles of the 11 sequential reduction and oxidation cycles obtained with the mass spectrometer.*

***Table 4.5**: Relevant data concerning the TPO profiles of sequential reduction and oxidation cycles.*

Cycle number	$T_{peak,1}$ [°C]	T_{shift} [°C]	2nd peak	$T_{peak,2}$ [°C]	$n^{reg}_{O,CuO}$ [mol]	$\%^{cons}_{O,CuO}$ [%]
2	212	-	✔	370	$5.78 \cdot 10^{-4}$	91.1
3	214	+2	✔	461	$4.76 \cdot 10^{-4}$	74.9
4	223	+9	-	-	$1.98 \cdot 10^{-4}$	31.2
5	213	-10	-	-	$2.32 \cdot 10^{-4}$	36.6
6	226	+13	-	-	$1.86 \cdot 10^{-4}$	29.3
7	226	0	-	-	$0.65 \cdot 10^{-4}$	10.2
8	230	+4	-	-	$1.13 \cdot 10^{-4}$	17.8
9	232	+2	-	-	$0.83 \cdot 10^{-4}$	13.2
10	228	-4	-	-	$1.24 \cdot 10^{-4}$	19.6
11	231	+5	-	-	$1.20 \cdot 10^{-4}$	18.9

As the data above show, the oxygen consumption profiles obtained through the mass spectrometer are similar to the ones obtained using the oxygen sensor (Figure 4.2), but a higher noise is present. This is supposed to be the cause of the anomalous behaviour shown by the quantifications, which suggests that the sample oxidation performances are dramatically compromised from cycle 4 onwards (i.e. when $\%^{cons}_{O,CuO}$ reaches 31.2%, in parallel with the second peak disappearance). The presence of noise prevents also a precise estimation of the activation temperature, but still allows the correct identification of the peak temperatures and the disappearance of the second peak from cycle 4 onwards.

Given these facts, only data deriving from the oxygen sensor will be shown.

4.1.4 Sample characterization

Once the eleventh TPO cycle had finished, the sample has been extracted from the reactor and analysed. Its shrinkage was evident, being the final bed height of less than 1 mm, and all the particles merged and were covered by a layer of black copper oxide. Its appearance is shown in Figure 4.5.

Figure 4.5: *Spent CuO bed after 11 redox cycles.*

The oxidised sample has been observed also using a SEM (i.e. Scanning Electron Microscope), and the images provided by the instrument showed that most of its surface was plain and covered by short fibres, yet also granules and protuberances were found, as shown in Figure 4.6.a. This surface flattening, which is evidenced in Figure 4.6.b, was probably due to the agglomeration of particles combined with the high number of reactive loops. The breakage of a protuberance, whose inner part is shown in Figure 4.7.a, revealed that under its external layer, whose depth is of approximately 3 μm, an inner porous structure with pore diameter of 200~800 nm is present. Finding a similar structure under the external surface, which from Figure 4.7.b seems to be collapsed, suggests that the sample is surrounded by a shell under which a nano-porous structure lie.

Also an EDS (i.e. Energy Dispersive X-ray Spectrometry) analysis has been carried out, which revealed that under the surface of the sample mainly copper oxides were present, with a small quantity of impurities such as silicon dioxide and calcium oxide, probably belonging to the sample or to some quartz wool fibre residual. Furthermore, a percentage of 61.90% copper and of 32.35% atomic oxygen has been found (1.91:1 ratio), suggesting that the sample is composed mainly (around 90%) of cuprous oxide (Cu_2O), being the ratio between these two elements 2:1 in this oxide.

Unfortunately, nor the cycle number nor the process (i.e. TPR or TPO) in which this structure is acquired could be known from these analyses, but from the moment in which it is formed, the diffusional resistance induced by the shell should be considered as part of the reactive process.

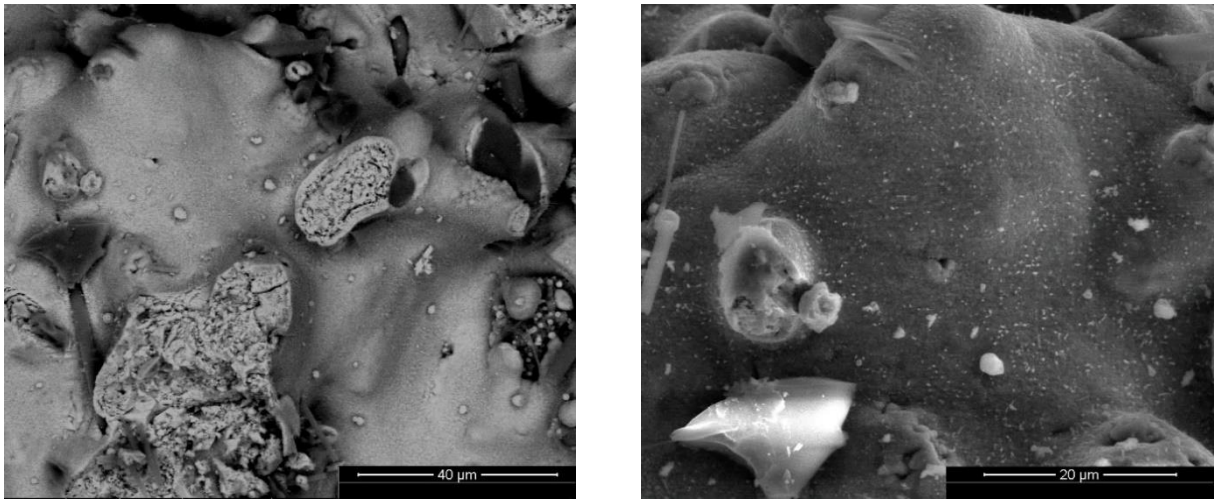

(a) (b)

***Figure 4.6**: (a) Back-scattered SEM image of the sample surface, (b) SEM image of the sample surface.*

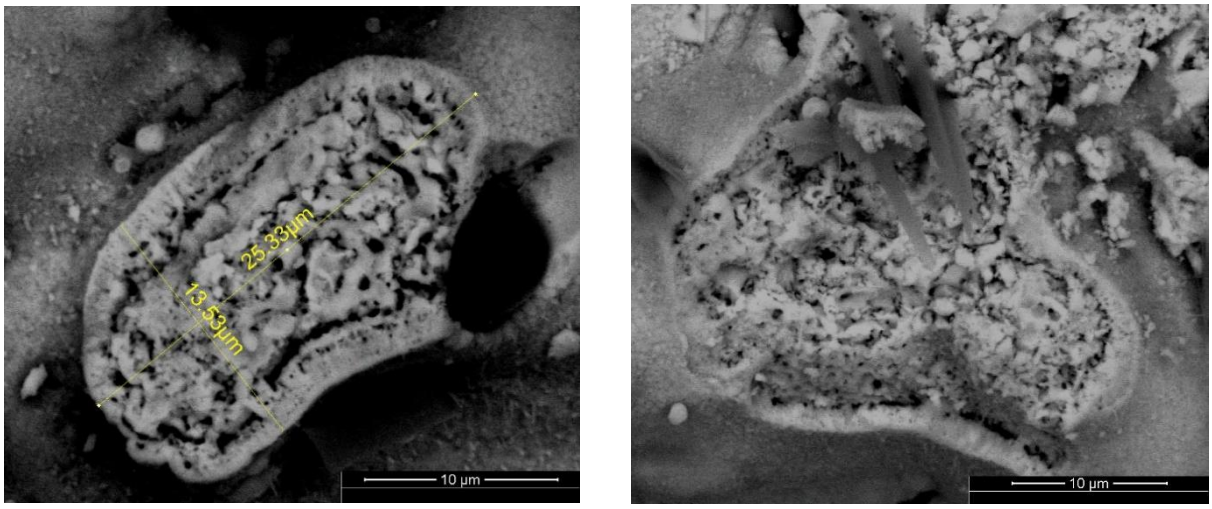

(a) (b)

***Figure 4.7**: (a) Enlargement of Fig. 4.5 and (b) focus on the structure under its surface.*

4.2 Pressure drop through the packed bed

4.2.1 K parameter calculations

Since further sample-destructive laboratory analyses on the oxidised sample had to be carried out to investigate on the particles agglomeration evidenced in §4.1.4, the mass used in the following tests has been increased. The criterion followed to decide the sample mass consisted in finding a trade-off between:

- the resulting height of the bed;
- the K parameter, which should be kept constant and equal to the one used in §4.1 (i.e. 367.5 s) in order to investigate on the effects given by a change in its parameters (i.e. m_s, $\dot{V}_{tot}$, y_r).

A program which calculates the K values as function of the mixture volumetric flowrate and its composition, parametric in the sample mass, has thus been made. The trade-off between the two conditions has been found in using a sample of 200 mg and performing the analyses with 100 Ncm^3/min of mixture at 10% reagent concentration. The surface representing the K value variation and the plane intersecting it at the desired value are shown in Figure 4.8.a and Figure 4.8.b respectively.

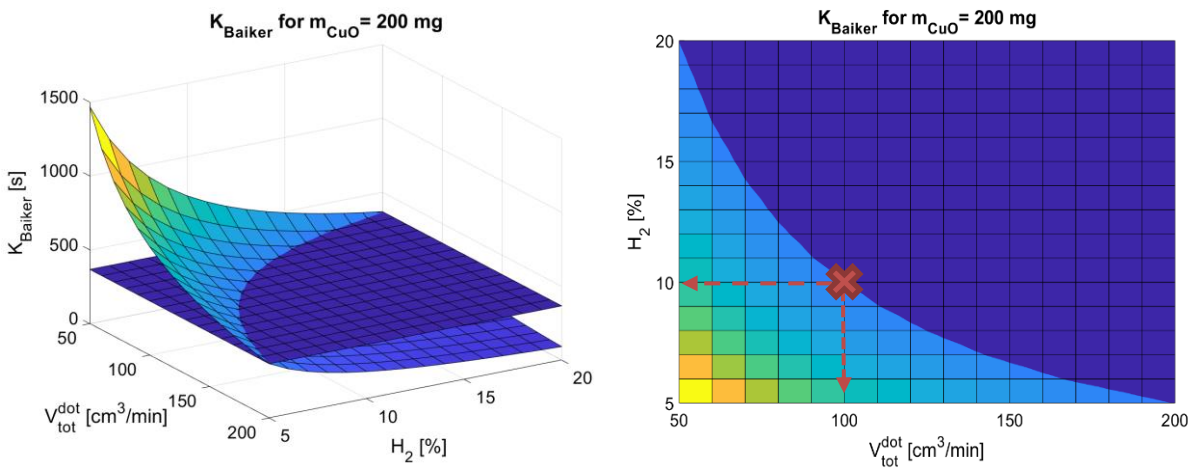

(a) (b)

Figure 4.8: (a) *K parameter calculations for a sample mass of 200 mg and* (b) *choice of the experimental parameters' combination.*

4.2.2 Intermediate cycles under inert flow

This test has been made with the purpose of verifying the effect of thermal cycles in an inert gas on the bed structure. The objective has been achieved by monitoring the pressure drop over the copper oxide bed both during the thermal cycles and at ambient temperature. This allowed to find the step responsible for the bed agglomeration.

Following the K parameter predictions of §4.2.1, the sample mass to be analysed has been increased with respect to the one used in §4.1 together with the mixture volumetric flowrate and its composition. The same setup shown in §2 is used, and the experimental procedure

outlined in §2.5 has been followed to perform the tests, while a different cupric oxide with respect to the one of §4.1 has been used. This test included a sample pre-treatment consisting in a thermal cycle under inert flow and a thermal cycle under oxidant mixture, followed by a redox cycle, 3 cycles under inert and one additional redox cycle. The cycles parameters are provided in Table 4.7.

Before running the test, the fresh oxide has been sieved to investigate its particle diameter distribution, and the results are reported in Figure 4.9. A particle size smaller than 45 µm has been chosen to maximize the specific surface area of the sample.

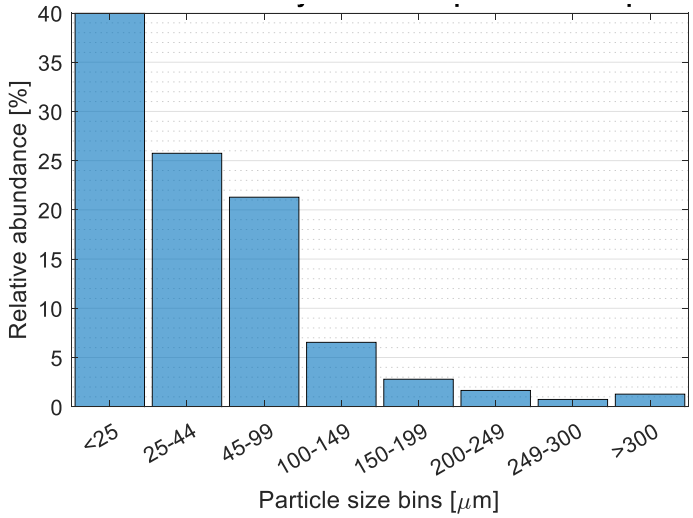

***Figure 4.9**: Particle size analysis of the CuO sample used.*

The resulting bed features are reported in Table 4.6, while the appearance of the bed is shown in Figure 4.10.a. While setting the reactor up, some of the particles adhered to the internal surface of the quartz tube, and have been trapped by the upper quartz wool bed while it was positioned. As a result, the quartz wool got dirty.

A focus on the particle shape and size, provided by the SEM, is shown in Figure 4.10.b. As the picture evidences, the particles used in this test are mostly flat with sharp protuberances on their edges, while at the same time also grain of smaller size and rounded edges are present. The high polydispersity of the sample suggests that the resulting bed packing will be high.

***Table 4.6**: Cupric oxide bed features.*

Parameter	Symbol	Unit of measure	Values
Main reagent species	-	-	CuO
Sample purity	-	[%]	99.995
Sample mass	m_s	[mg]	203
Sample molecular weight	MW_s	[g/mol]	79.54
Sample molar amount	n_s	[mol]	$2.54 \cdot 10^{-3}$
Sample particle size range	d_p	[μm]	<45
Particle bed height	H_{bed}	[mm]	6
Particle bed volume	V_{bed}	[cm^3]	0.284

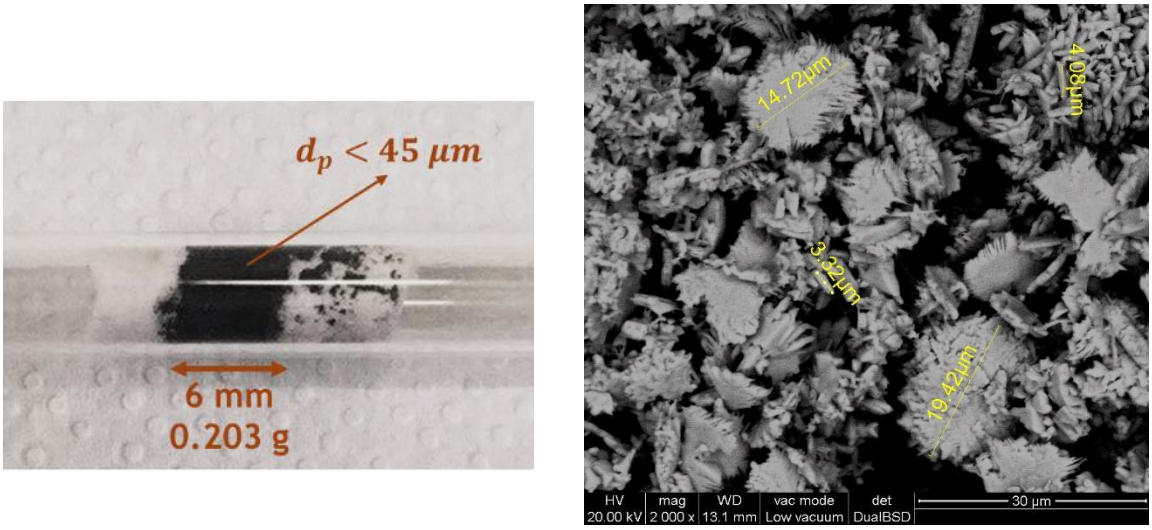

(a) (b)

Figure 4.10: (a) *Appearance of the reactive bed and* (b) *focus on the bed particle size and shape.*

***Table 4.7**: Cycles parameters.*

	Cycle [-]	Inert [-]	Reagent [-]	$\dot{V}_{tot}$ [Ncm^3/min]	y_R [%]	$\dot{n}_R^{in}$ [mol/min]	β [°C/min]	T_{fin} [°C]	t_s [min]
Inert thermal cycle	1	Ar	-	100	-	-	5	200	30
Oxidant thermal cycle	2	Ar	O_2	100	10	$4.16 \cdot 10^{-4}$	5	250	60
TPR	3	Ar	H_2	100	10	$4.16 \cdot 10^{-4}$	2.5	500	0
TPO	4	Ar	O_2	100	10	$4.16 \cdot 10^{-4}$	2.5	500	0
Inert cycle	5	Ar	-	100	-	-	2.5	500	0
Inert cycle	6	N_2	-	100	-	-	2.5	500	0
Inert cycle	7	Ar	-	100	-	-	2.5	500	0
TPR	8	Ar	H_2	100	10	$4.16 \cdot 10^{-4}$	2.5	500	0
TPO	9	Ar	O_2	100	10	$4.16 \cdot 10^{-4}$	2.5	500	0

4.2.2.1 Bed pressure drop and initial bed porosity calculations

Before beginning the test, the pressure drop variations of the line (i.e. of reactor, piping and quartz wool beds) have been measured under a flow of argon at ambient temperature while varying its volumetric flowrate. Once the reactive bed was placed into the reactor, the same measures have been taken using the same gas type and flowrates. The data obtained in both cases have been fitted using a quadratic function which allowed to retrieve the functions $\Delta P_{line}(\dot{V})$ in the first case, and $\Delta P_{system}(\dot{V})$ in the second one. The subtraction of these function allowed to find the pressure drop generated by the bed $\Delta P_{bed}(\dot{V})$, as in Equation (4.1)

$$\Delta P_{bed}(\dot{V}) = \Delta P_{system}(\dot{V}) - \Delta P_{line}(\dot{V}),\ T = 20°C \tag{4.1}$$

In order to estimate the porosity of the bed, moreover, the Ergun equation expressed in Equation (4.2) has been used

$$\frac{\Delta P_{bed}}{H_{bed}} = 150 \cdot \mu \cdot \frac{v}{d_p^2} \cdot \frac{(1-\varepsilon_{bed})^2}{\varepsilon_{bed}^3} + 1.75 \cdot \rho \cdot \frac{v^2}{d_p} \cdot \frac{1-\varepsilon_{bed}}{\varepsilon_{bed}^3}, \tag{4.2}$$

where H_{bed} is the height of the bed, ε_{bed} is the porosity of the bed, μ is the gas viscosity, v is the gas velocity, d_p is the particle diameter and ρ is the gas density [4]. This equation merges the Blake-Kozeny equation, which is seen in its first term and expresses the pressure drop variation when a laminar regime establishes in the particle bed, and the Burke-Plummer equation, which is seen in its second term and expresses the pressure drop variation when a turbulent regime establishes.

Equation (4.2) has been solved for ε by inserting the value of ΔP_{bed} found by flowing 100 Ncm^3/min of argon together with the values of μ, v and ρ of argon at ambient temperature [20], and the values of H_{bed} and d_p shown in Table 4.6. In this case, the calculations have been made approximating the particles as spherical and mono-dispersed with a diameter equal to 45 μm. The resulting bed porosity was ε_{bed} = 0.311, meaning that the bed packing was quite high.

The line pressure drop has been also measured from T=20°C to T=500°C with a heating rate of 2.5°C/min and with a constant flowrate of 100 Ncm^3/min of argon, and the quadratic fitting of the registered data allowed to retrieve the function $\Delta P_{line}(T)$. This has been done in order to calculate the bed pressure drop $\Delta P_{bed}(T)$ during the thermal cycles using Equation (4.3)

$$\Delta P_{bed}(T) = \Delta P_{system}(T) - \Delta P_{line}(T),\ \dot{V}_{tot} = 100\ Ncm^3/min \tag{4.3}$$

The bed pressure drop obtained by Equation (4.3) could deviate from the real ones, since the $\Delta P_{system}(T)$ of the reactive cycles have been obtained with different conditions with respect to the ones found when measuring $\Delta P_{line}(T)$ (i.e. a mixture of Ar/H_2 flowed when performing a TPR, and a mixture of Ar/O_2 flowed when performing a TPO), but since the reactive mixture was diluted, this deviation has been assumed negligible.

4.2.2.2 Thermal cycles results

Once the functions representing the line pressure drop $\Delta P_{line}(\dot{V})$ and $\Delta P_{line}(T)$ were fitted, the inert and the oxidant pre-treatments have been run in sequence and with the parameters reported in Table 4.7. The pressure drop over the bed during these thermal cycles showed a linear behaviour, and no anomalies (i.e. pressure drop falls) were detected. The procedure outlined in §4.2.2.1 to calculate the porosity of the bed has been repeated after every pre-treatment, which given a value of ε_{bed} =0.304 in both cases. It is then inferred that no evident agglomeration happens during the pre-treatments.

The results of the following TPR combined with the pressure drop variation in the bed as the analysis was performed are shown in Figure 4.11, while Table 4.8 highlights the relevant data retrieved by the plot together with the quantifications of the total hydrogen consumed in the reduction.

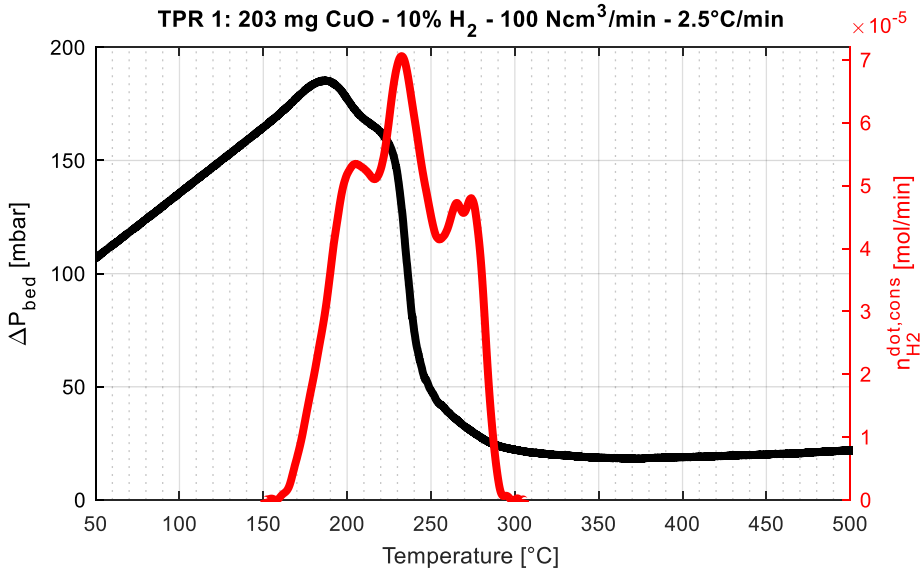

Figure 4.11: *Hydrogen consumption and pressure drop through the bed during the first TPR.*

Table 4.8*: Relevant data concerning the first TPR run.*

TPR number [-]	T_{act} [°C]	$T_{peak,1}$ [°C]	Secondary peak(s)	T_s [°C]	Peak range [°C]	$n_{O,CuO}^{cons}$ [mol]	$\%_{O,CuO}^{cons}$ [%]
1	158	233	✔	204, 266, 276	142	$2.21 \cdot 10^{-3}$	87.2

As the data gathered show, with the parameters m_s, $\dot{V}_{tot}$ and y_R chosen multiple peaks are observed in the hydrogen consumption profile. Moreover, the dramatic fall of the bed pressure drop (T=220°C) evidence that, during the reduction, the bed clearly agglomerated.
If the behaviour of $\Delta P_{bed}(T)$ is observed, it could be guessed that the catalyst bed starts agglomerating soon after the reaction begins (T=190°C), as a slight decrease in the pressure drop is detected. As the reaction is carried out the agglomeration continues, but when the pressure drop falls dramatically (T=220°C) a by-pass for the gas is created. Since the conditions for the application of Equation (4.2) are not met from this moment onward (i.e. the particles merged), the estimation of the porosity through the Ergun equation is not carried out.
As analysed in §1.5, the presence of multiple peaks could derive from the agglomeration that has been identified at T=220°C: this phenomena would indeed produce a layer through which the hydrogen should diffuse before reacting, adding a delay to the hydrogen consumption curve, which is observed at T=220°C.
One hypothesis to explain the secondary peak observed around T=270°C could be a sudden physical re-arranging of a small portion of the bed, where the gas passage was previously hindered. In this way some less reduced particles could become more exposed to the gaseous reagent, slightly increasing the rate of reaction.
On the other hand, also an inhomogeneous temperature distribution inside the sample, probably caused by the reaction exothermicity or by an uneven heating of the system, could be the cause of the multiple peaks. In this case a higher rate of reaction would be present in the hotter zones, leading to an increase in the hydrogen consumption, and so in a peak. In parallel, the colder zones would react later, producing delays in the peak, creating secondary peaks, as observed in this case.
The degree of reduction provided by the quantification (i.e. $\%_{O,CuO}^{cons}$) suggests that the bed has not reduced completely: as a consequence, some cuprous or cupric oxide are expected to be still present in the reduced sample.
The results of the following TPO are shown in Figure 4.12 and Table 4.9.

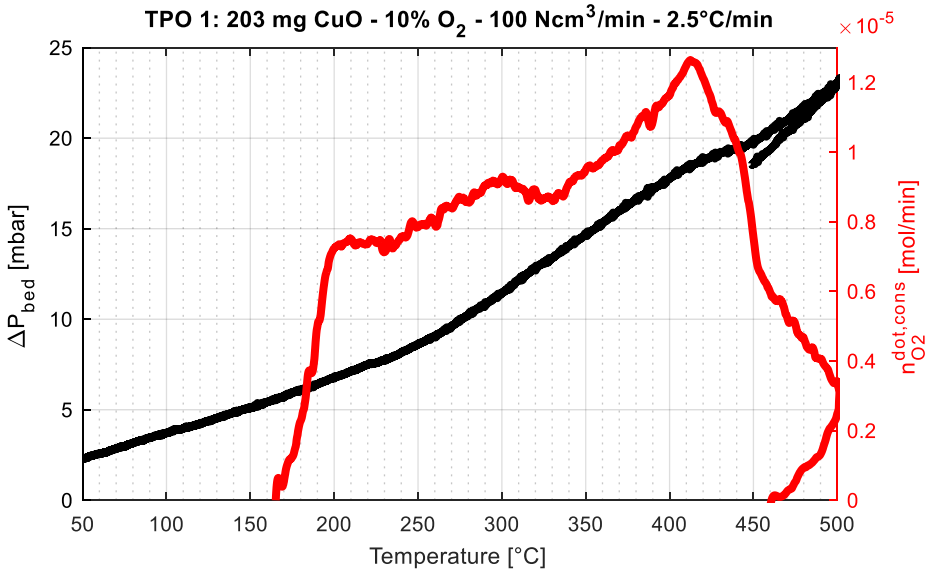

***Figure 4.12**: Oxygen consumption and pressure drop through the bed during the first TPO, obtained with the oxygen sensor.*

***Table 4.9:** Relevant data concerning the first TPO run.*

TPO number [-]	T_{act} [°C]	$T_{peak,1}$ [°C]	$T_{peak,2}$ [°C]	$n_{O,CuO}^{reg}$ [mol]	$\%_{O,CuO}^{reg}$ [%]
1	155	250	415	$2.22 \cdot 10^{-3}$	87.4

As Figure 4.12 shows, the pressure drop through the bed is very low, that suggests an irreversible packing of the bed during the previous TPR. Three peaks seem to be present in the oxygen consumption curve (i.e. a mechanism of reaction consisting of three steps is likely). If the profiles provided by the mass spectrometer are analysed, though, two peaks are identified, and their temperature are reported in Table 4.9. Probably the additional peak detected by the sensor could have been caused by an uneven oxidation of the bed.

As the shape of the profile evidences, the oxidation of the bed has been carried out also during the cooling process, and ended at T=460°C.

The degree of oxidation provided by the quantifications suggests that the bed has been oxidised completely, as its value is only slightly higher (+0.2%) than the previous TPR degree of reduction, probably due to experimental errors.

The following three thermal cycles have been carried out under an inert flow. The raw pressure drop registered by the transmitter are shown in Figure 4.13 instead of the $\Delta P_{bed}(T)$, as in the three cycles two different inert gases have been used. The fact of registering similar pressure drop during the first cycle and the third one, both carried out using argon as inert, suggests that they do not influence the macroscopic structure of the catalyst.

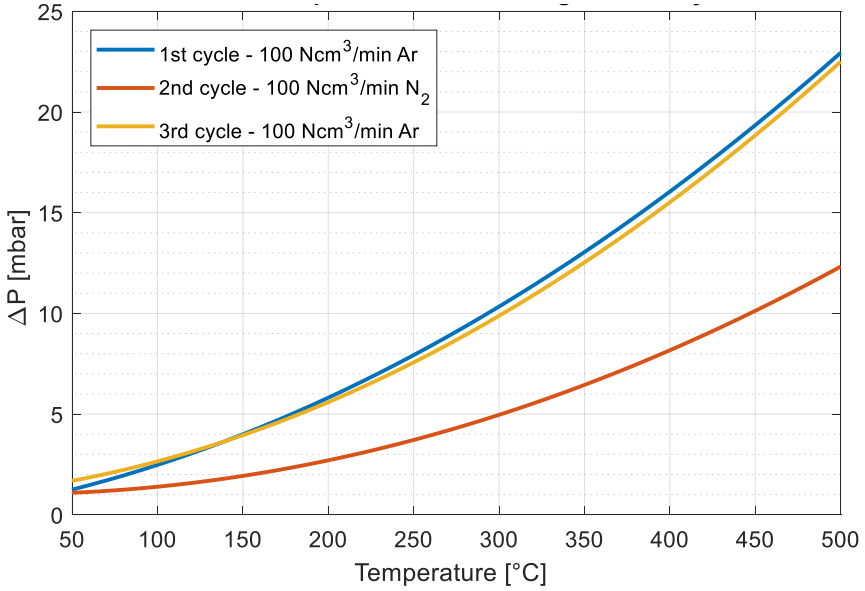

***Figure 4.13**: Pressure drop through the bed during the three inert thermal cycles.*

The following TPR results are presented in Figure 4.14 and in Table 4.10.

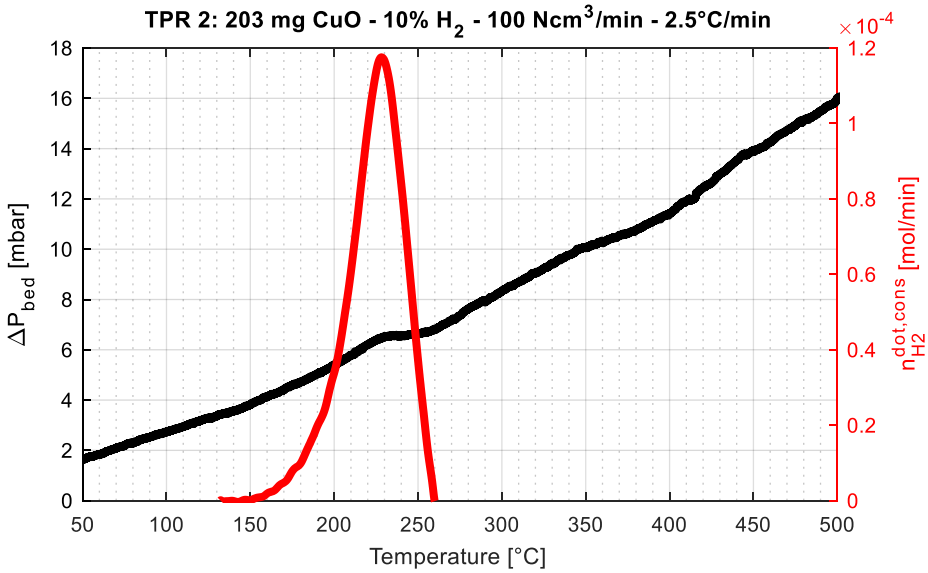

***Figure 4.14**: Hydrogen consumption and pressure drop through the bed during the second TPR.*

***Table 4.10:** Relevant data concerning the second TPR run.*

TPR number [-]	T_{act} [°C]	$T_{peak,1}$ [°C]	Secondary peak(s)	T_s [°C]	Peak range [°C]	$n_{O,CuO}^{cons}$ [mol]	$\%_{O,CuO}^{cons}$ [%]
2	146	228	-	-	124	$1.92 \cdot 10^{-3}$	75.6

Conversely to what observed in the first reduction cycle, one peak is obtained in the second cycle. In this case the reaction starts at lower temperatures because some structural defects could have appeared during the first cycle. As the studies of Rodriguez *et al.* [12] evidences, the formation of these more active sites decreases the reduction induction time (i.e. the reaction starts at lower temperatures). In parallel, the decrease of the surface area due to the previous agglomeration of the sample lowers the reaction rate when T<180°C. On the other hand, observing a single peak after the agglomeration suggests that when the conduction prevails over diffusion in the heat transfer mechanism, one peak is obtained. Moreover, since the secondary peak evidenced at T=270°C in the first TPR does not show in this cycle, probably a bed rearrangement did not happen.

The fact of having two inflections in $\Delta P_{bed}(T)$ seems to suggest that the bed had agglomerated further during the TPR, and that this process happened in the second part of the reduction.

The calculated degree of reduction is smaller than in the first TPR (-11.6%): also in this case, then, some copper oxides are expected to be present in the sample.

The results of the following TPO are shown in Figure 4.15 and in Table 4.11.

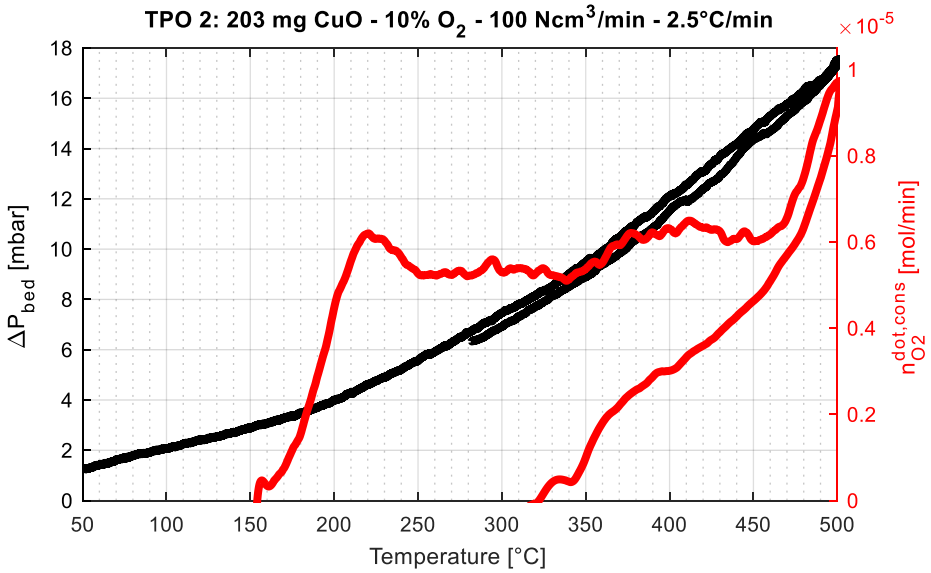

***Figure 4.15**: Oxygen consumption and pressure drop through the bed during the second TPO.*

***Table 4.11**: Relevant data concerning the second TPO run.*

TPO number [-]	T_{act} [°C]	$T_{peak,1}$ [°C]	$T_{peak,2}$ [°C]	$n_{O,CuO}^{reg}$ [mol]	$\%_{O,CuO}^{reg}$ [%]
2	155	220	500	$2.22 \cdot 10^{-3}$	72.3

Also for the second TPO a mechanism consisting of two reactive step occurs: the first peak is barely distinguishable with the profile obtained through the oxygen sensor, but its presence is

confirmed by the one obtained through the mass spectrometer. The second one, instead, is evident in the profiles obtained by both the instruments.

As observed in the second TPO of §4.1.2, the first peak is found nearly at the same temperatures as the first TPO run, while the second peak shows at higher temperatures, and the oxidation is carried out also during the cooling process. Since this gap between the peaks increases as the cycles are performed, and during every reduction a further agglomeration of the sample happens, it is suggested that a correlation between these two phenomena could hold.

The oxidation degree of the second TPO is slightly lower than the reduction degree of the previous TPR (-3.3%): as a result, some cupric oxide or copper are expected to be still present.

As every thermal cycle finished, different argon flowrate at ambient temperature have been flowed in the reactor, and the pressure drop has been registered. $\Delta P_{bed}(\dot{V})$ has been calculated using Equation (4.1), the points have been fitted using a quadratic function, and the results are shown in Figure 4.16.

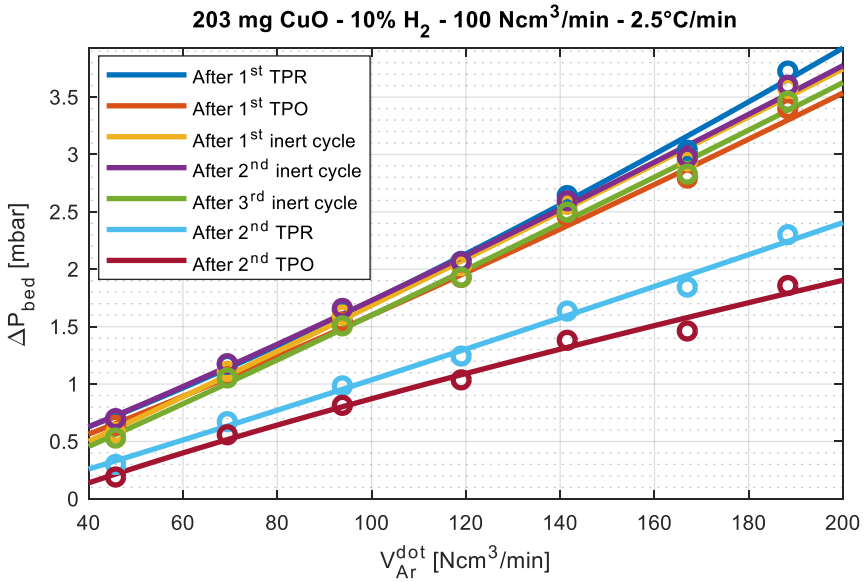

***Figure 4.16**: Pressure drop through the bed after each thermal cycle.*

Note that this plot does not show $\Delta P_{bed}(\dot{V})$ before the first TPR, since only a punctual value was available for the comparison (namely, $\Delta P_{bed}(100\ Ncm^3/\min Ar)$=93.3 mbar after the inert pre-treatment and $\Delta P_{bed}(100\ Ncm^3/\min Ar)$=92.8 mbar after the oxidant pre-treatment). Reminding these values, it is seen that the higher pressure drop fall between the cycles is found after the first TPR, for which at $\dot{V}_{Ar}$=100 Ncm^3/min the gap is of approximately 91 mbar: this supports the hypothesis made before, and so that the main agglomeration happens during the first TPR. Moreover, the plot evidences that a further agglomeration happened during the second TPR, since the $\Delta P_{bed}(\dot{V})$ are slightly lower than the ones registered after each inert cycle.

4.2.2.3 Visual inspection and sample characterization

After the tests were finished, the sample (Figure 4.17) appeared as a compact cylinder, and showed an axial shrinkage of 1 mm coupled with a lateral shrinkage. The analysis made throughout §4.2.2.2 suggests that this structure has been attained during the first TPR cycle.

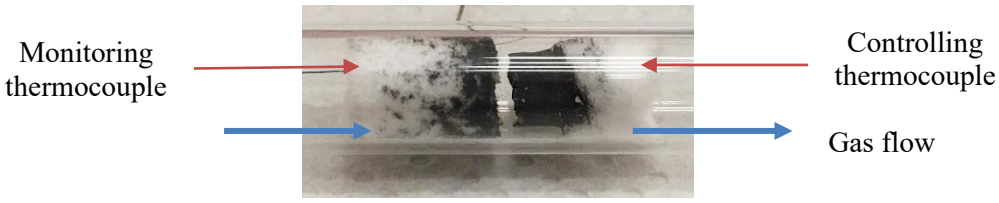

***Figure 4.17**: Sample appearance after the thermal cycles.*

The sample has been then analysed with the Scanning Electron Microscope, and its images are reported in Figure 4.18 and Figure 4.19.

Figure 4.18 shows a comparison between the fresh particles (Figure 4.18.a) and the external structure of the spent oxide (Figure 4.18.b): as it could be expected by the pressure drop behaviour in reduction, the particles have agglomerated and their edges have been rounded off. Moreover, some fibres are observed on the top of the surface, which could compensate for the surface area decrease given by the agglomeration process. Since some short fibres have been detected also in the oxidised sample of §4.1.4, as evidenced by Figure 4.6.a, it is suggested that they form during the first reactive cycles and then they are rounded off as the cycles are performed, thus reducing the rate of reaction at high cycles number.

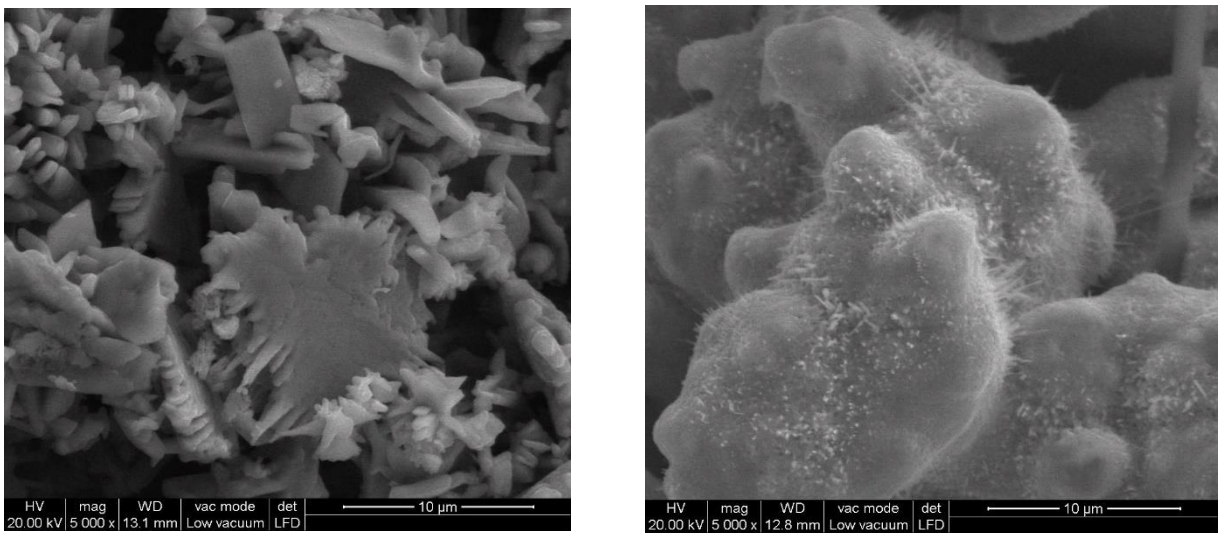

(a) (b)

***Figure 4.18**: SEM image focus of* (a) *the oxidised sample surface and* (b) *the fresh cupric oxide powder used in the sample.*

The breakage of the sample external layer (Figure 4.19.a and Figure 4.19.b), whose depth was about 1µm, revealed that the inner particles have reacted, since their edges are smoothed with respect to the fresh sample ones, and did not merge in the process. The difference between the shell depth of the oxidised sample of §4.1.4 (3 µm) and this one suggests that this layer grows cycle by cycle, increasing the diffusional resistance of the process.

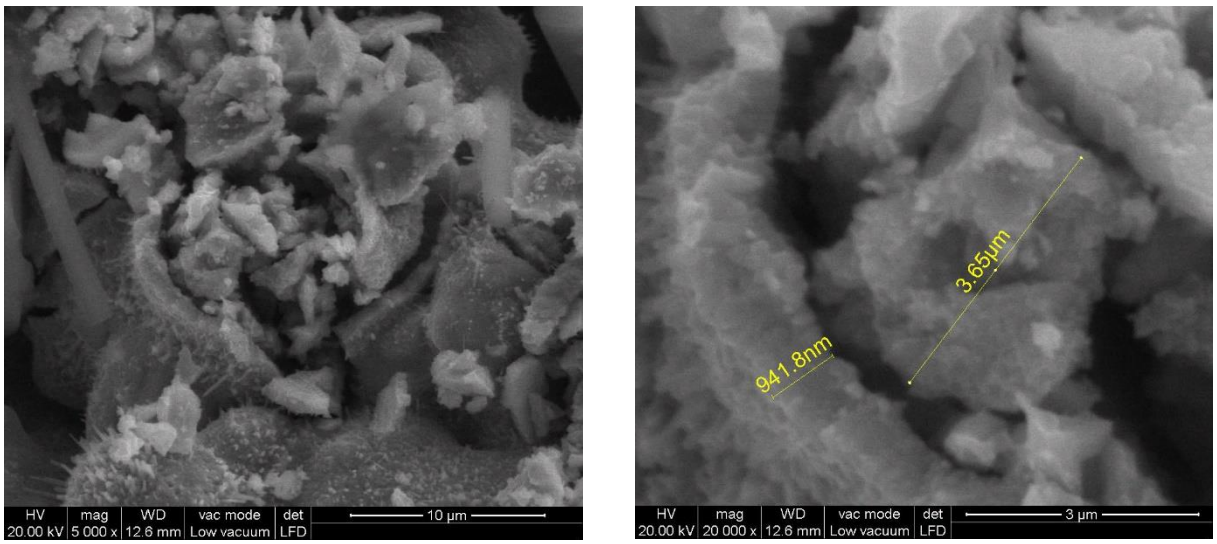

(a) (b)

Figure 4.19*: SEM image of* (a) *a breakage of the external shell and* (b) *the internal structure.*

4.2.3 Pre-treatment variation

This test has been made with the purpose of investigating the effect of a pre-treatment consisting only in a thermal cycle under inert flow both on the agglomeration phenomenon and on the peak shape.

The setup outlined in §2 and the same sample amount of §4.2.2 has been used to perform the tests, so the sample features and appearance remain the ones reported in Table 4.6 and in Figure 4.10 respectively.

This test included an inert pre-treatment of the sample followed by a TPR-TPO sequence, whose parameters are shown in Table 4.12.

Also in this case the $\Delta P_{line}(\dot{V})$ at ambient temperature and $\Delta P_{line}(T)$ using a 100 Ncm^3/min flowrate of argon were retrieved before placing the cupric oxide bed into the reactor. This was done in order to calculate the $\Delta P_{bed}(\dot{V})$ and the $\Delta P_{bed}(T)$ later on as explained in §4.2.2.1. Also the bed initial porosity has been calculated beforehand following the procedure outlined in §4.2.2.1, and the result obtained (ε_{bed}=0.296) suggest that the bed packing was higher than the bed used in §4.2.2.

***Table 4.12**: Experimental parameters used in the cycles.*

	Cycle [-]	Inert [-]	Reagent [-]	$\dot{V}_{tot}$ [Ncm^3/min]	y_R [%]	$\dot{n}_R^{in}$ [mol/min]	β [°C/min]	T_{fin} [°C]	t_s [min]
Inert thermal cycle	1	Ar	-	100	-	-	5	200	30
TPR	2	Ar	H_2	100	10	$4.16\cdot10^{-4}$	2.5	500	0
TPO	3	Ar	O_2	100	10	$4.16\cdot10^{-4}$	2.5	500	0

4.2.3.1 Redox cycles results

The first TPR results are reported in Figure 4.20 and Table 4.13.

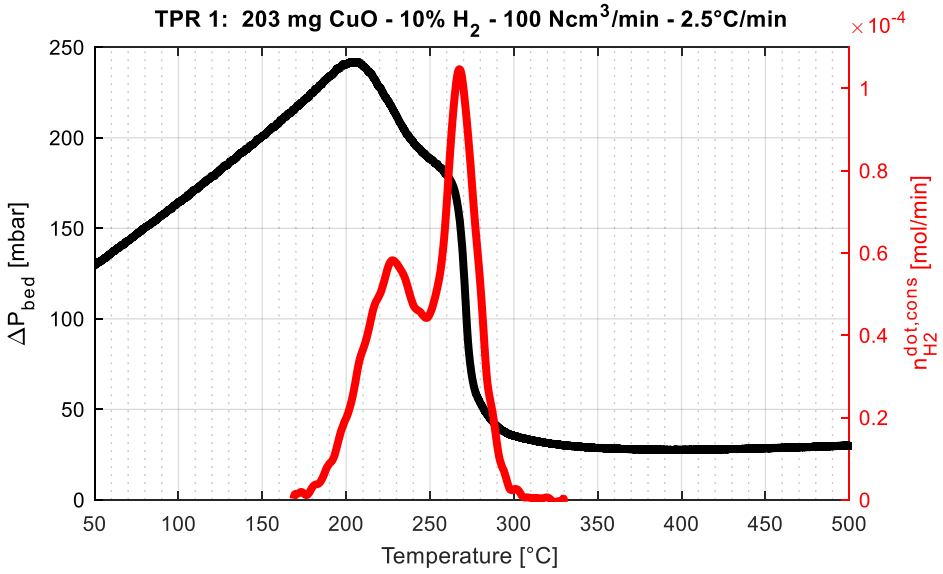

***Figure 4.20**: Hydrogen consumption and pressure drop through the bed during the first TPR.*

***Table 4.13**: Relevant data concerning the first TPR run.*

TPR number [-]	T_{act} [°C]	$T_{peak,1}$ [°C]	Secondary peak(s)	T_s [°C]	Peak range [°C]	$n_{O,CuO}^{cons}$ [mol]	$\%_{O,CuO}^{cons}$ [%]
1	175	268	✔	228	125	$2.08\cdot10^{-3}$	81.9

As for the first TPR of §4.2.2.2, also in this case the bed has agglomerated, as the fall of the $\Delta P_{bed}(T)$ curve suggests: this fact confirms that the reduction process is responsible of the agglomeration. Differently, the hydrogen consumption profile of this one shows two peaks instead of four: this suggests that the formation of the last two peaks in the previous experiment

(see Figure 4.11) could be given by the different pre-treatment or by random phenomena happening with the rearrangement of the bed. Moreover,

The double-peak shape could be explained using the same phenomena already mentioned in §4.2.2.2 for the first TPR: as the reaction develops, the bed agglomerates and a shell over the unreacted particles form. A delay is then added to the peak (i.e. a second peak forms) because the reagent should diffuse through it before reacting. On the other hand, as in the previous test, temperature gradients inside the bed could have formed, favouring an increase in the hydrogen rate of consumption in the hotter zones and a delay in its consumption (i.e. a shift of the peak towards higher temperatures) because of the slower reaction in colder zones.

The degree of reduction is unexpectedly low if compared to the previous TPR (-5.3% with respect to the first TPR of §4.2.2.2) which was run in similar conditions: this could have been caused by experimental errors, as in this particular experiment the TCD signal was quite noisy, or by the absence of the oxidant pre-treatment. However, this last hypothesis seems weak, as the high sample purity should have allowed to start with an almost completely oxidised sample even without the oxidant pre-treatment.

It is interest to notice that, in this particular case, the axial temperature gradient obtained as in §3.3 (i.e. by subtracting the monitored temperature and the controlling temperature) followed quite well the hydrogen consumption profile, as shown in Figure 4.21. Since thermal peaks rise later in time with respect to the hydrogen consumption ones, it is likely that the temperature rise in the sample is caused by the reaction exothermicity, rather than it being the cause of the double-peak profile in the hydrogen consumption curve.

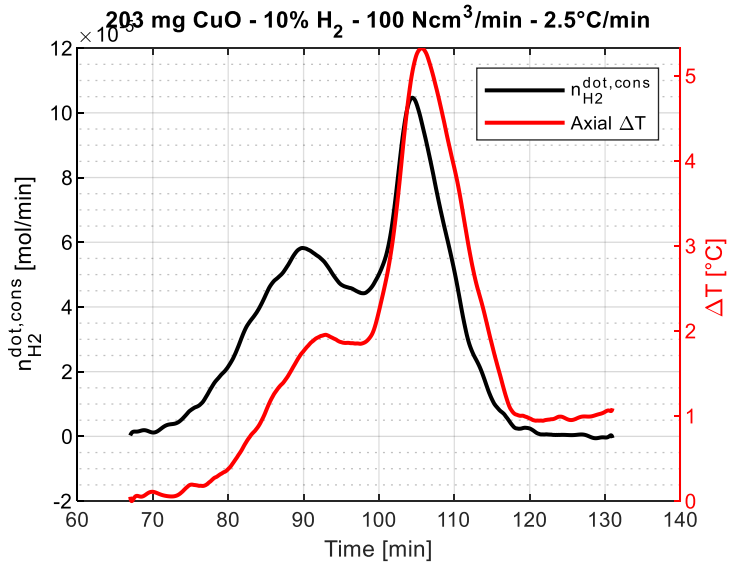

Figure 4.21: *Hydrogen consumption profile and axial difference in temperature for the first TPR run.*

The following TPO results are shown in Figure 4.22 and Table 4.14.

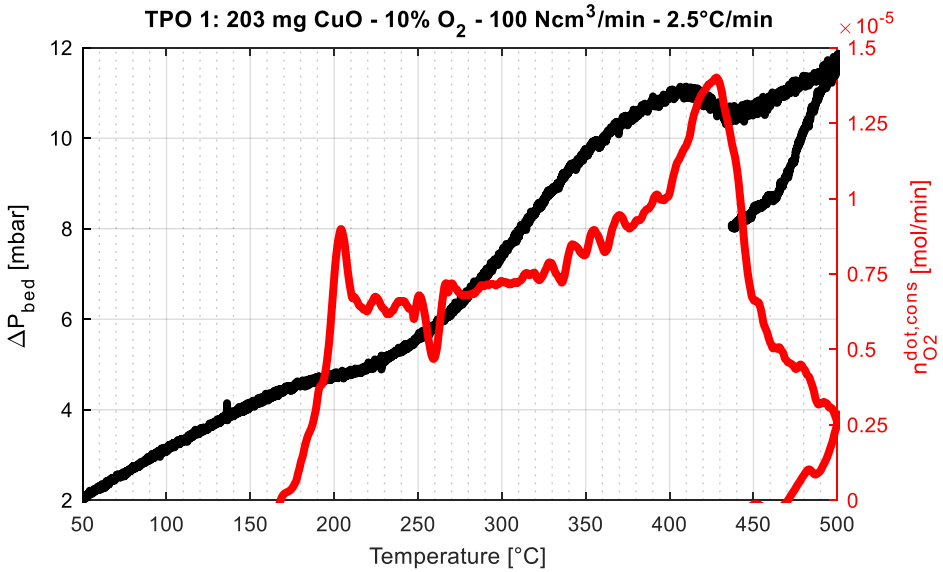

***Figure 4.22**: Oxygen consumption and pressure drop through the bed during the first TPO.*

***Table 4.14**: Relevant data concerning the first TPO run.*

TPO number [-]	T_{act} [°C]	$T_{peak,1}$ [°C]	T_s [°C]	$n_{O,CuO}^{reg}$ [mol]	$\%_{O,CuO}^{reg}$ [%]
1	160	205	425	$2.22 \cdot 10^{-3}$	87.7

As shown by the gathered data, the first TPO carried out on the sample shows two distinct peaks. The temperatures at which the peaks are found have been confirmed by the profiles obtained through the mass spectrometer.

The degree of oxidation is greater than the preceding TPR degree of reduction (+5.8%). As already mentioned in §4.1.2, a possible explanation could be the formation of some copper peroxide, but in this case an underestimation of the hydrogen consumed during the previous TPR seems more likely, since the values of $\%_{O,CuO}^{cons}$ agrees with the first TPO quantifications of §4.2.2.2 (+0.3%).

To see if the absence of the oxidant pre-treatment could have influenced the bed structure, and to confirm the correlation between the reduction process and the agglomeration, the bed pressure drop $\Delta P_{bed}(\dot{V})$ has been measured as in §4.2.2 before the pre-treatment, after the pre-treatment and after the first TPR. The experimental measurements coupled with their fitting are shown in Figure 4.23.

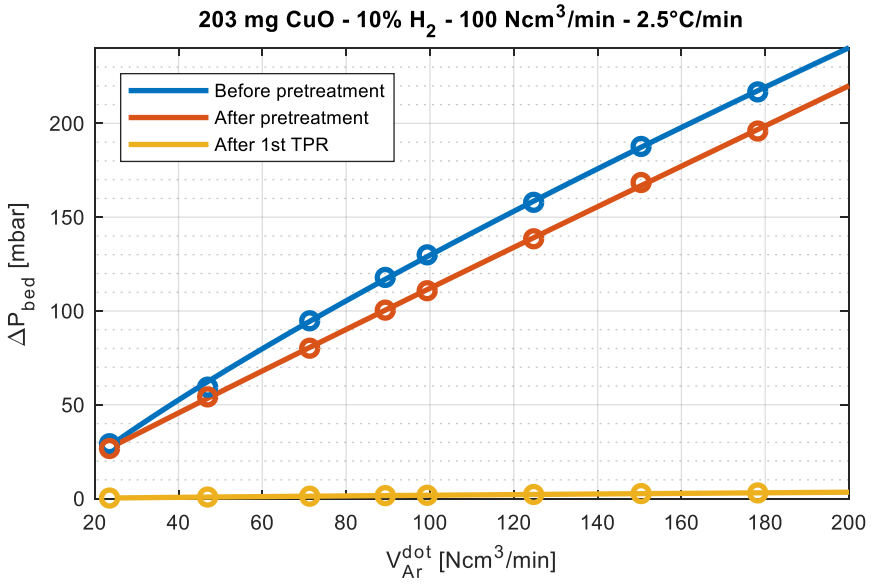

***Figure 4.23**: Pressure drop variation before the pre-treatment, after the pre-treatment and after the TPR.*

As the plot shows, the pressure drop generated by the bed is visibly lower when measured after the reduction process, proving that the agglomeration of the bed happened during the TPR cycle. On the other hand, also the inert pre-treatment made the bed shrink slightly, as the measured pressure drop is lower than the one measured before the pre-treatment.
If the values obtained while flowing 100 Ncm^3/min of argon are taken as reference, a gap of 20 mbar before the pre-treatment and after the pre-treatment is measured. The corresponding value for the previous test, instead, was of approximately 1 mbar. If these values are related to the total gap in the pressure drop before the pre-treatment and after the TPR, in the first case the pre-treatment contributes for the 15.5% to the total pressure drop evidenced, while in the second case this contribution is only of 1.7%. Given these results, it is suggested that the pre-treatments affect the bed agglomeration only slightly.

4.2.3.2 Sample characterization

As done with the previous tests, the sample has been visually inspected and the same structure as §4.2.2.3 has been found. Moreover, the sample has been analysed with the Scanning Electron Microscope: as Figure 4.24.a shows, the oxidised sample surface still retained a granular-looking surface, even if the particles sides have been smoothed and the particles visibly merged. If an enlargement is made, fibres of approximately 100 nm of diameter are seen on the sample surface, as reported in Figure 4.24.b. Since they seem to be present in higher number with respect to the two previous cases (see Figure 4.18.a and Figure 4.6.b), it could be concluded that their number and length decrease as the reactive cycles increase.

In addition to the fibres, also protuberances are found, as the focus of Figure 4.25 reports: the breakage of one showed that a crust formed also after one redox cycle. This layer, which is as deep as 600 nm, covered the remaining particles, which still retained a granular shape. Since Figure 4.25.b highlights that the depth of this layer was of approximately 1 μm after two redox cycles and 3 μm after eleven redox cycles, it can be concluded that this layer depth increases as the reactive cycles are performed, hindering more the inward diffusion of reagent.

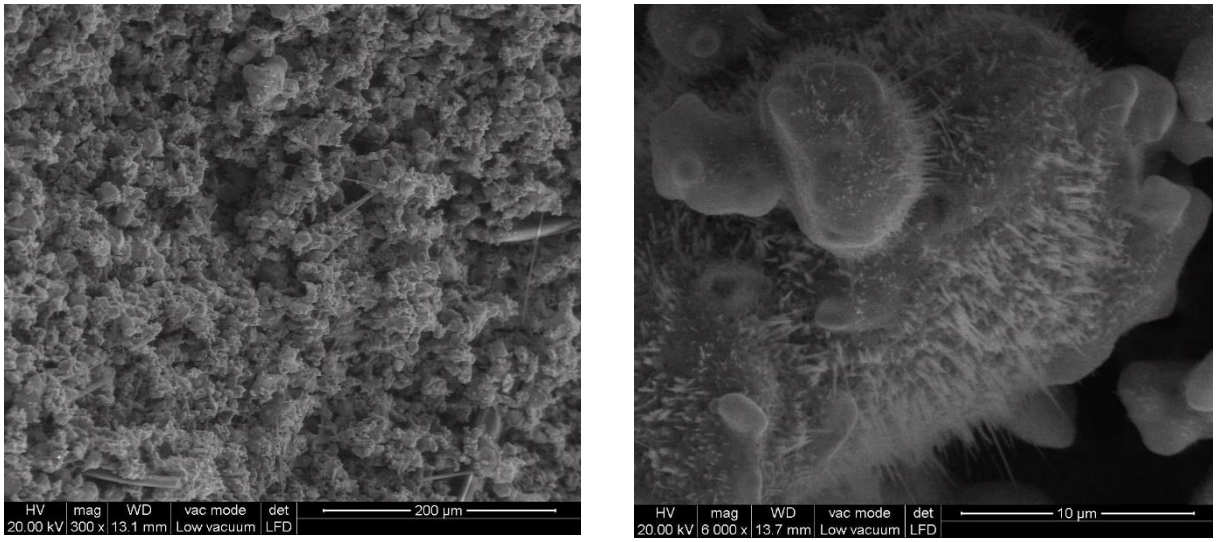

(a) (b)

Figure 4.24*: SEM image of* (a) *the sample surface and* (b) *enlargement of the external surface.*

Figure 4.25*: SEM image of the sample surface: focus on a broken protuberance.*

4.3 Bed height minimization

Since Malet and Caballero [9] experimentally obtained two distinct peaks using very low cupric oxide masses (i.e. with 5 or 10 mg of CuO, refer to curves *a* and *b* of Figure 1.6), one redox cycle has been performed using a lower quantity of cupric oxide. The setup described in §2 has been used, and the procedure described in §2.5 has been followed.

To keep the parameter K equal to 367.5 s while having a smaller mass to be analysed, the feed concentration has been reduced. The cupric oxide bed features are reported in Table 4.15, while the parameters of each cycle are reported in Table 4.16.

In this case, forming a homogeneous layer of cupric oxide was difficult because of the lower mass to be analysed, whose particles dispersed on the supporting quartz wool piece. Because of the low resulting height of the bed, which is shown once placed into the reactor in Figure 4.26, the difference between the measured $\Delta P_{system}(T)$ and $\Delta P_{line}(T)$ were minimal, and both the ΔP_{bed} during the thermal cycles and at ambient temperature have not been calculated. As happened in the previous tests, some of the particles adhered to the internal surface of the reactor, and have been trapped by the upper quartz wool bed as it was positioned.

Table 4.15: *Cupric oxide bed features.*

Parameter	Symbol	Unit of measure	Values
Main reagent species	-	-	CuO
Sample purity	-	[%]	99.995
Sample mass	m_s	[mg]	9.9
Sample molecular weight	MW_s	[g/mol]	79.54
Sample molar amount	n_s	[mol]	$1.24 \cdot 10^{-4}$
Sample particle size range	d_p	[μm]	<45
Particle bed height	H_{bed}	[mm]	<1
Particle bed volume	V_{bed}	[cm^3]	n.a.

Table 4.16*: Thermal cycles parameters.*

	Cycle [-]	Inert [-]	Reagent [-]	$\dot{V}_{tot}$ [Ncm^3/min]	y_R [%]	$\dot{n}_R^{in}$ [mol/min]	β [°C/min]	T_{fin} [°C]	t_s [min]
Inert pre-treatment	1	Ar	-	50	-	-	5	200	30
Oxidant pre-treatment	2	Ar	O_2	50	1	$4.16 \cdot 10^{-5}$	5	250	60
TPR	3	Ar	H_2	50	1	$4.16 \cdot 10^{-5}$	2.5	500	0
TPO	4	Ar	O_2	50	1	$4.16 \cdot 10^{-5}$	2.5	500	0

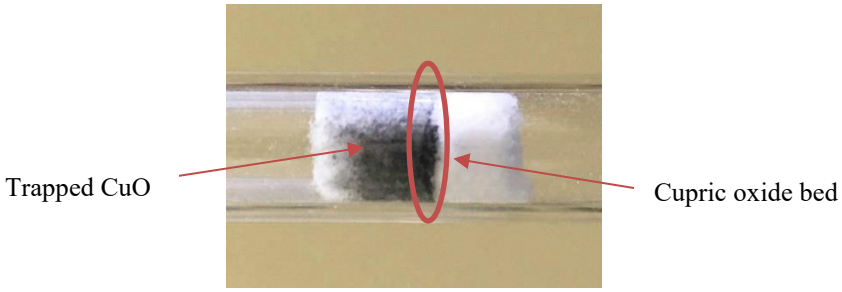

***Figure 4.26**. Cupric oxide bed appearance.*

4.3.1 Redox cycles results

The results of the TPR and TPO cycles are presented in Figure 4.27, Figure 4.28, Table 4.17 and Table 4.18.

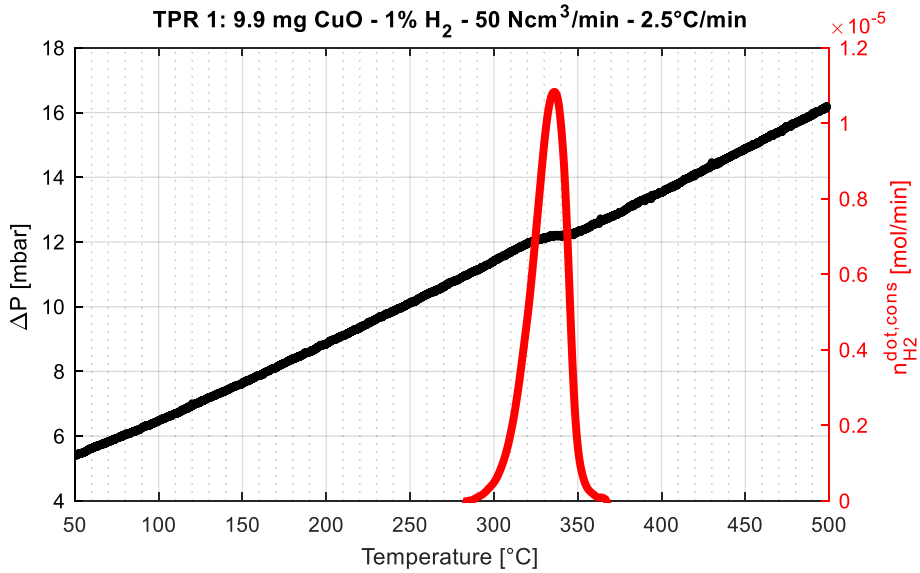

***Figure 4.27**: : Hydrogen consumption and pressure drop through the bed during the first TPR.*

***Table 4.17**: Relevant data concerning the first TPR run.*

TPR number [-]	T_{act} [°C]	$T_{peak,1}$ [°C]	Secondary peak(s)	T_s [°C]	Peak range [°C]	$n_{O,CuO}^{cons}$ [mol]	$\%_{O,CuO}^{cons}$ [%]
1	280	335	-	-	90	$1.15 \cdot 10^{-4}$	90.6

Differently from the experimental results of Malet and Caballero, using a lower quantity of catalyst a single peak is produced in the reduction process, at higher temperatures with respect to the one obtained by the authors (307°C against 227°C). Since the two parameters that differed in this case were the hydrogen concentration (i.e. 1% against 5%) and the heating rate (2.5°C/min against 10°C/min), and from the results of Monti and Baiker [5] it is evidenced that

a more concentrated mixture shifts the peak towards lower temperatures, it is supposed that the heating rate could be the responsible of the multiple peaks observed by the authors. This is reasonable, as a higher heating rate could favour the development of temperature gradients inside the bed. Such temperature inhomogeneity could increase the kinetic rates in the hotter zones, increasing the hydrogen consumption rates, and so the hydrogen consumed, resulting in additional peaks.

The slight inflections on the pressure drop registered by the pressure transducer as the peak is formed, moreover, suggest that also in this case the bed has slightly agglomerated during the reduction. The bed agglomeration, combined with the lower hydrogen concentration in the feed, could have been the responsible of the slightly low degree of reduction observed. If the reagent diffusion through the shell is limiting, indeed, the inner particle reduction could be further hindered because of the low driving force (i.e. the concentration gradient) provided when feeding a more diluted mixture. In this case, some unreacted copper or some cuprous oxide can be expected in the bulk of the solid phase.

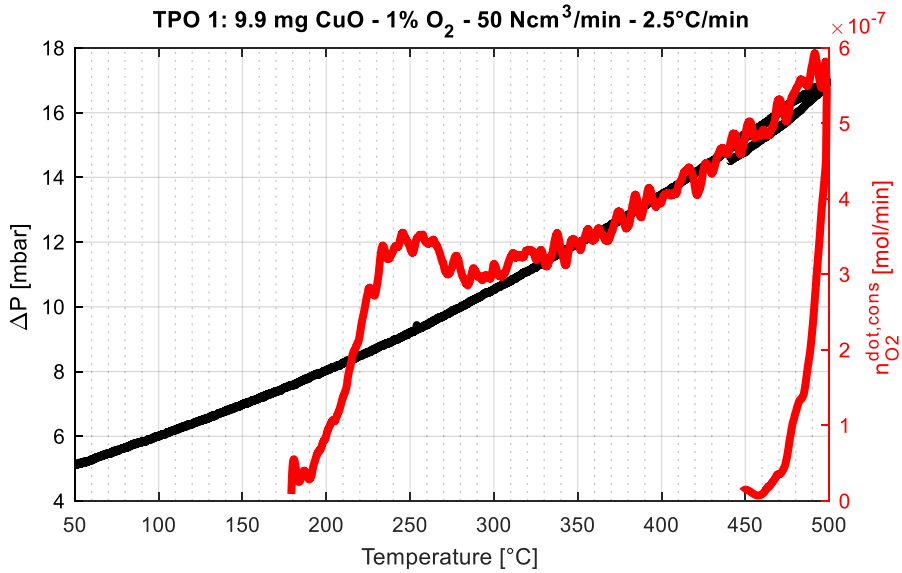

***Figure 4.28**: Oxygen consumption and pressure drop through the bed during the first TPO.*

***Table 4.18**: Relevant data concerning the first TPO run.*

TPO number [-]	T_{act} [°C]	$T_{peak,1}$ [°C]	$T_{peak,2}$ [°C]	$n_{O,CuO}^{reg}$ [mol]	$\%_{O,CuO}^{reg}$ [%]
1	176	250	500	$1.07 \cdot 10^{-4}$	84.4

Also in the TPO profile both the activation temperature and the one of the first peak shift towards higher T with respect to the preceding tests, and the second peak is reached at the final temperature explored (T=500°C). This shift of the peak suggests that the diffusion through the

layer formed during the reduction could be limiting. A lower oxidation degree is found with respect to the one of the preceding TPR (-6.2%): as stated in the previous chapters, this fact suggests that not all the copper and cuprous oxide present are oxidised back to cupric oxide, and consequently some additional cuprous oxide could be found in the sample.

4.3.2 Visual inspection

As expected by observing the pressure drop behaviour during the reduction, the bed agglomerated during the reduction cycle: the powder merged in granules of higher diameter, and sticked to the quartz wool pieces, as reported in Figure 4.29. This is a quite interesting result, because even with a low catalyst mass, low concentrations of reagent and higher dispersion the agglomeration could not be avoided. At the same time, although the initial bed height was minimized, the differential pressure transmitter proved to be sensible enough to detect the phenomenon.

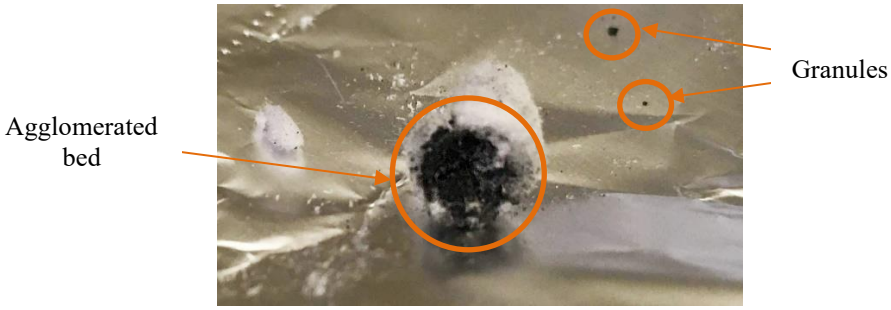

***Figure 4.29**: Appearance of the 10-mg copper oxide bed after the redox cycle.*

4.4 Bed dilution with silicon carbide

Since the results of the previous tests suggested that temperature gradients could arise in the reactive bed, the influence of a bed dilution with silicon carbide has been investigated. As a starting point, the thermal properties of the solid compounds and elements involved in the processes studied are shown in Table 4.19 [15][20][21]. As the table shows, silicon carbide should increase the heat propagation among the bed particles thanks to its high thermal conductivity, thus reducing thermal gradients in the bed. Moreover, its presence among the reacting particle could also prevent their agglomeration.

In this test a silicon carbide-bed dilution with the same mass of cupric oxide has been done. The same granulometry has been used not to affect the fluid dynamics of the bed. The setup described in §2 has been used, but since the bed height after mixing resulted in high pressure drop generation, a quartz tubular reactor with the internal diameter equal to 8 mm has been used. The resulting bed features are summarized in Table 4.20, while its appearance before and after the mixing is shown in Figure 4.30.

***Table 4.19**: Thermal properties of the compounds involved in the processes.*

	c_p [J/Kg/K]	λ [W/m/K]	T_m [°C]
CuO	705	6	1326
Cu_2O	489	4.5	1235
Cu	460	350	1085
SiC	675	490	2730

***Table 4.20**: Cupric oxide bed features.*

Parameter	Symbol	Unit of measure	Values
Main reagent species	-	-	CuO
Sample purity	-	[%]	99.995
Sample mass	m_s	[mg]	201
Sample molecular weight	MW_s	[g/mol]	79.54
Sample molar amount	n_s	[mol]	$2.54 \cdot 10^{-3}$
Sample particle size range	d_p	[μm]	<45
Diluent type	-	-	SiC
Diluent mass	m_d	[mg]	206
Diluent particle size range	d_p	[μm]	<45
Bed height	H_{bed}	[mm]	6
Bed volume	V_{bed}	[cm^3]	0.302

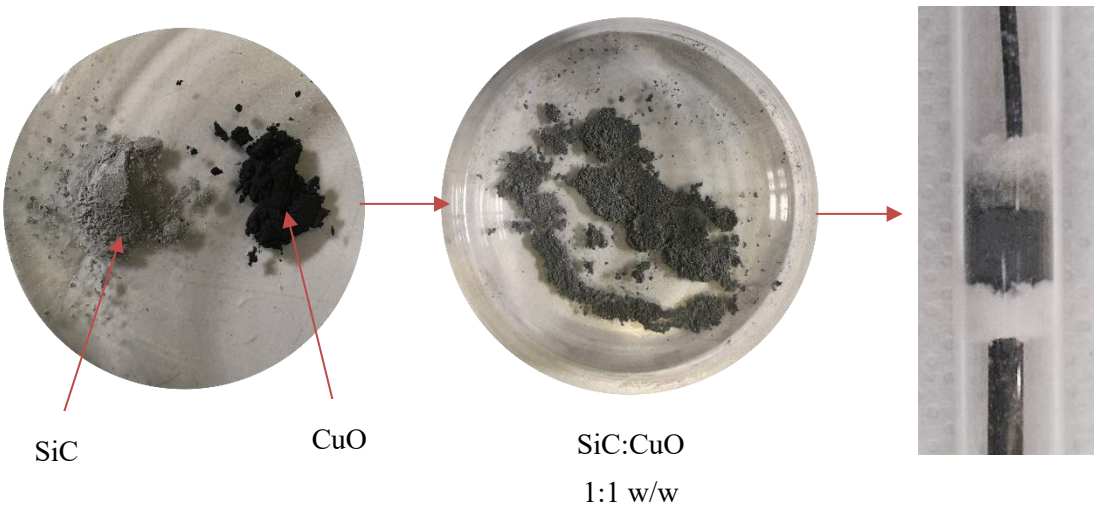

***Figure 4.30**: Appearance of the components before mixing and after mixing, and appearance of the cupric oxide bed.*

This test included a thermal cycle under inert flow, a thermal cycle under oxidant mixture, and four TPR-TPO cycles performed in sequence. Each cycle has been carried out with the

corresponding parameters shown in Table 4.21. The pressure drop over the bed has been monitored during each thermal cycle and retrieved after each thermal cycle at ambient temperature following the procedure outlined in §4.2.2.1.

***Table 4.21**: Experimental parameters used in the cycles.*

	Inert [-]	Reagent [-]	$\dot{V}_{tot}$ [Ncm³/min]	y_R [%]	$\dot{n}_R^{in}$ [mol/min]	β [°C/min]	T_{fin} [°C]	t_s [min]
Inert thermal cycle	Ar	-	100	-	-	5	200	30
Oxidant thermal cycle	Ar	O_2	100	10	$4.16 \cdot 10^{-4}$	5	250	60
TPR	Ar	H_2	100	10	$4.16 \cdot 10^{-4}$	2.5	500	0
TPO	Ar	O_2	100	10	$4.16 \cdot 10^{-4}$	2.5	500	0

4.4.1 Redox cycles results

The results of the four TPR cycles are presented in Figure 4.31 and in Table 4.22.

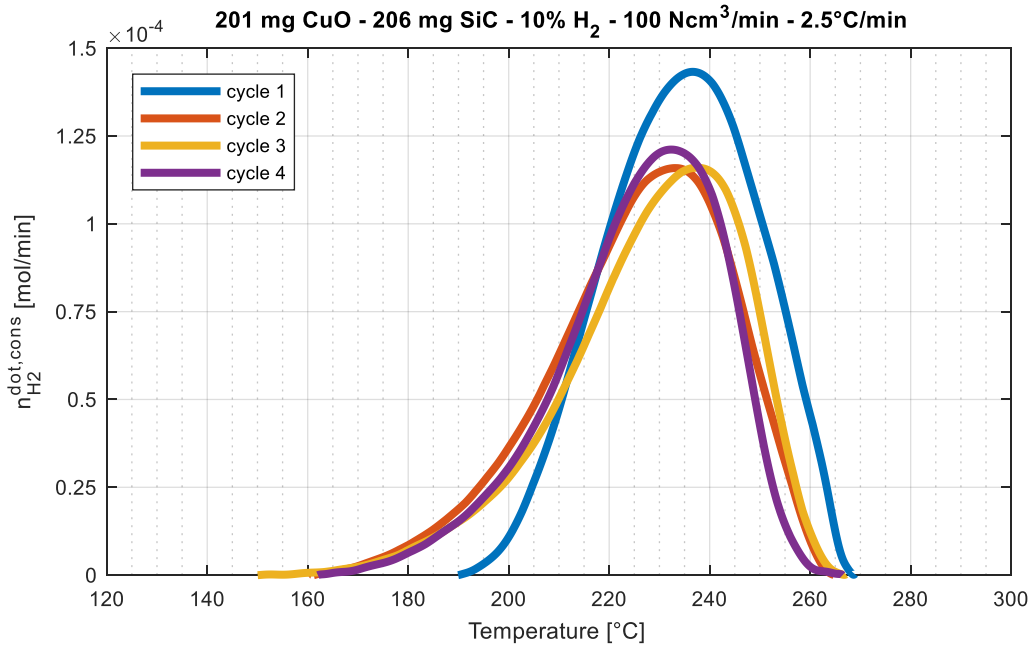

***Figure 4.31**: Hydrogen consumption during the four TPRs.*

***Table 4.22**: Relevant data concerning the four TPR run.*

TPR number [-]	T_{act} [°C]	$T_{peak,1}$ [°C]	Secondary peak(s)	T_s [°C]	Peak range [°C]	$n_{O,CuO}^{cons}$ [mol]	$\%_{O,CuO}^{cons}$ [%]
1	193	236	-	-	78	$2.28 \cdot 10^{-3}$	89.9
2	155	238	-	-	111	$2.06 \cdot 10^{-3}$	81.3
3	155	240	-	-	111	$1.99 \cdot 10^{-3}$	78.4
4	174	234	-	-	84	$1.94 \cdot 10^{-3}$	76.4

As Figure 4.31 shows, every reduction produces a single peak, whose temperature remains almost equal during the four cycles (i.e. 237±3 °C). The first peak distinguishes from the other for its slightly higher initial reaction rate, and the higher degree of reduction, which surpasses all the others obtained in the first TPRs using 200 mg of sample. As discussed in §4.4, these effects could be related to the high thermal conductivity of the silicon carbide used in these tests. This suggests that conduction plays a significant role in the system studied, and that the formation of temperature gradients in the bed could be the real cause of the secondary peaks.
The following three cycles shows almost superimposable profiles and almost equal degrees of reduction. Moreover, since left-skewed profiles are obtained for cycle 2, 3 and 4, it is suggested that the same phenomena explained in §4.2.2.2 for the second reduction cycle develop (i.e. the generation of structural defects that decrease the activation temperature, and the specific surface area decrease that lowers the reaction rate).
The four TPO profiles are shown in Figure 4.32, while the data regarding each TPO are shown in Table 4.23.

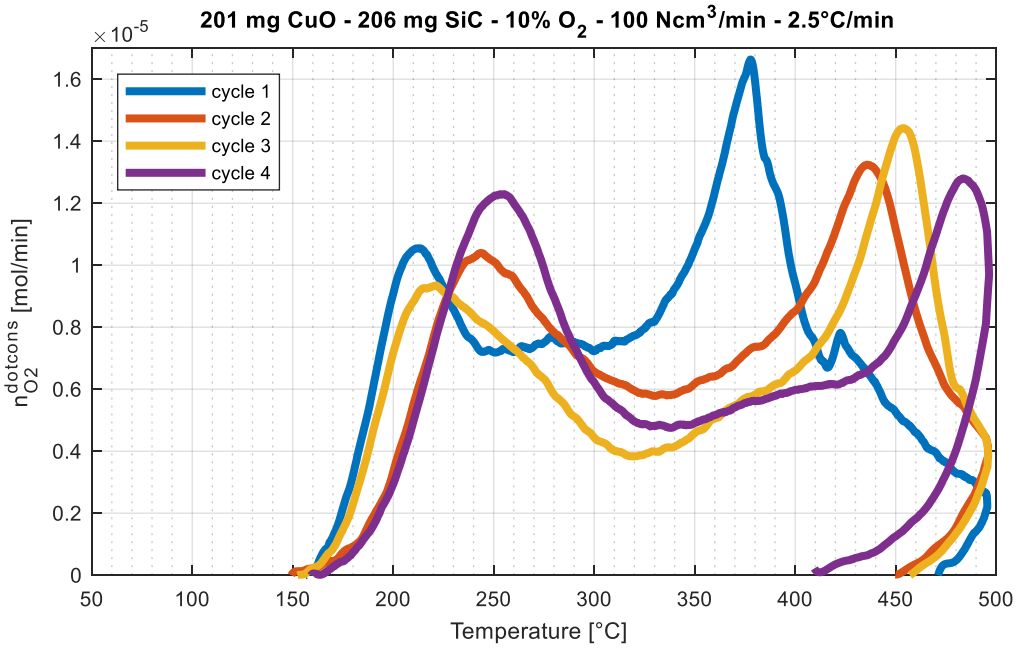

***Figure 4.32**: Oxygen consumption during the four TPOs.*

Table 4.23: *Relevant data concerning the four TPO run.*

TPO number [-]	T_{act} [°C]	$T_{peak,1}$ [°C]	$T_{peak,2}$ [°C]	$n_{O,CuO}^{reg}$ [mol]	$\%_{O,CuO}^{reg}$ [%]
1	159	210	377	$2.16 \cdot 10^{-3}$	85.4
2	150	243	436	$1.99 \cdot 10^{-3}$	78.6
3	152	221	455	$1.87 \cdot 10^{-3}$	73.8
4	158	253	483	$1.99 \cdot 10^{-3}$	78.3

All the TPOs shape exhibit a double-peak shape (i.e. a mechanism consisting in two steps), which all have a better resolution than the ones obtained in §4.2.2 and §4.2.3 without dilution, and do not show any additional peak.

The results also suggest that the second peak always shifts towards higher temperatures as the cycle number increases, remembering the results obtained in §4.1.2. Conversely, the first peak does not follow this rule, as in cycle 3 its anticipation is evident and its initial reaction rate is higher. This fact could be derived from experimental error or from random phenomena.

Overall, it could be observed that adding the silicon carbide to the bed favours the resolution of the oxidation peaks. Combining the high exothermicity of the oxidation process with the good results obtained with the silicon carbide, it could be supposed that the thermal effect developed during the TPOs has a great impact on the results of the analysis.

The sequential degrees of reduction and oxidation, finally, suggest that in the first three cycles both the reductions and the oxidations are not complete, since the $\%_{O,CuO}^{cons}$ value for each cycle is smaller than its previous one. This trend is not followed in the fourth cycle, as its reduction degree is higher than the third oxidation degree and is surpassed also by the fourth oxidation degree. Being these differences small, however, they could be associated with experimental errors.

Also in this test the pressure drop variation with the argon flowrate at ambient temperature has been measured after every thermal cycle, and the $\Delta P_{bed}(\dot{V})$ calculated as in Equation (4.1). The results reported in Figure 4.33 suggest that the bed agglomerated considerably both during the first TPR and during the first TPO, as the two major gaps in the curves are found when these two cycles are involved.

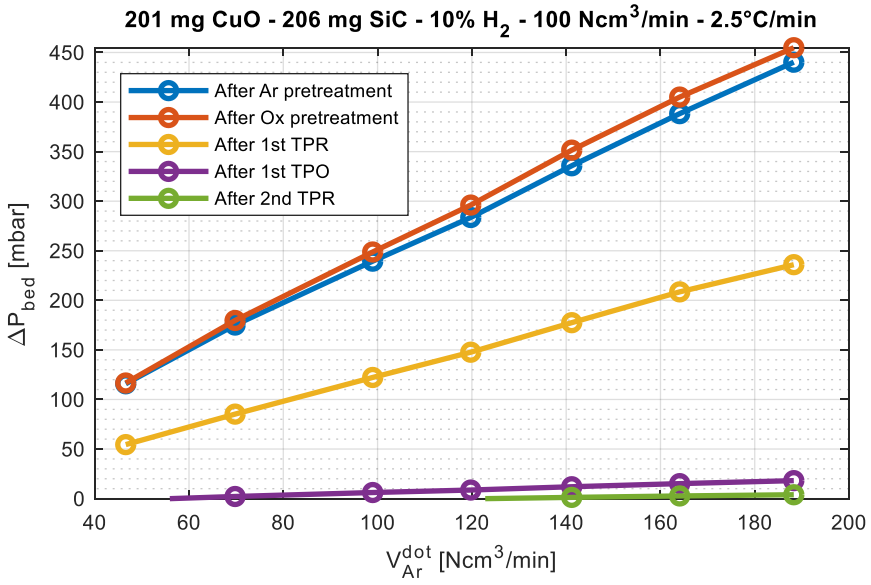

***Figure 4.33**: Pressure drop variation in the diluted bed, at ambient temperature.*

This effect is also proved by the pressure drop registered while the reactive cycles were performed, as shown in Figure 4.34: during the first TPR, indeed, a pressure drop fall is detected in correspondence of the peak, and at the end of the first TPO a dramatic fall is registered. This suggests that the agglomeration continued as the two processes were carried out, and that towards the end of the TPO by-passes were created in the bed.

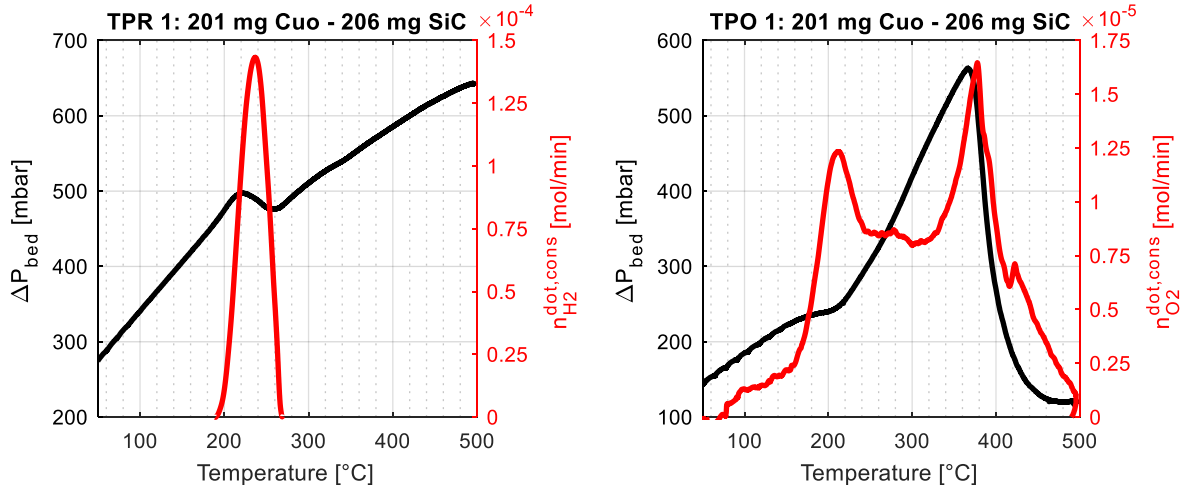

(a) (b)

***Figure 4.34**: Pressure drop variation in the diluted bed during* (a) *the first TPR and* (b) *the first TPO.*

It is then concluded that the bed dilution with silicon carbide helps to level out temperature gradients inside the diluted bed also in the case of TPOs, but does not prevent its almost-

complete agglomeration, even if this process is delayed to the end of the first TPO. This is proven by the final shape of the bed, which becomes a compact cylinder during the process, as reported in Figure 4.35.a. Its axial shrinkage is smaller than 1 mm but still observable, as shown in Figure 4.35.b. Moreover, as happened with the diluted bed samples of §3, also in this case the external by-passes created during the oxidation are visible and evidenced in Figure 4.35.c. As the figures show, the agglomeration was quite pronounced, but the decrease in bed volume was not as high as the cases shown in §4.2.2 and in §4.2.3.

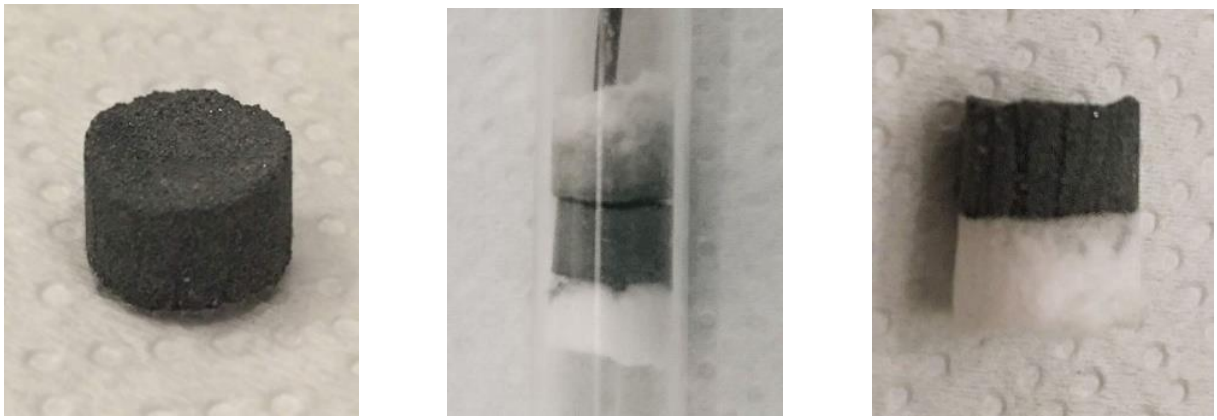

(a) (b) (c)

Figure 4.35*: Diluted sample appearance after the fourth TPO:* (a) *final shape,* (b) *focus on the axial shrinkage and* (c) *focus on the by-passes.*

4.5 TPR and TPO profiles at constant K

Since all the tests displayed from §4.1 to §4.4 have been carried out with a K parameter equal to 367.5 s and a heating rate equal to 2.5 °C/min, a comparison among the reagent consumption profiles obtained both during reduction and oxidation is done. The TPR and TPO profiles obtained are thus overlapped in Figure 4.36 and Figure 4.37 respectively. Whenever more than one cycle was performed, only the first TPR and TPO run data were reported.

The data summarizing the experimental conditions used in the tests are reported on Table 4.24 to simplify the results reading.

***Table 4.24**: Relevant data concerning the 5 tests at K=367.5 s.*

Set	m_s [mg]	$\dot{V}_{tot}$ [Ncm3/min]	y_R [%]	Bed dilution	Ox. Pre-treatment	$\%_{O,CuO}^{cons}$ [%]	$\%_{O,CuO}^{reg}$ [%]
1	51	50	5	-	✔	96.0	98.2
2	203	100	10	-	✔	87.2	87.4
3	203	100	10	-	-	81.9	87.7
4	9.9	50	1	-	✔	90.6	84.4
5	201	100	10	✔	✔	89.9	85.4

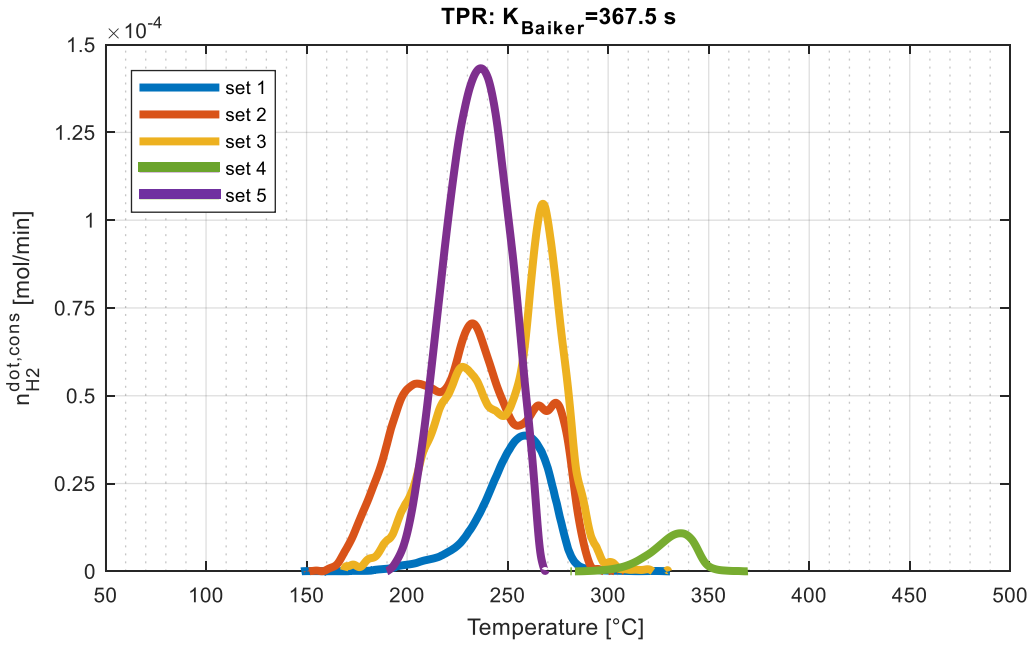

***Figure 4.36**: TPR profiles of the test with K=367.5 s.*

As shown by the figure above, one peak is obtained when low masses of sample are used, or when the bed is diluted with silicon carbide: as suggested in §4.4, this effect could be related to the temperature gradient generation on the reactive bed, which are smaller in the case of a having a bed with lower height, or when a diluent with a high thermal conductivity is used. This suggests that the prevailing mechanism of heat transfer in the solid phase is conduction, and that this phenomenon is critical to have the complete reduction of the bed in a short time (i.e. in a smaller temperature range). Moreover, as the principal peak is shifted towards higher temperatures if lower hydrogen concentrations are used, the diffusion through the bed seems to be crucial, being it driven by the concentration gradient.

Since all these profiles are obtained with the same K parameter, it is concluded that this number is not adequate to establish the experimental conditions which favours a homogeneous reduction of the bed. The multiple-peak phenomenon seems to be related to an uneven

temperature distribution in the sample, or to the physical changes in the reactive bed rather than the reduction being carried out in multiple reactive steps, since a single and well-defined peak is obtained in set 5 using the same parameters of set 2 and 3, but with the addition of a diluent having high thermal conductivity and capable of preventing the total agglomeration of the sample.

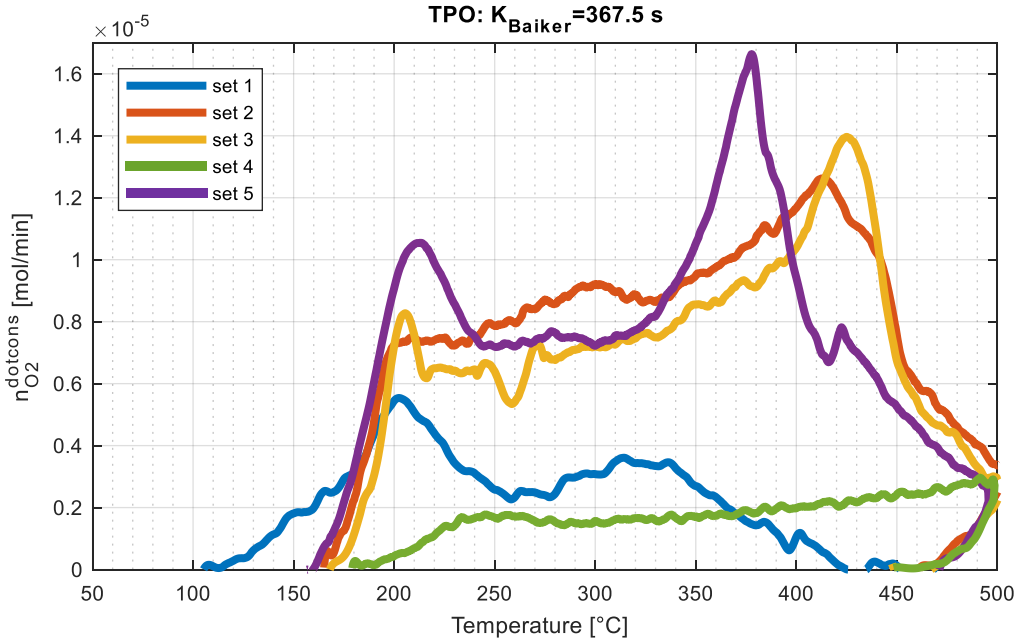

***Figure 4.37**: TPO profiles of the test with K_{Baiker}=367.5 s.*

Looking at the TPO results, two peaks are produced in every case, the second one (at higher temperature) being always the one at which there is a higher oxygen consumption (except for test 1, on which a different cupric oxide has been used, refer to Table 4.1). The second peak is shifted towards lower temperatures using a bed dilution with a highly conductive material, indicating that the cuprous oxide transition to cupric oxide is favoured when temperature gradients are levelled out in the sample. The fact of having two well-resolute peaks in this case also suggests that a more homogeneous temperature distribution in the sample promotes the oxidation in two distinct steps.

When a low concentration of reagents is used, both the peaks shift towards higher temperatures, which suggests that in oxidations, as well as in reductions, the diffusion is a limiting factor.

If the efficiency of each reactive cycle is observed (i.e. $\%_{O,CuO}^{cons}$ and $\%_{O,CuO}^{reg}$), it could be observed that, whenever high concentrations of reagent are used and the bed is not diluted, the oxygen consumption is higher than the hydrogen consumption of the preceding TPR: this fact suggests that the bed dilution slightly hinders the first oxidation.

4.6 Axial temperature profile measurement

Since the previously-exposed results suggests the formation of a temperature gradient in the bed, which seems to be lowered using a bed dilution with silicon carbide, a larger bed has been studied and its temperature axial profile during the thermal cycles has been registered using a multipoint thermocouple. This experiment has been done both with a diluted bed and with a pure cupric oxide one, and the results are shown below.

4.6.1 Silicon carbide bed dilution

The first experiment aimed to investigate if an axial temperature profile arises as TPR and TPO analyses are carried out. The cupric oxide bed has been diluted with a mass of silicon carbide 20 times larger than the cupric oxide one to verify if the particles could still agglomerate in the process even if, theoretically, they were isolated one from each other. To investigate on this thermal effect, the setup presented in §2.4 has been used. The cupric oxide bed features are presented instead in Table 4.25.

***Table 4.25**: Cupric oxide bed features.*

Parameter	Symbol	Unit of measure	Values
Main reagent species	-	-	CuO
Sample purity	-	[%]	99.995
Sample mass	m_s	[mg]	472
Sample molecular weigth	MW_s	[g/mol]	79.54
Sample molar amount	n_s	[mol]	$5.93 \cdot 10^{-3}$
Sample particle size range	d_p	[μm]	100-200
Diluent type	-	-	SiC
Diluent mass	m_d	[mg]	9478
Diluent particle size range	d_p	[μm]	100-200
Bed height	H_{bed}	[mm]	59
Bed volume	V_{bed}	[cm^3]	6.67

The appearance of the bed after mixing the two components, shown in Figure 4.38.a, is instead presented in Figure 4.38.b: as no visible segregation appears, perfect mixing of the two phases is supposed.

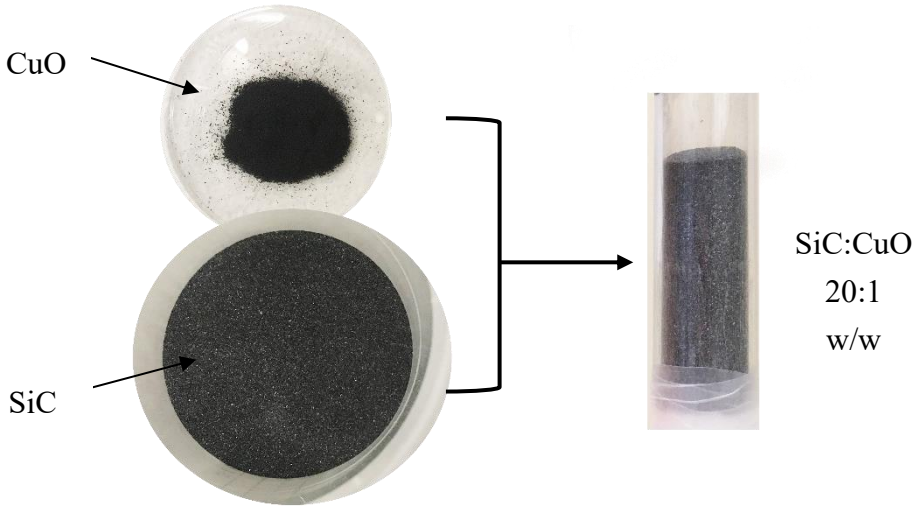

***Figure 4.38**: Bed components* (a) *before mixing and* (b) *after mixing.*

Taking as reference the reactor scheme of Figure 2.11, the monitoring thermocouple used in this test was T9, while T10 lied outside of the bed, and the bed covered all the monitored points up to T1.

This test included a sample pre-treatment, consisting of one thermal cycle in inert gas and one thermal cycle in oxidant mixture, followed by two redox cycles, whose parameters are reported in Table 4.26. All the cycles have been carried out using a reagent concentration of 10%, apart from the first TPR in which a lower reagent concentration has been used (i.e. 1% H_2) to study the effect of a slower reaction on the axial temperature profile.

***Table 4.26**: Experimental parameters used in the cycles.*

	Cycle [-]	Inert [-]	Reagent [-]	$\dot{V}_{tot}$ [Ncm^3/min]	y_R [%]	$\dot{n}_R^{in}$ [mol/min]	β [°C/min]	T_{fin} [°C]	t_s [min]
Inert thermal cycle	1	Ar	-	250	-	-	5	200	30
Oxidant thermal cycle	2	Ar	O_2	250	10	$1.04 \cdot 10^{-3}$	5	250	60
TPR	3	Ar	H_2	250	1	$1.04 \cdot 10^{-4}$	2	500	0
TPO	4	Ar	O_2	250	10	$1.04 \cdot 10^{-3}$	2	500	180
TPR	5	Ar	H_2	250	10	$1.04 \cdot 10^{-3}$	2	500	0
TPO	6	Ar	O_2	250	10	$1.04 \cdot 10^{-3}$	2	500	30

4.6.1.1 Redox cycles results

The results of the two TPR cycles are shown in Figure 4.39 and Table 4.27.

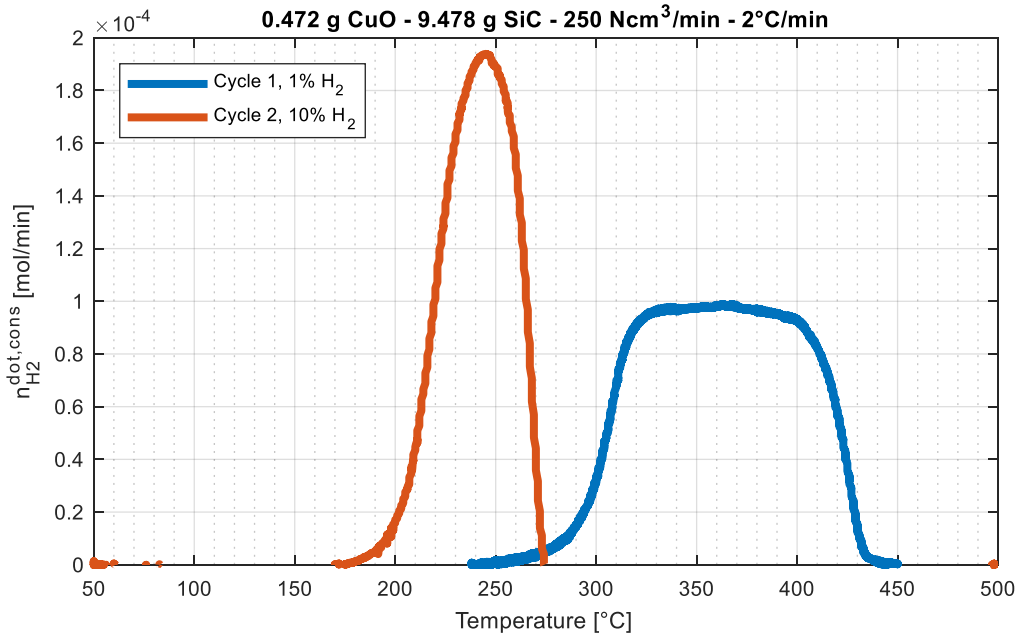

***Figure 4.39**: Hydrogen consumption profiles of the two TPR run with 20:1 w/w SiC dilution.*

***Table 4.27**: Relevant data concerning the two TPR run.*

TPR number [-]	K [s]	T_{act} [°C]	$T_{peak,1}$ [°C]	Secondary peak(s)	T_s [°C]	Peak range [°C]	$n_{O,CuO}^{cons}$ [mol]	$\%_{O,CuO}^{cons}$ [%]
1	3453	193	361	-	-	210	$5.76 \cdot 10^{-3}$	97.3
2	345	177	246	-	-	97	$4.82 \cdot 10^{-3}$	81.4

As data shows, even with a high quantity of cupric oxide to be reduced and the K parameter lying out of the suggested range, one peak forms in both cases. As observed in §3.1.4, with low hydrogen concentration the peak is flattened and the peak range becomes wider: this happens because almost all the reagent fed is consumed from T=323°C to T=400°C. Moreover, the sample seems to have reduced almost entirely even with a high bed dilution and with a low reagent concentration, meaning that the reagent reached almost all the particles and their core. On the other hand, the second TPR run showed a narrower peak centred at lower temperatures and a lower degree of reduction.

As it could be expected by the high dilution used and the low reagent concentration, the axial temperature profile at peak conditions of the first TPR run gives uniform axial T, as it is shown in Figure 4.40.a. This is reasonable, since the reaction is slow and the reaction heat is distributed thanks to the high thermal conductivity of the silicon carbide. Similar profiles are obtained for the second TPR (Figure 4.40.b), which underlines the capability of silicon carbide to level out temperature gradients inside the sample.

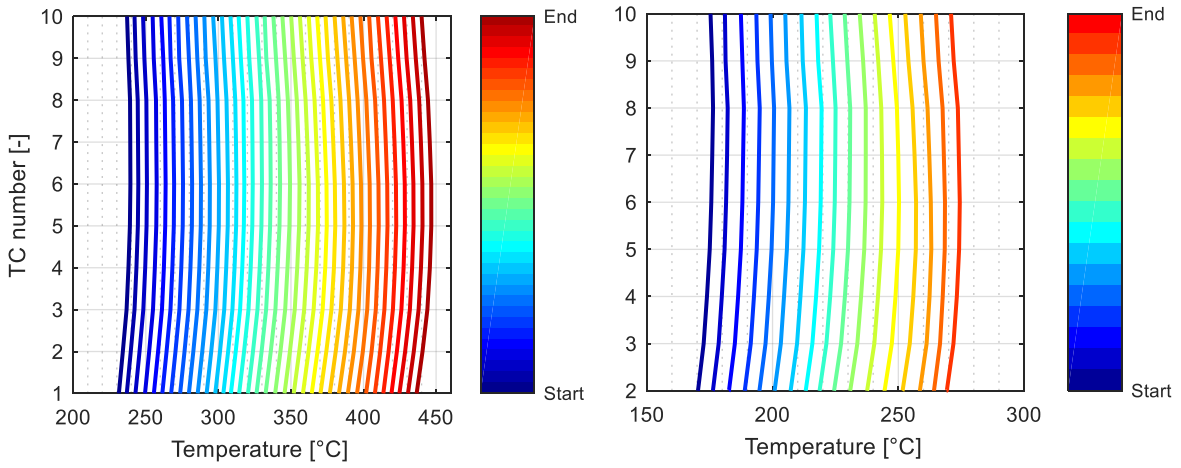

***Figure 4.40**: Axial temperature profiles at peak conditions (step size: 3 min)* (a) *for the first TPR run and* (b) *for the second TPR run.*

The results of the two TPO carried out after each TPR are shown in Figure 4.41 and Table 4.28. Note that the isothermal step is not shown in the figure.

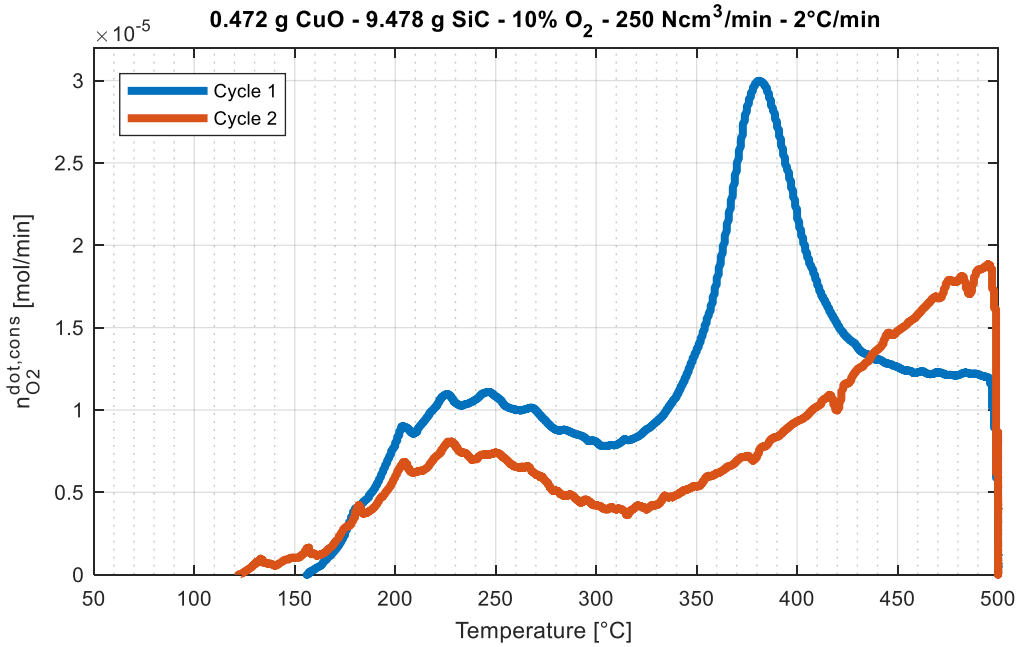

***Figure 4.41**: Oxygen consumption profiles of the two TPR run with 20:1 w/w SiC dilution.*

***Table 4.28**: Relevant data concerning the two TPO run.*

TPO number [-]	T_{act} [°C]	$T_{peak,1}$ [°C]	$T_{peak,2}$ [°C]	$n_{O,CuO}^{reg}$ [mol]	$\%_{O,CuO}^{reg}$ [%]
1	159	230	381	$4.81 \cdot 10^{-3}$	81.2
2	118	232	500	$3.85 \cdot 10^{-3}$	65.0

As seen by the data, both TPOs show two peaks as found in the preceding tests. In both cases the first one is distorted because of the small temperature oscillations of the furnace, but the temperature at which it is detected is almost coincident. The second peak, instead, moves towards higher temperatures in the second run, following the behaviour of the second peaks of the preceding results. Differently from the results of §4.4.1, it seems that a high bed dilution (i.e. 20:1) with silicon carbide does not prevent the shift of the second peak towards temperatures greater than 500°C in the second TPO.
Even if in the first run the sample remained in the oxidant mixture at 500°C for three hours, the degree of the oxidation is smaller than the one expected (i.e. -16.1% with respect to the previous TPR result), and the second oxidation efficiency is further lowered. Both these facts suggest that a high bed dilution hinders the complete oxidation of the sample, probably because of preferential passages created in the bed, whose height and dilution are high. On the other hand, the complete oxidation of the bed could have been hindered also by the sample slight agglomeration during the first TPR.
As done with the previous TPRs, the temperature profiles acquired during the oxidation are plotted and shown in Figure 4.42, but no visible thermal increase is detected in both cases.

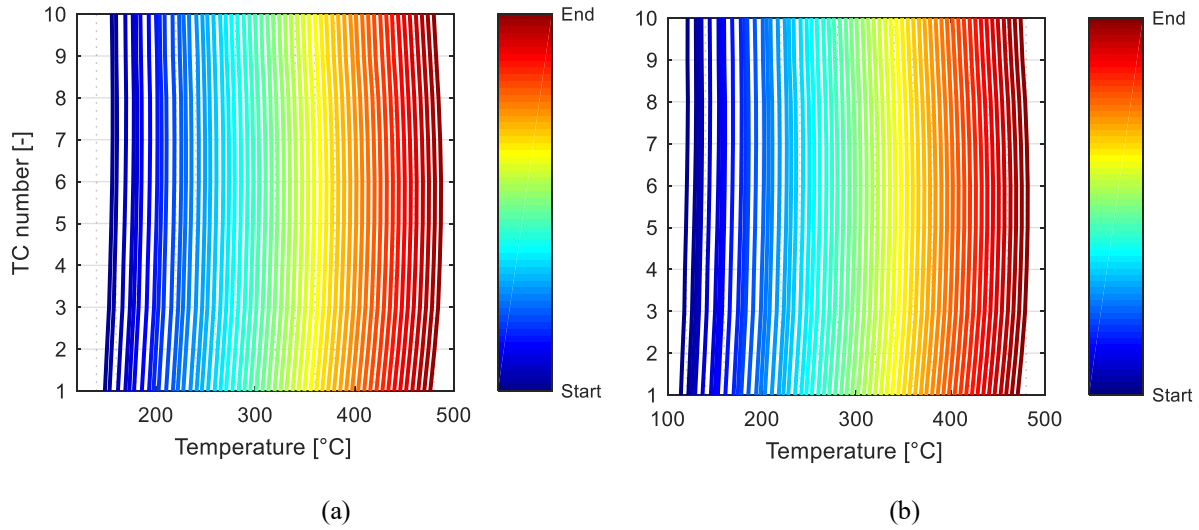

Figure 4.42*: Axial temperature profiles at peak conditions (step size: 3 min)* (a) *for the first TPO run and* (b) *for the second TPO run.*

The four reactive cycles performed on the diluted sample have not caused any visible agglomeration in the bed, since it was extracted from the reactor in powdery form, as it is shown in Figure 4.43, but probably the particles structure has changed at a smaller scale.

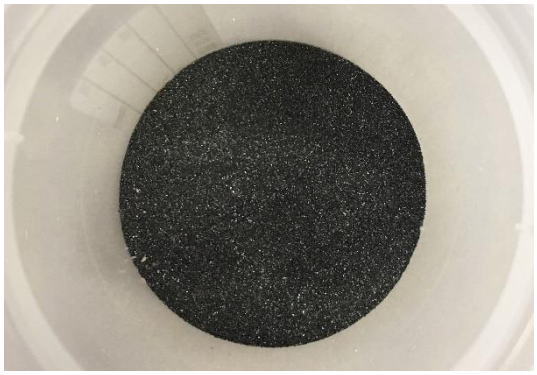

***Figure 4.43**: Appearance of the diluted bed after the two TPR-TPO series.*

It is then concluded that a high ratio bed dilution prevents agglomeration of the bed, at least on the macroscale, and helps to level out temperature gradient inside the bed.

4.6.2 Pure cupric oxide bed

Since a high bed dilution prevented to identify directly from the thermal profiles a variation of the sample temperature as the peak developed, a sample consisting of pure cupric oxide has been analysed with the setup described in §2.4. A higher mass of sample has been used in this test to cover six of the ten available measuring points of the thermocouple (from T7 to T2), and the resulting cupric oxide bed had the features reported in Table 4.29. The height of the quartz wool bed has been regulated in order to have T8, the controlling point, lying in the gas phase and close to the sample upper surface.

***Table 4.29**: Cupric oxide bed features.*

Parameter	Symbol	Unit of measure	Values
Main reagent species	-	-	CuO
Sample purity	-	[%]	99.995
Sample mass	m_s	[mg]	4750
Sample molecular weight	MW_s	[g/mol]	79.54
Sample molar amount	n_s	[mol]	$5.97 \cdot 10^{-2}$
Sample particle size range	d_p	[μm]	<300
Bed height	H_{bed}	[mm]	29
Bed volume	V_{bed}	[cm^3]	3.27

The sample underwent a thermal cycle under inert flow, a thermal cycle under oxidant mixture and two TPR-TPO cycles whose parameters are reported in Table 4.30.
The volumetric percentage of reagent for the TPRs run has been chosen so to develop a peak in reduction which could grant a peak shape between the two of Fig. 4.30, so avoiding both the

consumption of almost all the reagent fed and the simultaneous reduction of multiple layers of the bed. Since the sample had reduced in t=98 min in the first TPR of that test, and in t=55 min in the second, the desired time for a complete reduction of all the sample would reasonably lie around the mean of the two, so at $t_{peak,des}$=76.5 min. Seen the stoichiometry of the reduction reaction, shown in Equation (3.1), and assuming a constant reduction rate, the molar flowrate of hydrogen to be fed is calculated as in Equation (4.4)

$$\frac{n_s}{t_{peak,des}} = \frac{5.97 \cdot 10^{-2}\ mol}{76.5\ min} = 7.80 \cdot 10^{-4}\ mol/\min H_2 \tag{4.4}$$

which at standard temperature and pressure is equal to a volumetric flowrate of

$$\dot{V}_{H2} = \frac{\dot{n}RT}{P} = 18.76\ Ncm^3/\min H_2$$

being R the ideal gas constant, T the ambient temperature and P the ambient pressure. The total volumetric flowrate of the mixture is kept equal to the one used in §4.4.1, and so the resulting hydrogen volumetric percentage in the mixture is

$$y_{H2} = \frac{18.76\ Ncm^3/min}{250\ Ncm^3/min} = 7.5\ \%$$

The same volumetric percentage is used also in the two TPOs.

***Table 4.30**: Experimental parameters used in the cycles.*

	Cycle [-]	**Inert [-]**	**Reagent [-]**	$\dot{V}_{tot}$ **[Ncm³/min]**	y_R **[%]**	$\dot{n}_R^{in}$ **[mol/min]**	**β [°C/min]**	T_{fin} **[°C]**	t_s **[min]**
Inert thermal cycle	1	Ar	-	250	-	-	5	200	30
Oxidant thermal cycle	2	Ar	O_2	250	10	$1.04 \cdot 10^{-3}$	5	250	60
TPR	3	Ar	H_2	250	7.5	$7.80 \cdot 10^{-4}$	2	500	0
TPO	4	Ar	O_2	250	7.5	$7.80 \cdot 10^{-4}$	2	500	0
TPR	5	Ar	H_2	250	7.5	$7.80 \cdot 10^{-4}$	2	500	0
TPO	6	Ar	O_2	250	7.5	$7.80 \cdot 10^{-4}$	2	500	0

4.6.2.1 Redox cycles results

The two TPR profiles and their relative numerical results are reported in Figure 4.44 and Table 4.31.

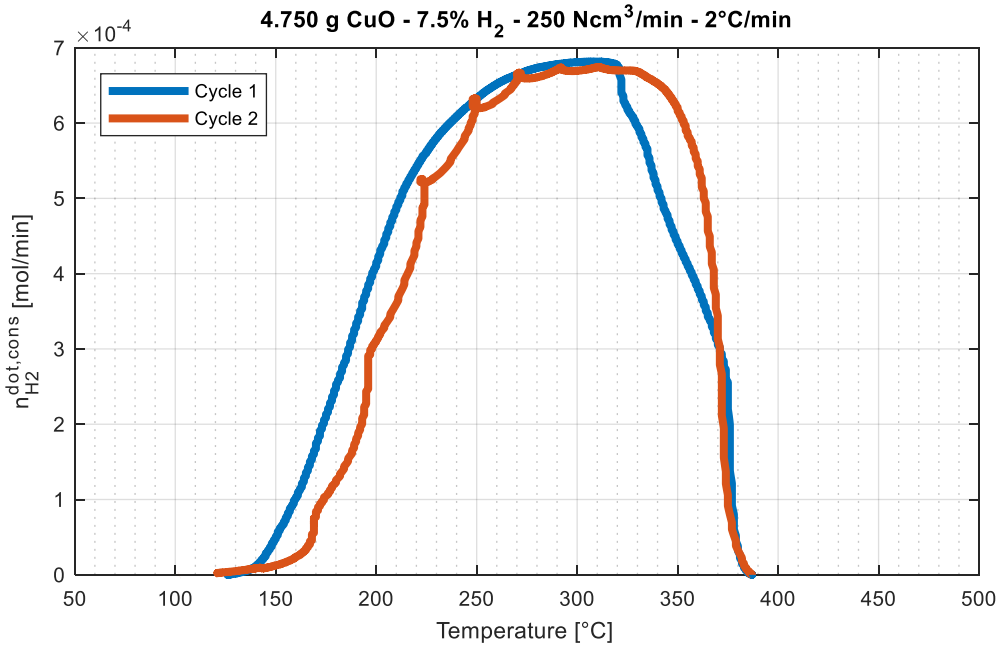

***Figure 4.44**: Hydrogen consumption profiles of the two TPR run with a pure CuO sample.*

***Table 4.31**: Relevant data concerning the two TPR run.*

TPR number [-]	K [s]	T_{act} [°C]	$T_{peak,1}$ [°C]	Secondary peak(s)	T_s [°C]	Peak range [°C]	$n_{O,CuO}^{cons}$ [mol]	$\%_{O,CuO}^{cons}$ [%]
1	4595	125	304	-	-	261	$5.58 \cdot 10^{-2}$	93.5
2	4595	105	304	-	-	281	$5.50 \cdot 10^{-2}$	92.1

As the data reports, one broad peak is obtained in each TPR run even with the parameters used, which made the K parameter lie outside the suggested range. The two peak shapes are similar: in both cases the temperature at which the peak is detected is the same, and also the one at which the peak ends, but in the second case the reduction starts at lower temperatures and with a lower velocity, being it the combined effect of the structural defects creation and the decrease of the surface area already evidenced. The second hydrogen consumption profile seems also affected by the slightly oscillating temperature, which deformed its peak.

Both reductions have a high efficiency, and almost all the copper oxide has reduced. Moreover, the bed agglomerated during the first TPR, since during this cycle the monitored pressure at the top of the reactor fell, as shown in Figure 4.45.

This could have been detrimental in the following test because, as reported in §4.6.2.2, the bed has axially shrunk of 5 mm, thus moving away its upper surface from the controlling point and making the temperature control loop less representative of the solid temperature.

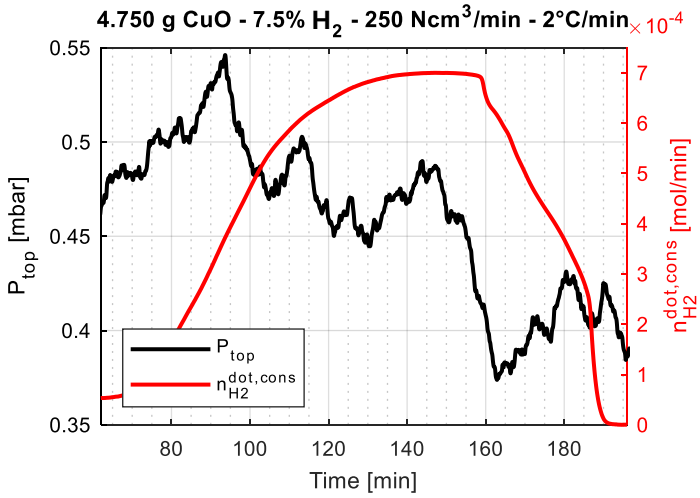

Figure 4.45: *Pressure at the reactor top and hydrogen consumption in the first TPR.*

The temperature profiles registered by the multipoint thermocouple, which are plotted in Figure 4.46.a, shows a perceivable local temperature increase in the bed as the reduction progresses: the maximum of each profile moves from T7 to T2 as the peaks develops, suggesting that the reaction advances from the top to the bottom of the bed, together with the gas flow.

Since the temperature reached by the sample is far from the melting point of its components (see Table 4.19) throughout all the thermal cycle, agglomeration is not caused by the exothermicity of the reaction.

Similar phenomena happen in the second TPR run: in this case the temperature rise caused by the reduction is slightly increased with respect to the previous one, as Figure 4.46.b shows. This behaviour could be linked to the sample agglomeration and to its distancing from the control thermocouple, which could not make the furnace compensate fast enough for temperature increase given by the reaction.

As the axial temperature gradient is not pronounced, however, it is concluded that the double peaks are not likely caused by inhomogenous hydrogen consumption in the sample.

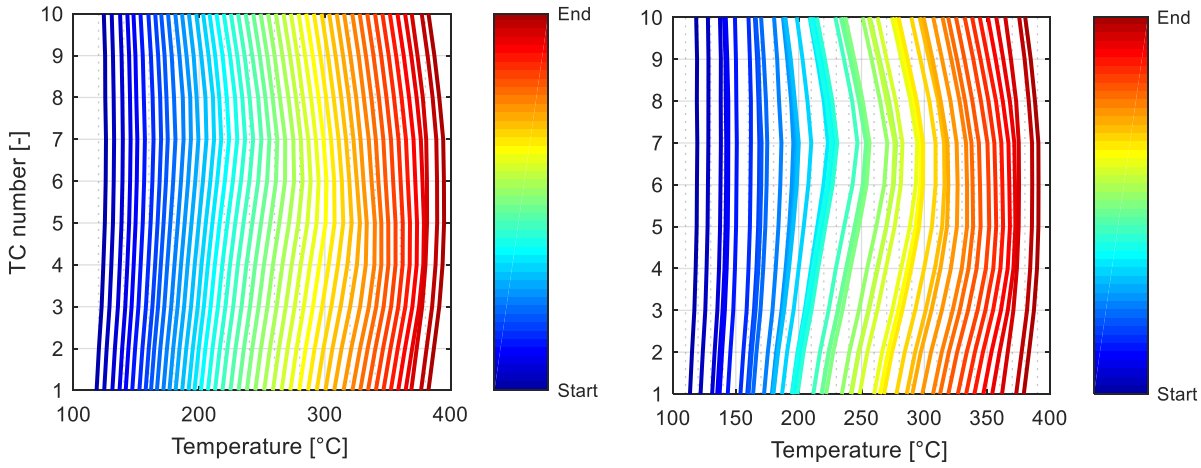

***Figure 4.46**: (a) Axial temperature profiles at peak conditions (step size: 3 min) (a) for the first TPR run and (b) for the second TPR run.*

The two TPO overall numeric results are presented in Table 4.32, while the single thermal cycles are represented Figure 4.47.b and Figure 4.48.b: a figure representing the oxygen consumption in temperature is not meaningful, since in this test the temperatures visibly oscillated. Given this fact, the temperature reported in the tables are the control thermocouple ones at their peaks.

***Table 4.32:** Relevant data concerning the two TPO run.*

TPO number [-]	T_{act} [°C]	$T_{peak,1}$ [°C]	$T_{peak,2}$ [°C]	$n_{O,CuO}^{reg}$ [mol]	$\%_{O,CuO}^{reg}$ [%]
1	169	293	461	$5.82 \cdot 10^{-2}$	97.5
2	172	322	494	$5.12 \cdot 10^{-2}$	85.7

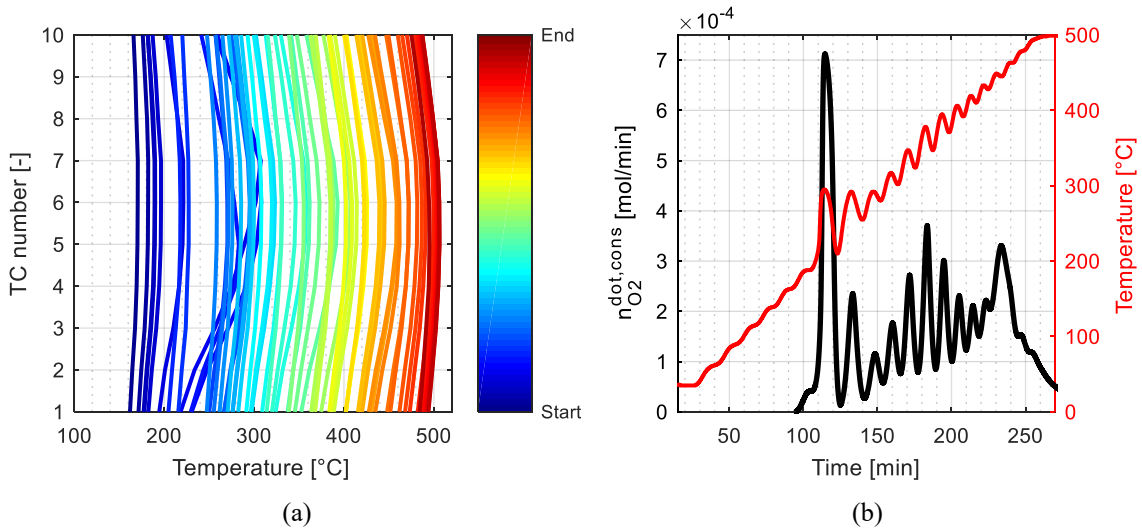

***Figure 4.47**: (a) Axial temperature profile (step size: 3 min) and (b) oxygen consumption and controlling thermocouple values of the first TPO run.*

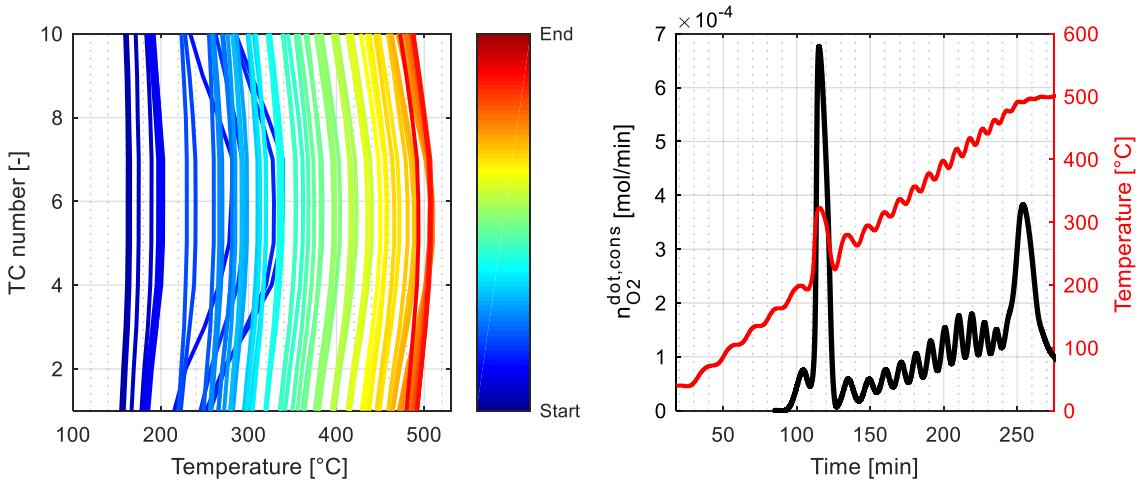

(a) (b)

Figure 4.48: (a) *Axial temperature profile (step size: 3 min) and* (b) *oxygen consumption and controlling thermocouple values of the second TPO run.*

As the data show, the bed oxidised almost completely in both the TPOs. On the other hand, as the first peak was approached (i.e. from t=115 min in both the TPOs), in both cases the energy release of the reaction was so high that the temperature in the bed raised of almost 100°C. As a consequence, the kinetic constant increase made the oxygen consumption accelerate dramatically.

From that moment on, an oscillatory behaviour established both in the temperature and in oxygen consumption because the furnace control tried to compensate for the exothermicity of reaction, though not being fast enough. As said above, this could have happened because the sample upper surface moved away the control point T8 due to the shrinkage, combined with an inadequate PID controller tuning.

Multiple peaks in temperature and in the oxygen consumption are then obtained, which are almost coincident in time. This is a clue that the two variables are correlated, but it is not straightforward to infer if this behaviour is given by the oscillation of the kinetic constant or by the superposition of an additional temperature gradient.

In both cases, especially as the first peak develops, the heat wave travels fast to the bottom of the sample, since temperature in the sample bottom reaches fast the upper temperature values, as seen in Figure 4.47.a and Figure 4.48.a. This behaviour could have been caused by the high thermal conductivity of the sample, which consisted initially of almost pure copper, coupled to the higher molar enthalpy of the oxidation.

In any case, as the temperature of the sample throughout both the TPOs never reached the melting temperature of its component (see Table 4.19), the agglomeration process could not be linked to the oxidation exothermicity either, and its cause should be investigated in other chemical phenomena.

4.6.2.2 Oxidised sample appearance

As a result of the thermal cycles of §4.6.2, a compact cylinder of copper oxide was produced, meaning that the agglomeration happened as the first TPR was carried out, as the pressure data of that test told. Its appearance is shown in Figure 4.49.a and Figure 4.49.b.

(a) (b)

Figure 4.49*:* (a) *Axial view of the sample and* (b) *the sample seen in perspective.*

The axial shrinkage of the sample was of 5 mm, and its weight was 220 mg less than the initial value (i.e. 4.75 g). Probably some material could have sticked to the internal surface of the tubular reactor. The spent oxide composition and structure is unknown, since no further analyses have been carried out, but Figure 4.49.b evidences some orange compounds in the hole made by the thermocouple. As copper and cuprous oxide are both orangish, it could be guessed that in the inner part the sample did not oxidize completely, as the last TPO degree of reduction suggested. Moreover, also the camera flash evidences some orangish reflection on its external surface, probably meaning that the complete oxidation was not completely favoured even in the outer layers.

Conclusions

The main objective of this thesis work was to apply temperature programmed reactions to obtain information about the redox reactivity of CuO/Cu system. This objective has been achieved by varying the experimental conditions and analysing the reducing/oxidizing profile shapes. Reagent concentration and heating rate were found to have the greatest effect on the peak shape, together with the identification of diffusional barriers and thermal inertia of the material. The bed dilution with silicon carbide proved to be effective both in TPR and in TPO analyses, promoting the sample reduction and oxidation at higher reagent concentrations. The increased CuO/Cu activity has been related to the silicon carbide capability of levelling out temperature gradients in the bed and favouring the inward oxygen diffusion process by delaying the sample agglomeration.

The CuO/Cu system long-term reactivity during sequential redox cycles (11) has been studied as well. A progressive loss in catalytic activity was identified through the peak shape analysis coupled with the quantifications of the sample oxygen consumed in reduction and regained in oxidation. During each reduction, a single-peak profile has been obtained, related to a single-step reduction mechanism ($CuO \rightarrow Cu$). A double-peak profile has been obtained only in three oxidations, the second peak progressively shifting to higher temperatures. These two peaks have been related to a two-step reduction of the oxide ($Cu \rightarrow Cu_2O \rightarrow CuO$). The disappearance of the second peak has been related to a structural rearrangement of the bed, both at a macroscopical and microscopical level, hindering the complete oxidation to CuO. After eleven cycles, the sample has visibly agglomerated in a compact lump and the SEM images showed that a crust developed over the original particles. The EDS results proved that, under the sample surface, copper and oxygen atoms were present in a ratio of 1.91:1, suggesting cuprous oxide (Cu_2O) to be the predominant oxide in that phase.

The analysis of higher-mass samples produced multiple peaks in the first TPR profile. Monitoring the pressure drop through the bed during reductions, oxidations and thermal cycles, clearly showed that the process responsible for the agglomeration is the reduction and it was not caused by the oxidative pre-treatment or thermal cycles carried out under inert flow.

Also in these cases, the bed had visibly compacted and the SEM images show that a structural change of the sample happens even after one redox cycle: a layer covers the reacting particles and nanofibres are created all over the flat surface. It is argued that this layer is created during the reduction step as soon as the pressure drop through the bed falls, hindering the inward reagent diffusion and delaying the peak. The quantifications show that neither the reduction

steps nor the oxidative steps were complete, suggesting that Cu_2O could be present in the oxidized sample pulled out from the reactor. The cupric oxide tendency to agglomerate combined with the loss in redox efficiency show that, if a higher long-term redox efficiency is desired, the oxide should be deposited over a support.

A silicon carbide bed dilution proved to be effective in obtaining a single peak in reduction, and two well-defined peaks in oxidation. This positive effect has been related to its capability of levelling out temperature gradients thanks to its high thermal conductivity, and hindering the contact among the reacting particles, as the agglomeration is delayed at the end of the first oxidation.

The axial temperature profile of a higher-mass sample has been monitored using a multipoint thermocouple: a single peak has been obtained in reduction and low temperature gradients axially developed, suggesting that double peaks in TPR profiles are not generated by an uneven temperature distribution in the sample. Rather than that, the multiple peaks observed in the other tests were most probably caused by physical effects, such as the bed agglomeration or its collapse. On the other hand, the different behaviour during TPO has been attributed to the higher exothermicity of the reaction, combined with the slow temperature control loop of the furnace. This last result underlines the primary importance of the PID tuning and of the correct placing of the control thermocouple, which should not be affected by disturbances deriving from the heat of reaction.

Nomenclature

c_p	=	Specific heat capacity
D_{eff}	=	Effective diffusion coefficient
D_g	=	Diffusion coefficient
d_p	=	Particle diameter
ΔH_R^0	=	Standard molar enthalpy of reaction
ΔP	=	Pressure drop
H_{bed}	=	Bed height
h_m	=	External mass transfer coefficient
m_s	=	Sample mass
$\dot{n}^{in}$	=	Molar flowrate fed
n_s	=	Sample molar amount
$n_{O,CuO}^{cons}$	=	Total sample oxygen consumed
$n_{O.CuO}^{reg}$	=	Total oxygen regained by the sample
T_{act}	=	Activation temperature
T_{fin}	=	Final temperature
T_m	=	Melting temperature
T_{peak}	=	Temperature of the peak
$T_{peak,1}$	=	Temperature of the first peak
$T_{peak,2}$	=	Temperature of the second peak
T_s	=	Temperature of the shoulder
t_s	=	Soak time
V_{bed}	=	Bed volume
v_{rel}	=	Relative velocity
$\dot{V}_{tot}$	=	Total volumetric flowrate
y	=	Volumetric percentage
$\%_{O,CuO}^{cons}$	=	Degree of reduction
$\%_{O.CuO}^{reg}$	=	Degree of oxidation

Greek letters:

β	=	Heating rate
ε	=	Porosity

λ	=	Thermal conductivity
μ	=	Dynamic viscosity
ρ	=	Density
τ	=	Tortuosity

Acronyms:

EDS	=	Energy Dispersive X-ray Spectrometry
SEM	=	Scanning electron microscope
TCD	=	Thermal conductivity detector
TPO	=	Temperature programmed oxidation
TPR	=	Temperature programmed reduction

References

[1] Fadoni, M. and L. Lucarelli, Temperature programmed desorption, reduction, oxidation and flow chemisorption for the characterization of heterogeneous catalyst. Theoretical aspects, instrumentation and application.

[2] Eser, S., Venkataraman, R., & Altin, O. (2006). Utility of Temperature-Programmed Oxidation for Characterization of Carbonaceous Deposits from Heated Jet Fuel. *Industrial & Engineering Chemistry Research*, **45**(26), 8956–8962.

[3] Hurst, N. W., S. J. Gentry, A. Jones, B. D. McNicol, Temperature programmed reduction. *Catalyst review: Science and Engineering,* **24**(2), 233-309.

[4] Gentry, S. J., Hurst, N. W., & Jones, A. (1979). Temperature programmed reduction of copper ions in zeolites. *Journal of the Chemical Society, Faraday Transactions 1: Physical Chemistry in Condensed Phases*, **75**(0), 1688.

[5] Monti, D. A., A. Baiker, (1983). Temperature-programmed reduction. Parametric sensitivity and estimation of kinetic parameters. *Journal of Catalysis*, **83**(2), 323–335.

[6] Gunn, D. J. (1978). Transfer of heat or mass to particles in fixed and fluidised beds. *International Journal of Heat and Mass Transfer*, **21**(4), 467–476.

[7] Bird, R. B., W. E. Stewart, E. N. Lightfoot, Transport phenomena, Wiley, 2nd edition, 538.

[8] Ibok, E. E., D. F. Ollis, (1980). Temperature-programmed desorption from porous catalysts: Shape index analysis. *Journal of Catalysis*, **66**(2), 391–400.

[9] Malet, P., A. Caballero, (1988). The selection of experimental conditions in temperature-programmed reduction experiments. *Journal of the Chemical Society, Faraday Transactions 1: Physical Chemistry in Condensed Phases*, **84**(7), 2369.

[10] Fierro, G., M. Lo Jacono, M. Inversi, P. Porta, R. Lavecchia, F. Cioci (1994). A Study of Anomalous Temperature-Programmed Reduction Profiles of Cu2O, CuO, and CuO-ZnO Catalysts. *Journal of Catalysis*, **148**(2), 709–721.

[11] Lee, J.-Y. and Lee, S. M. (1986). Hydrogen trapping phenomena in metals with B.C.C. and F.C.C. crystals structures by the desorption thermal analysis technique. *Surface and Coatings Technology,* ***28****(3-4), 301–314.*

[12] Rodriguez, J. A., J. Y. Kim, J. C. Hanson, M. Pérez, A. I. Frenkel (2002). Reduction of CuO in H_2: *In Situ* Time-Resolved XRD Studies. *Catalysis Letters,* **85,** 247–254.

[13] Günter, M. M., T. Ressler, R. E. Jentoft, B. Bems (2001). Redox Behavior of Copper Oxide/Zinc Oxide Catalysts in the Steam Reforming of Methanol Studied by in Situ X-Ray Diffraction and Absorption Spectroscopy. *Journal of Catalysis*, **203**(1), 133–149.

[14] Kim, J. Y., J. A. Rodriguez, J. C. Hanson, A. I. Frenkel, P. L. Lee (2003). Reduction of CuO and Cu2O with H2: H Embedding and Kinetic Effects in the Formation of Suboxides. *ChemInform,* **34***(50),* 10684–10692.

[15] García-Labiano, F., de Diego, L. F., Adánez, J., Abad, A., & Gayán, P. (2005). Temperature variations in the oxygen carrier particles during their reduction and oxidation in a chemical-looping combustion system. *Chemical Engineering Science,* ***60****(3), 851–862.*

[16] Bronkhorst® HIGH-TECH, *Instruction manual*, "General instructions digital Mass Flow/Pressure instruments laboratory style/IN-FLOW".

[17] Alphasense Application Notes, *AAN009*, "How oxygen sensors work".

[18] Zheng, C., Cao, J., Zhang, Y., & Zhao, H. (2020). Insight into oxidation mechanism of Cu-based oxygen carrier (Cu→Cu2O→CuO) in chemical looping combustion. *Energy & Fuels*, **34(7)**, 8718–8725.

[19] Ergun, S. (1952). Fluid flow through packed columns. *Chemical engineering progress,* **48**(2), 89-94.

[20] Green, D. W., Perry, R. H., Perry's Chemical Engineer's Handbook, Mc-Graw Hill, 7th edition.

[21] Biccari, F. (2009). Defects and doping in Cu_2O. *Ph.D. Thesis,* Università degli Studi di Roma "La Sapienza".

Ringraziamenti

Stento a crederci, ma alla fine anche per me è arrivato il momento di chiudere il mio percorso di studi. Sono consapevole di aver raggiunto questa ambita meta non solo grazie alle mie forze, ma anche grazie al supporto e all'affetto delle persone che mi sono state vicine in questi anni, e che vorrei qui di seguito ringraziare.

Prima di tutto, un ringraziamento speciale va a mio papà Aldo per essermi stato vicino in tutta la mia vita, e in particolare in questo ultimo periodo abbastanza faticoso. Nonostante ci siano stati molti momenti burrascosi in passato, posso dire con certezza di volergli tanto bene, e di stimarlo soprattutto per la sua praticità (qualità di cui sono sprovvista) che in molte situazioni mi ha aiutata a superare serenamente gli ostacoli. Vorrei ringraziare anche la mia mamma Raffaela che, pur non potendo essermi vicina fisicamente, rimane sempre nei miei pensieri e nei miei ricordi: a lei devo molto, soprattutto la tenacia con cui mi ha insegnato ad affrontare la vita, l'ottimismo con cui bisogna guardarla e la cura per i dettagli. Farò di tutto per renderti onore negli anni che verranno, mamma.

Vorrei poi ringraziare il prof. Paolo Canu per avermi accolto nel suo laboratorio, e per aver creduto in me anche quando io non ci credevo del tutto. Un grazie colossale va poi alla mia correlatrice Benedetta, per essersi fatta in quattro nel momento del bisogno, per avermi insegnato a ragionare, a cercare sempre una spiegazione per quanto si osserva, e soprattutto, a non agire "per sport" (cit.). Se questo lavoro di tesi ha assunto queste proporzioni è gran parte anche merito suo, e anche per questo le sono grata.

Colgo poi l'occasione per ringraziare anche tutti i compagni del CreLab, che hanno reso questo ultimo anno vivace ed entusiasmante: rapportarmi con voi mi ha permesso di imparare un sacco di cose, sia a livello pratico sia a livello umano, e ne sono felice. In particolare, vorrei ringraziare Mattia per i momenti di disagio condivisi sin dal primo giorno e per avermi aiutata a fare gli ultimi test in cappa HP, Micol e Arianna per avermi collegato il sensore di O_2 a Hiden mentre lavoravo da remoto, Luca per avermi fatto imparare *The sound of silence*, e Nicola per avermi corretto il capitolo 4 della tesi senza che gli fosse dovuto.

Vorrei ringraziare anche tutti i miei parenti per essermi stati vicini in questi ultimi anni, in particolare zia Marta e zia Franca, che con la loro presenza e il loro affetto hanno saputo riempire un vuoto incolmabile, e Stefano per essere stato un cugino speciale fin dall'infanzia.

Un grazie speciale va anche a tutti i miei amici con cui ho condiviso gli ultimi anni di università, ossia Enrico, Sara, Dodo, Arianna, Giovanni, Matteo, Alessandro, Stefano, Marco, Raffaello e Riccardo: passare le giornate in quel di Padova assieme a voi mi ha davvero resa felice. Inoltre,

vorrei ringraziare i miei amici Kelly, Alessandra, Elena, Silvia, Alessia e Francesco: anche se ho passato solo un anno e mezzo di vita universitaria in vostra compagnia vi ricordo come delle bellissime persone.
Un grazie va anche ai miei amici del JdP, ossia Giulia, Bea, Erica, Davide, Alberto e Daniele: anche se ci vediamo meno di un tempo, sono contenta che riusciamo a trovarci se non altro per festeggiare i compleanni e gli avvenimenti importanti della nostra vita, perché anche voi siete delle persone straordinarie.
Vorrei poi ringraziare Luca, amico d'infanzia e compaesano, per non essere mai sparito del tutto, e per avermi saputo strappare delle risate anche nei momenti più difficili. Per lo stesso motivo ringrazio anche Ilaria che, pur rimanendo discreta, ha saputo darmi conforto nel momento del bisogno e non mi ha mai lasciata sola.
Vorrei poi ringraziare Frenk, Angela, Matteo, Alberto, Michele, Anna, Cortif e Francesca per tutti i weekend passati in compagnia: penso che la vostra allegria e il modo in cui affrontate la vita siano davvero unici, e sono contenta di avervi conosciuti e di poter condividere con voi parte della mia vita.
Inoltre, non manca gratitudine nei confronti di Mario, Paola e Giulio, che da ormai un anno e mezzo sono quasi diventati la mia seconda famiglia: siete davvero speciali.
Infine ringrazio Ricky per essere stato sempre al mio fianco in questo ultimo periodo della mia vita: grazie per avermi fatto ridere, sognare, pedalare in sella alla Trek, e tante altre cose che mi rendono felice di essere qui e ora. Grazie per avermi sorretto nei momenti di sconforto, e grazie anche per non esserti mai trattenuto dal rimproverarmi, se notavi che qualcosa in me andava corretto. Sei fantastico.